PhD 17976.

The Upheaval Buckling of Buried Pipelines

UNIVERSITY LIBRARY CAMBRIDGE

Dissertation submitted to the University of Cambridge

for the Degree of Doctor of Philosophy

Timothy C. Maltby

St John's College

Cambridge

November 1992

Preface

This dissertation is the result of my own work and contains nothing which is the outcome of work done in collaboration.

Total Number of pages..... 133 .....

Acknowledgements

I would like to thank my supervisor, Professor Chris Calladine for his invaluable advice and support during the three years of this project. He has helped me considerably with all aspects of my work and for that I am very grateful. My thanks also to Professor Andrew Palmer and Professor Roger Hobbs, who have both given useful advice and guidance on various aspects of the project.

Roger Denston has provided a considerable amount of practical assistance and his help has been invaluable. Thanks also to the other members of staff who have contributed in many ways: Eric Silk, Chris Mason, Martin Touhey, Michael Price, Brian Butler, Clive Hannant, Vic Piper, Richard Christmas and others.

Thanks also to my friends and family, both here in England and at home in New Zealand. They have been wonderfully supportive over this time. Thanks to Sarah, Ian, John and Sue for their considerable help with proof reading.

Lastly, special thanks to the Commonwealth Scholarship Commission for giving me the opportunity to study here in England.

Abstract

Upheaval buckling is a serious problem which can be encountered during the operation of buried, submarine, oil and gas pipelines. These pipelines are usually operated at high temperatures and pressures (well above the conditions under which the pipe was laid), and the resulting axial expansion can cause significant axial compressive loads in the pipe wall. Under certain circumstances buckling can occur, with potentially disastrous consequences.

An important requirement for pipeline design is therefore to ensure that upheaval buckling does not occur. Most previous models of pipeline buckling have been based on the rigid base model; which is an old railway-track model that has been modified to suit the pipeline conditions. According to this model, a so-called minimum, buckling load can be calculated, and provided that the axial load is kept below this value, then buckling should not occur. In practice however, this model is unsatisfactory because buckling does occur at axial loads well below the so-called minimum value. The model is useful for analysing the post-buckling profile of the pipeline, but a better theory is required to explain the buckling process.

A number of modified buckling models have been proposed in the literature. However, despite the volume of literature available on this subject, there appears to be very little experimental data published to verify the numerous theoretical models. The purpose of this project has been to perform a number of experiments on a small-scale model of a buried pipe, in order to determine various aspects of the upheaval buckling behaviour. These aspects included: the force-displacement interaction of the pipeline and the soil, and the behaviour of the pipeline due to various combinations of horizontal and axial loading.

A simplified buckling model has been developed, and the results have been discussed in relation to this model. The model concentrates on the conditions under which buckling is initiated, and takes into account the force-displacement interaction between the pipe and the soil. The effect of cyclic loading was also investigated. Under repeated loading, the pipeline can displace by an incremental creep mechanism. A simple design model is suggested for the creep phenomenon.

Table of Contents

Preface ii
Acknowledgements iii
Abstract iv
Table of Contents v
List of Tables vi
List of Figures vii
Notation ix
Key Words x
1. Introduction 1-1
1.1. Background 1-1
1.2. A Buckling Case History 1-2
1.3. Design Methods 1-3
1.4. Description of Thesis 1-4
1.5. Figures 1-6
2. Literature Survey 2-1
2.1. Introduction 2-1
2.2. The Rigid-Base Model 2-1
2.2.1. Kerr's Railway Track Model 2-1
2.2.2. Hobbs' Pipeline Model 2-6
2.2.3. Dimensionless Groups for the Rigid-Base Model 2-8
2.2.4. Further Publications on the Rigid-Base Model 2-10
2.2.5. Summary of the Rigid-Base Model 2-13
2.3. The Elastic-Base Model 2-14
2.3.1. Kerr's Railway Track Model 2-14
2.3.2. Tvergaard & Needleman's Model 2-16
2.4. Palmer's Maximum Vertical Load Model 2-19
2.5. Figures 2-21
3. Theory 3-1
3.1. Introduction 3-1
3.2. The Simplified Buckling Model 3-2
3.3. The Effective Imperfection Amplitude 3-6
3.4. An Example 3-7
3.5. Determining the Initial Imperfection Amplitude 3-8
3.6. Figures 3-10
4. Experimental Apparatus 4-1
4.1. Introduction 4-1
4.2. Overview of the Apparatus 4-1
4.3. Details of the Apparatus 4-2
4.3.1. The Channel Section 4-2
4.3.2. The Test Pipe 4-3
4.3.3. The Pipe End-Mountings 4-4
4.3.4. The Pipe and Soil Levelling Tools 4-5
4.3.5. The Soil Material 4-6
4.3.6. The Position-Sensors and the Sensor-Trolley 4-7
4.3.7. The Position-Measuring System 4-9
4.4. Calibration of the Apparatus 4-10
4.5. Figures 4-11
5. Experimental Results 2-1
5.1. Introduction 5-1

5.2. The Soil Forces 5-1
5.2.1. The Horizontal and Vertical Soil-Response 5-1
5.2.2. The Soil Hysteresis 5-4
5.3. The Axial Load Tests 5-5
5.3.1. A Typical Test Result 5-5
5.3.2. The Overall Results 5-8
5.4. Horizontal Loads 5-9
5.4.1. Horizontal Load Only 5-10
5.4.2. Combined Axial and Horizontal Loads 5-12
5.4.3. Adding and Removing the Horizontal Load 5-13
5.5. Cyclic Axial Loading 5-15
5.5.1. Typical Results 5-16
5.5.2. The Overall Results 5-17
5.6. Figures 5-20
6. Summary and Conclusions 6-1
6.1. Literature Survey 6-1
6.2. Theory 6-1
6.3. Experimental Results 6-2
6.3.1. The Soil-Response 6-2
6.3.2. Axial loading 6-3
6.3.3. Combined Horizontal and Axial Loading 6-4
6.3.4. Cyclic Loading 6-4
6.4. Further Research 6-6
7. Bibliography 7-1
A.1 The Experimental Apparatus 8-1
A.1.1 Details of The Apparatus 8-1
A.1.2 Control System 8-2
A.1.3 The Position Measuring Algorithm 8-2
A.2 List of the Experimental Tests 8-3
A.2.1 The Soil Response Tests 8-3
A.2.2 The Axial Load Tests 8-4
A.2.3 The Horizontal Load Tests 8-5
A.2.4 The Combined Horizontal and Axial Load Tests 8-5
A.2.5 Add and Remove The Horizontal Load 8-5
A.2.6 The Cyclic Axial Load Tests 8-7
A.3 The Finite-Difference Model 8-8
A.3.1 Theory 8-8
A.3.2 The Finite-Difference Algorithm 8-9
A.3.3 Figures 8-10

List of Tables

Table 5.1. The experimental values of W_0 and Y_1 for vertical displacement 5-2
Table 5.2. The experimental values of W_0 and X_1 for horizontal displacement 5-3

List of Figures

Figure 1.1. A schematic diagram of upheaval buckling 1-6
Figure 2.1. A schematic diagram of the rigid-base model 2-21
Figure 2.2. The axial-load distribution in a buckled pipeline 2-21
Figure 2.3. The buckling load according to the rigid-base model 2-22
Figure 2.4. The effect of axial-friction on the rigid-base model 2-22
Figure 2.5. A dimensionless plot of the data from the rigid-base model 2-23
Figure 2.6. The three types of imperfections 2-23
Figure 2.7. The effect of imperfections according to Ju & Kyriakidies' model 2-24
Figure 2.8. Pedersen & Jensen's maximum displacement model 2-24
Figure 2.9. A schematic diagram of the elastic-base model 2-25
Figure 2.10. The buckling mode-shapes 2-25
Figure 2.11. The bilinear and exponential models of the soil-response 2-26
Figure 2.12. The effect of imperfections according to Tvergaard & Needleman's model 2-26
Figure 2.13. The effect of varying the wavelength 2-27
Figure 2.14. The buckling load according to Tvergaard & Needleman's model 2-28
Figure 2.15. The Palmer model of the maximum vertical load 2-28
Figure 3.1. A schematic diagram of the simplified buckling model 3-10
Figure 3.2. The buckling load according to the simplified buckling model 3-10
Figure 3.3. A comparison of the buckling loads from three different models 3-11
Figure 3.4. The variation of the peak load with the half-wavelength 3-11
Figure 3.5. The effect of wavelength on the arch and bending terms 3-12
Figure 3.6. A schematic diagram of an arbitrary sinusoidal imperfection 3-13
Figure 3.7. A method for determining the effective amplitude 3-13
Figure 3.8. A dimensionless plot of the effective amplitude versus the wavelength 3-14
Figure 3.9. A dimensionless Palmer plot of the effective amplitude data 3-14
Figure 3.10. The displacement data from the finite difference model 3-15
Figure 3.11. A Southwell plot of the data from the finite-difference model 3-15
Figure 4.1. An end elevation of the sensor-trolley 4-11
Figure 4.2. A view of the under side of the sensor-trolley 4-12
Figure 4.3. A photograph of the sensor-trolley 4-13
Figure 4.4. A schematic view of the main experimental apparatus 4-14
Figure 4.5. A side elevation of the North end-mounting block 4-15
Figure 4.6. The apparatus used to measure the soil forces 4-16
Figure 4.7. The reference data grid points 4-16
Figure 4.8. An end elevation of the pipe and soil levelling tools 4-17
Figure 4.9. The effect of re-levelling the soil on the vertical position 4-17
Figure 4.10. The reference data for sensor two 4-18
Figure 4.11. The reference ratio data, sensor two to sensor three 4-18
Figure 4.12. Calibration of the horizontal pipe position 4-19
Figure 4.13. Calibration of the vertical pipe position 4-19
Figure 5.1. The vertical force-displacement response of the test soil 5-20
Figure 5.2. The horizontal force-displacement response of the test soil 5-20
Figure 5.3. The interaction of the horizontal and vertical soil forces 5-21
Figure 5.4. The variation of W and K with the depth of soil cover Q 5-21
Figure 5.5. The hysteresis of the vertical soil-response 5-22
Figure 5.6. The hysteresis of the horizontal soil-response. 5-22
Figure 5.7. The vertical displacement for an increasing axial load 5-23
Figure 5.8. The horizontal displacement for an increasing axial load 5-23
Figure 5.9. A polar plot of the displacement for an increasing axial load 5-24
Figure 5.10. A plot of the load versus the displacement 5-24

Figure 5.11. A Southwell plot of the pipe displacement 5-25
Figure 5.12. The buckling load versus the estimated imperfection size, Q=6 mm..... 5-25
Figure 5.13. The buckling load versus the estimated imperfection size, Q=12 mm 5-26
Figure 5.14. A schematic diagram of the application of a horizontal load 5-26
Figure 5.15. The horizontal displacement for an increasing horizontal load..... 5-27
Figure 5.16. The horizontal displacement versus the load, log plot 5-27
Figure 5.17. The horizontal wavelength versus the load, log plot 5-28
Figure 5.18. The approximate value of W 5-28
Figure 5.19. The horizontal displacement, combined horizontal & axial load..... 5-29
Figure 5.20. The vertical displacement, combined horizontal & axial load 5-29
Figure 5.21. A Southwell plot, combined horizontal and axial load..... 5-30
Figure 5.22. The horizontal displacement, add & remove a horizontal load..... 5-30
Figure 5.23. A polar plot, add & remove a horizontal load..... 5-31
Figure 5.24. The effect of the position of the horizontal load 5-31
Figure 5.25. The effect of varying the size of the pre-load 5-32
Figure 5.26. The vertical displacement from cycling the axial load 5-32
Figure 5.27. The horizontal displacement from cycling the axial load..... 5-33
Figure 5.28. The vertical displacement from cycling the axial load 5-33
Figure 5.29. The horizontal displacement from cycling the axial load..... 5-34
Figure 5.30. The vertical displacement versus the number of cycles..... 5-34
Figure 5.31. The effect of peak load and cycle load..... 5-35
Figure 5.32. The vertical displacement during the cycle..... 5-35
Figure 8.2. A schematic diagram of the finite-difference model 8-10

Notation

Alphabetical

A	Cross Sectional Area m^2
c	Shear Strength of Soil N/m^2
D	Diameter m
E	Young's Modulus N/m^2
F	Axial Friction Force N/m
f	Friction Angle
g	Gravitational Constant N/Kg
H	Imperfection Height m
I	2nd Moment of Area m^4
K	Soil Elastic Constant N/m^2
L	Wavelength m
M	Bending Moment Nm
m	Moment due to vertical load Nm
N	Thermally Induced Axial Load N
OD	Outside Diameter m
P	Compressive Axial Load N, also refers to Polynomial
PC	Personal Computer
Q	Depth of Soil Cover Above Pipe m
R	Radius m
S	Largest Sensor Output V
SS	Ratio of Largest Sensor Output / Next Largest output
T	Temperature ^oC
t	Wall Thickness m
U	Horizontal Load N
V	Imperfection Amplitude m
W	Downwards Vertical Load N/m
w	Force exerted on 300 mm test bar by soil N
X	Horizontal Position mm co-ordinates
x	Horizontal Position grid co-ordinates
Y	Vertical Position mm co-ordinates
y	Vertical Position grid co-ordinates
Z	Axial Position 100 mm per unit
z	The ratio of imperfection amplitude to half wavelength

Greek

α	Coefficient of Thermal Expansion $^oC^{-1}$
Δ	Prefix denoting change in value
ρ	Density Kg/m^3
ξ	Characteristic Length of Deflection

Subscripts

b	The simplified Buckling Model
c	Cyclic Load
data	Experimental Data Value
e	Elastic Base Model
eff	Effective
f	Finite Difference Model
L	Minimum buckling Values from the Rigid base Model
l	Elastic Limit
max	Maximum Value
o	Original Value
p	Pre-load
ref	Reference Data Value
t	Tvergaard and Needleman Model
1, 2 ..	Number

Superscripts

*	Dimensionless Variable

Key Words

Axial load, Buckling, Elastic-base, Hobbs, Horizontal, Instability, Kerr, Lateral, Palmer plot, Proportional limit, Rigid-base, Soil-Response, Southwell plot, Temperature-Rise, Tvergaard & Needleman, Upheaval, Vertical.

1. Introduction

1.1. Background

The upheaval buckling of buried, submarine pipelines is a compressive instability phenomenon which is caused by operating oil and gas pipelines at high temperatures and pressures. The high operating temperatures are necessary in order to prevent condensation occurring in the pipeline, or the separation of various low-temperature constituents from the flow. The high operating pressures are necessary, in order to achieve high flow rates.

Pipelines are normally laid with zero axial tension, at the temperature of the surrounding environment. Under normal operating conditions, the difference between the operating temperature and pressure, and the as-laid conditions, would cause an unrestrained pipe to expand. The axial expansion is however restrained by the axial friction of the soil, thus inducing significant compressive axial loads in the pipe wall. Being a long thin member, the pipe is particularly vulnerable to compressive buckling; and this sometimes occurs, usually at the location of an initial out-of-straightness of the pipe centreline. Pipelines lying on the surface tend to buckle horizontally while those buried in a trench tend to buckle vertically, with the pipe emerging from the soil and forming an extended loop.

A schematic diagram of vertical or upheaval buckling is shown in figure 1.1. A section of pipeline, which is represented by a centreline, is shown in its initial position buried in the trench, and also in its buckled position with a section of the pipe lifted up out of the soil. Buckling has occurred at the location of an initial imperfection, or out-of-straightness of the centreline. In the context of this Thesis, the term imperfection refers to such an out-of-straightness. If an axial load is applied to the pipe, the imperfection grows in magnitude as the axial load increases until at some critical combination of load and displacement, buckling occurs.

Buckling is undesirable because of the potential for serious damage to occur to the pipeline; and considerable effort and expense is often exerted to prevent it occurring. If suitably designed and installed, the vertical restraint provided by the weight of the pipe and the soil is

often sufficient to prevent it. In some circumstances other measures such as rock dumping or residual lay tension are necessary. The important parameters in the design are the induced axial load, the flexural rigidity of the pipe, the vertical restraint provided by the soil and the size of the initial imperfections in the pipeline.

A further feature of the problem is the existence of an incremental ratcheting mechanism. This can occur when the temperature and pressure is repeatedly cycled, as when the pipeline is shut down for maintenance, or for other reasons. In such cases, pipelines are reported to have moved up through the soil over a period of time, and to have eventually buckled at a load considerably below the design buckling load. One such case history is described below.

1.2. A Buckling Case History

The case history of the first recognised occurrence of submarine buckling is described by Nielsen, Lyngberg & Pedersen (1990). The pipeline in question was 17 km in length and carried oil from a satellite platform to a central processing facility. The pipeline consisted of an inner steel pipe 0.22 m outer diameter, which was covered with a foam insulating layer and a concrete jacket 0.45 m outer diameter. A small auxiliary gas pipeline of 0.075 m outer diameter was attached to the main pipeline. The maximum operating temperature was approximately 82 °C, the ambient temperature being approximately 10 °C, and the pressure differential was approximately 1000 psi. The pipeline was buried so that the minimum depth of cover from the top of the pipeline was 1.15 m; the minimum depth of soil cover having been determined by the rigid-base, buckling model.

The pipeline was installed during the summer of 1985 and first brought into service in January 1986. In July 1986 the sea bed above the pipeline was surveyed using a side scanning sonar. A buckled section of the pipe was discovered protruding from the sea bed, approximately 0.3 km from the platform. The protruding section had a peak height of 1.1 m above the sea bed, and a length of 10 m. The overall wavelength of the buckle was approximately 24 m. No other buckles were evident during the survey. From the marine

growth on the exposed section of the pipe, the buckle was estimated to have occurred in January, the same month that the pipe was commissioned.

Following this event, it was decided to carry out a comprehensive sub-bottom profile survey along the entire length of the pipe, using a remotely operated vehicle (ROV). The survey was performed in September 1986, and a second buckle was discovered at a location approximately 2.2 km from the platform, i.e. approximately 1.9 km from the first buckle. The second buckle had not been evident at the time of the July survey and had thus occurred in the intervening 2-month period. The survey also found that there were 26 severe undulations along the pipeline, of amplitude 0.5-1.0 m. These undulations appeared to have grown during the 8-month period between commissioning the pipeline and the comprehensive survey.

The growth of the second buckle and the imperfections was thought to be due to the numerous shutdowns which had occurred. There had been 15 major shutdowns of between 1 and 17 hour duration during the 6-month period preceding the discovery of the first buckling failure, and another 2 major shutdowns before the second survey was performed. In addition, both buckling failures had occurred at locations where the pipe had been damaged by fishing trawl boards during the laying and trenching operation. The pipeline had been bent sideways by the trawl boards at 10 locations. The damaged sections of pipe were left temporarily un-trenched until the inspection and repair operations had been completed.

Thus it appeared that the pipeline had operated satisfactorily when first installed. However, at each shutdown and start-up with its subsequent cooling and re-heating, and consequent axial unloading and loading, a small non-reversible upwards displacement of the pipe had occurred. Eventually the pipe had buckled at a load well below the design buckling load. The presence of bends in the pipe because of trawler damage was also obviously an important factor in the incremental failure.

1.3. Design Methods

The design method for upheaval pipe buckling which had been current in the mid-1980's, was based on the "rigid-base" railway-track model. This model was first proposed by Martinet in 1936 and is described further in Chapter 2. According to this model, a "safe"

temperature rise can be calculated which is independent of the size of the initial imperfections, but which is highly dependent on the value of axial friction between the pipe and the soil.

This method had been used in the case history described above, but upheaval buckling had occurred at a temperature well below the so-called "safe" temperature which was calculated in this way. Clearly, the existing design procedures, based on the accepted theory were no longer satisfactory.

Following the 1986 incident a number of new buckling models have been developed. Generally these have been based on the rigid-base model, but are increasingly complex numerical versions which allow for various non-linearities in the pipeline and soil behaviour. One such model, UPBUCK is the result of a joint industry study and is described in Chapter 2. For this model the vertical force-displacement characteristics of the soil are measured with a short length of pipe and the data are input into a computer programme in order to calculate a safe operating temperature.

There is however, a lack of empirical data on the behaviour of a complete section of pipeline, to support the new theoretical models; and it is not obvious which if any of the various theories is correct. Therefore the main purpose of this project has been to perform a series of experiments on a model test pipe, in order to obtain experimental data and to develop a deeper understanding of the buckling process. The content of the thesis is described below.

1.4. Description of Thesis

Several sets of experiments have been performed on a model test pipe buried in soil, in order to investigate various aspects of the pipe buckling behaviour and the mechanisms by which buckling occurs. The factors which were of interest include the following:

The pipe-soil interaction.

The pipe displacement preceding buckling.

The magnitude of the buckling loads.

The effect of imperfection size.

The effect of cycling the axial load.

An experimental apparatus was designed and built for this purpose and various experiments

were performed. The experimental results are described in this Thesis, and this is set out as follows:

The published literature is reviewed in Chapter 2. The review is not exhaustive, but is restricted to a small number of papers which deal with the main points of the theory. This includes some theory on the vertical instability of railway tracks, and on lateral or horizontal buckling. The bibliography contains a more complete list of the relevant papers.

Some simple theory, which has been developed in conjunction with the experimental data, is described in Chapter 3. This includes a simplified buckling model, a model of the effect of varying the wavelength of an imperfection, and a method for estimating the amplitude of the initial imperfections in the test pipe.

The experimental apparatus is described in Chapter 4. A notable feature of the apparatus is the remote-sensing, position-measuring system, which was developed in order to measure the position of the pipe under the soil without disturbing either the pipe or the soil.

The results are presented and discussed in Chapter 5. Several different types of experiments were performed in order to examine different features of the buckling process and these are described in detail.

A summary and conclusion is given in Chapter 6.

Appendix A.1 contains further details of the apparatus. The experiments performed are listed by type in Appendix A.2. The finite-difference, numerical model is described in Appendix A.3.

The figures referred to in the text are located at the end of each Chapter.

1.5. Figures

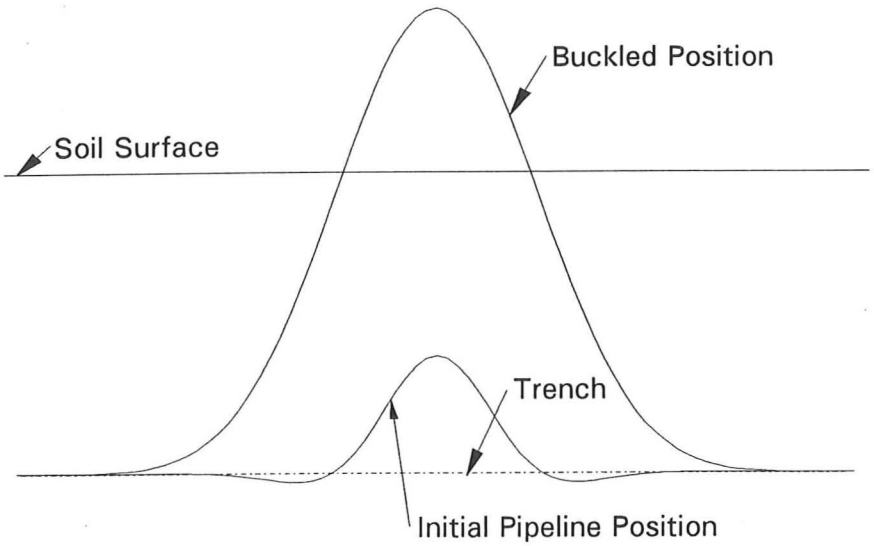


Figure 1.1. A schematic diagram of upheaval buckling, showing the initial position of the pipe in the trench, and the buckled position. Note that the horizontal and vertical scales are different, and that the pipe is represented by a centreline.

2. Literature Survey

2.1. Introduction

There is a large volume of material published on both the upheaval and lateral buckling of pipelines, and on the closely related problem of the buckling of railway tracks. In this Thesis, we are primarily interested in the phenomenon of upheaval buckling. Rather than review all of the available literature, a number of papers have been selected which encapsulate the key points and these papers are described in some detail. Broadly speaking, there are two types of buckling model described in the literature, the rigid-base model and the elastic-base model. These are described below

A wide variety of different notation is used in the literature. For consistency therefore, a standard notation has been used throughout this Thesis. Where possible, the different models described in this Chapter have all been analysed using the same data. The data has been taken from the test pipe and the soil, which were used in the experiments.

In the case of the Tvergaard and Needleman model, their original analysis has been re-presented here in a simplified form. The data from the test soil data has been used, but it has been approximated by an "exponential" soil-response curve, which is described further in Chapter 3, and the pipe deflection is assumed always to be sinusoidal.

This Chapter also includes two features which are not in the published literature, but which have been developed as part of this Thesis. A simplified axial-friction model is described in section 2.2.1; and a dimensionless version of the rigid-base model is described in section 2.2.3. They are included in this Chapter, rather than elsewhere, for convenience.

2.2. The Rigid-Base Model

2.2.1. Kerr's Railway Track Model

Kerr (1974) has reviewed the literature on the vertical instability of railway track. He describes the rigid-base model of a straight railway track; the track is modelled as a continuous heavy beam of flexural stiffness EI Nm^2, which is compressed by an axial load P N. The self-

weight of the beam W N/m is constant and acts vertically downwards. The beam is supported on an infinitely rigid base.

The track is assumed to be initially straight; however in order to proceed with the analysis, it is necessary to assume that a buckle has somehow already formed. Such a buckle, of total length L and height H, is shown in figure 2.1.a. The buckle is supported at each end by a localised or point reaction R of magnitude WL/2 N. The forces and moments acting on a typical beam element of length dx, are shown in figure 2.1.b. From small deflection beam theory, provided that the slope $|dy/dx|$ is small, the governing equation can be written as:

$$EI\frac{d^4y}{dx^4} + P\frac{d^2y}{dx^2} = -W \qquad (2.1)$$

The boundary conditions for a symmetrical buckle are that:

(i) at $x = 0$ $y' = 0$

(ii) at $x = \pm L/2$ $y = 0$, $y' = 0$, $y'' = 0$.

The last condition arises from the requirement for continuity of the bending moment at the points of support, the bending moment being zero in the sections of pipe lying on the base. Kerr gives the solution as:

$$y = \frac{WEI}{P^2}\left(-\frac{\cos(nx)}{\cos\left(\frac{nL}{2}\right)} - \frac{n^2x^2}{2} + \frac{n^2L^2}{8} + 1\right) \qquad (2.2)$$

where $n^2 = P/EI$ m^{-2}. This satisfies all boundary conditions except $y'' = 0$ at $x = L/2$. This requires that $\tan(nL/2) = nL/2$, which has a series of solutions: $nL = 8.9868$, 15.4504, 21.8082..... The lowest value of the buckling load P_r corresponds to the first solution, $nL = 8.9868$. The subscript $_r$ is used here to denote the terms from the rigid-base model. Re-arranging the first solution, P_r can be expressed in terms of the buckle length L_r as:

$$P_r = \frac{80.76EI}{L_r^2} \qquad (2.3)$$

Alternatively, by substituting $nL = 8.9868$ into equation (2.2) and rearranging, P_r can be expressed in terms of the height at the centre of the buckle H, as:

$$P_r = 3.962\sqrt{\frac{WEI}{H}} \qquad (2.4)$$

Combining equations (2.3) and (2.4) and eliminating P_r, the buckle length L_r can be expressed as:

$$L_r = 4.514\sqrt[4]{\frac{HEI}{W}} \qquad (2.5)$$

Note that the variables L_r, H and P_r are inter-dependent. If any one of the three variables is known the other two can be calculated from equations (2.3) to (2.5).

The above analysis is based on the assumption that a buckle has already formed. Before the buckle has formed, the thermally induced load N_0 N, in the straight track can be expressed as:

$$N_0 = EA\alpha\Delta T \qquad (2.6)$$

where EA N is the axial stiffness of the track, ΔT °C is the increase in temperature above the temperature at which the axial load is zero, and α $°C^{-1}$ is the coefficient of thermal expansion. If the track is then disturbed so that a buckle forms, the axial load in the buckled section of track will be reduced by an amount ΔN, because of the elastic extension of the track as it deflects. The total extension is equal to the difference between the arc length S of the buckled section and the buckle wavelength L, a term which is sometimes called the "geometric shortening". In general, provided $|dy/dx|$ is small, we find that:

$$S - L = \int_0^L \frac{1}{2}\left(\frac{dy}{dx}\right)^2 dx \qquad (2.7)$$

For the simplest case we assume, somewhat unrealistically, that no axial slippage occurs between the track and the base; and so the elongation is restricted to the buckled section of the track. In this case the reduction in load ΔN, which equals the difference between N_0 and P_r, is related to this small change in length by the elastic law:

$$\Delta N = (S - L)\frac{EA}{L} \qquad (2.8)$$

In order for no axial slippage to occur, the axial force N in the buckle zone must be distributed as shown in figure 2.2.a, i.e. $N = N_0$ throughout the section of track in contact with the base

and $N=P_r$ in the buckled section. Clearly, the buckled configuration is not possible unless $N_0 = \Delta N+P_r$. Thus, by substituting for ΔN and P_r. from equations (2.8) and (2.4), the value of N_0 can be calculated in terms of L by:

$$N_0 = \frac{80.76EI}{L^2} + 1.597x10^{-5}\frac{W^2EAL^6}{(EI)^2} \qquad (2.9)$$

The 2nd term on the RHS is the geometric shortening term, ΔN. Alternatively, N_0 can also be expressed in terms of L as:

$$N_0 = 3.962\sqrt{\frac{WEI}{H}} + 0.1347H^{3/2}\sqrt{\frac{W}{EI}}EA \qquad (2.10)$$

These equations give the condition for a buckle of height H and length L, to be able to form.

Generally there is insufficient axial friction to prevent axial slippage occurring, and the expression for N_0 must be modified to account for this. The axial-friction force F can be modelled in several ways. One such model is based on the assumption that the axial-friction force F N/m between the pipe and the soil is due to Coulomb friction, with coefficient λ, i.e. $F=W\lambda$ N/m. The axial force distribution corresponding to this assumption, is shown in figure 2.2.b. The axial force $N=P_r$ in the central arched section of track as before. The step in N at each end of the buckle is of magnitude $R\lambda=WL\lambda/2$, and is due to the vertical point reaction $R=WL/2$ at those points. The slope of the two triangular regions is $W\lambda$, and is due to the weight of the track. The slip length L_s is the length of pipe affected by axial slippage.

The expression for N_0 is somewhat more complicated than in the previous case. Martinet (1936) derived the following expression for N_0 in the case of a Coulomb friction force, F:

$$N_0 = \frac{80.76EI}{L^2} + L\sqrt{F\left(\frac{W^2L^5A}{62,566EI^2} - \frac{F}{4}\right)} \qquad (2.11)$$

provided that the second term on the RHS has a real value. This expression reduces to equation (2.9) when $WL\lambda/2=1.597 \times 10^{-5}\, W^2EAL^6 / (EI)^2$.

Note that if the two triangles are continued by the dotted lines shown, the lines meet at the point A. For small values of the friction coefficient λ, the slip length $L_s >> L$ and the axial load distribution can be approximated by the triangle geometry shown in figure 2.2.c. This is

made by omitting the "wings" from figure 2.2.b. These are shown by a dotted line in figure 2.2.c. For this approximate friction model, N_0 can be expressed as:

$$N_0 = \frac{80.76EI}{L^2} + 3.996x10^{-3}\frac{WL^{7/2}}{EI}\sqrt{FEA} \qquad (2.12)$$

This is a simpler form of equation (2.11), without the -F/4 component in the last term.

For each of the three models described above, the first term on the RHS of each equation is the buckling load P_r, and represents the axial force in the uplifted part of the track. The second term involves the particular friction (or axial slippage) law which is used. Whichever friction law is used, the shaded areas in figure 2.2.a, b & c, should be equal.

Having derived these various formulas, let us now investigate their physical meaning. The simplest case occurs when there is no axial slippage, as in equation (2.9). This is illustrated in figure 2.3. The values of both P_r and N_0 are plotted versus H; the values of W, EI and EA being taken from the model pipeline which is described in Chapter 4. The difference in ordinate between the two curves represents the geometrical shortening term ΔN. It can be seen from the graph that N_0 has a minimum value N_L, denoted by the subscript $_L$. The value of the minimum load $N_L \approx 118$ N and the corresponding height $H_L \approx 7$ mm.

Clearly, buckling cannot occur unless N_0 exceeds N_L, otherwise equation (2.9) has no real solution. If N_0 exceeds N_L there are two solutions, which correspond to two possible buckling configurations; an unstable configuration on the left branch of the curve and a stable configuration on the right branch. This is shown in the figure. A section of straight track with an initial load $N_0 = 180$ N is shown at point A. If the track is somehow deflected to point B, it will then be unstable and will immediately snap-through buckle to the stable point at C as shown by the dashed line.

The more general case where axial slippage occurs is illustrated in figure 2.4. The same variables are plotted using the approximate friction model described by equation (2.12). A series of curves have been plotted for values of the Coulomb friction coefficient λ varying between 0 & ∞, although in practice it is unlikely that $\lambda > 1$. In this case the data is plotted as the temperature-rise ΔT °C, versus the buckle length L m. The temperature-rise ΔT °C can be

calculated by dividing N_0 by $EA\alpha$, and is measured relative to the temperature at which the axial load is zero.

It can be seen that the minimum buckling temperature-rise ΔT_L and the corresponding buckling wavelength L_L, are highly dependent on the value of the friction coefficient λ. As λ decreases the value of ΔT_L decreases and the value of L_L increases. The values of $\Delta T_L = 7\ ^oC$ and $L_L = 2.95$ m are shown on the figure for $\lambda = 0.1$.

A feature of this type of model is that although it presupposes that buckling has occurred, it cannot say under what conditions buckling will actually take place. All that can be said is that buckling can only occur if $N > N_L$. For railway tracks the passage of a train is often the event which precipitates buckling.

2.2.2. Hobbs' Pipeline Model

Hobbs (1981 & 1984) has described a modified rigid-base model for pipelines, which is very similar to the model described by Kerr. There are however several major differences between the two models and these are described as follows.

(i) The thermally induced load in the pipeline N_0, is a result of both the temperature-rise and the difference between the internal and external pressure. Hobbs, in place of equation (2.6) derived the following expression for N_0:

$$N_0 = EA\alpha\Delta T + \frac{\pi D^2 p}{4}(1 - 2\upsilon) \qquad (2.13)$$

Here, p is the internal gauge pressure, D is the average diameter of the pipe and ν is Poisson's ratio. The temperature-rise ΔT, is measured relative to the temperature at which the axial load is zero, at zero gauge pressure. In most instances the pressure term is considerably smaller than the temperature term, so that the axial load is often equated with an equivalent temperature-rise ΔT_{eff}, which includes the effect of the pressure term. Thus:

$$\Delta T_{eff} = \Delta T + \frac{pD}{4tE\alpha}(1 - 2\upsilon) \qquad (2.14)$$

N_0 is calculated by substituting ΔT_{eff} into equation (2.9) or (2.10).

As an example, using the data from the case history described in Chapter 1, the effective temperature-rise of the pipeline ΔT_{eff}=77 °C. Of this figure, 72 °C is a result of the actual temperature-rise, and 5 °C is a result of the internal gauge pressure.

(ii) The vertical load on a pipeline is a result of both the self weight of the pipe and the weight of a wedge shaped section of soil above the pipe (or for sub-sea pipelines the buoyant weight of the pipe and the soil). In general the vertical load is a function of the pipe displacement, but for the Hobbs analysis it is regarded as being constant.

Palmer, Ellinas, Richards & Guijt (1990) suggest the following two equations in order to calculate the value of the constant vertical load W_0, as a function of the depth of soil cover Q. For cohesionless sand, silt and rock the vertical load W can be taken as:

$$W = W_p + \rho g Q(D + fQ) \qquad (2.15)$$

The first term W_p, is the weight (or buoyant weight) of the pipe. The second term is the weight of the wedge shaped section of soil above the pipe; ρg N/m^3, is the unit weight of the soil, Q is the height of soil above the top of the pipe, D is the outside diameter of the pipe and f is the friction angle or the slope of the wedge (taken as 0.5 for dense soils and 0.1 for loose soils). For cohesive soils W is calculated as:

$$W = W_p + cD \min[3, Q / D] \qquad (2.16)$$

where c is the shear strength of the soil. The final term is multiplied by the smaller of 3 and the ratio of the depth of soil cover / pipe diameter.

(iii) Unlike railway tracks, pipelines are normally laid with large initial imperfections, or out-of-straightness. Such imperfections are normally characterised by an imperfection length L and height H and can be of two types; a so-called "foundation" imperfection or a "geometric" imperfection. A foundation imperfection occurs when a straight length of pipe is laid in a crooked trench. A geometric imperfection is a crookedness in the actual pipe. These two types of imperfection can occur separately, or as a worst-case analysis, it is often assumed that both types of imperfection occur together, i.e. the pipe is plastically deformed to the shape of the foundation imperfection.

According to Hobbs, small imperfections have no effect on the minimum buckling temperature-rise, ΔT_L. This result arises because of the assumption that a buckle has already

formed: once a buckle has formed, the track is lifted clear of the base and is not affected by the presence of an imperfection. However, if the initial imperfection exceeds a certain critical size, snap-through buckling does not occur. Instead the amplitude of the imperfection steadily increases as the axial load increases.

(iv) For pipelines there is no external mechanism, such as the passage of a train, to disturb the pipeline from its initial position. Instead, in the absence of such a mechanism it is possible to say that buckling cannot occur below a certain load or temperature-rise, however initiated.

Apart from the differences described above, the results of the Hobbs analysis are the same as the data plotted in figures 2.3 & 2.4.

2.2.3. Dimensionless Groups for the Rigid-Base Model

In order to fix our ideas, all of the above analyses have been presented for the particular case of our model pipe. It is usual for authors to present their theoretical plots for a pipe of particular dimensions; and indeed this is understandable in relation to the assessment of a particular pipeline. There are however, strong reasons for wanting to present the entire analysis in terms of dimensionless variables. We shall do this here, even though this particular analysis does not appear in the literature.

There are many possible ways of doing this. The underlying dimensions of this problem are length and force. The example given here is based on the idea of using the diameter D as the standard length and the axial stiffness EA as the standard force. For a thin walled pipe, the flexural stiffness EI can be expressed in terms of EA as follows:

$$\frac{EI}{EA} = \frac{I}{A} = \frac{\pi r^3 t}{2\pi r t} = \frac{r^2}{2} = \frac{D^2}{8} \qquad (2.17)$$

where r is the pipe radius, D is the pipe diameter and t is the pipe wall thickness. Thus the dimensionless quantities identified by the superscript *, can be defined as follows:

$$P^* = \frac{P}{EA}, \quad W^* = \frac{WD}{EA}, \quad L^* = \frac{L}{D}, \quad H^* = \frac{H}{D},$$

$$N_0^* = \frac{N_0}{EA}, \quad \Delta N^* = \frac{\Delta N}{EA}, \quad F^* = \frac{FD}{EA}$$

All of the previous equations can now be expressed in terms of these dimensionless variables. Firstly, consider the most straightforward case, where there is no axial slippage. From equation (2.9), N^*_0 can be expressed as:

$$N_0^* = \frac{10.1}{L^{*2}} + \frac{W^{*2}L^{*6}}{989} \tag{2.18}$$

N^*_0 has a minimum value N^*_L with respect to L^* at a wavelength L^*_L such that:

$$L_L^* = \frac{2.76}{\sqrt[4]{W^*}} \tag{2.19}$$

The corresponding value of the axial load N^*_L is:

$$N_L^* = 1.77\sqrt{W^*} \tag{2.20}$$

and the dimensionless deflection H^*_L is a constant:

$$H_L^* = 1.109 \tag{2.21}$$

This is illustrated in figure 2.5, with N^* plotted versus H^*. Note that, the values of L^*_L and N^*_L depend only on W^*, and that the value of H^*_L has a constant value.

For a thin-walled pipeline and with no axial slippage, H^*_L thus corresponds to a deflection $H_L = 1.1D$. If the pipe were to be replaced by a solid round bar, some details change but we find that $H_L = 0.78D$. Similarly, for a solid rectangular bar of width b and height d $H_L = 0.9d$. Thus we find that in general for pipes and rods, $H_L \approx D$, to a first order of magnitude.

For the more general case where axial slippage occurs, the approximate friction model described by equation (2.12) can be expressed as:

$$N_0^* = \frac{10.1}{L^{*2}} + \frac{W^*L^{*7/2}F^{*1/2}}{31.45} \tag{2.22}$$

N^* has a minimum N^*_L at a wavelength L^*_L such that:

$$L_L^* = \frac{2.575}{\sqrt[11]{W^{*2}F^*}} \tag{2.23}$$

The corresponding value of the axial load N^*_L is:

$$N^*_L = 2.39\sqrt[11]{W^{*4}F^{*2}} \qquad (2.24)$$

and of the deflection H^*_L is:

$$H^*_L = 0.8455\sqrt[11]{\frac{W^{*3}}{F^{*4}}} \qquad (2.25)$$

provided that the length of pipe affected by axial slippage $L_s >> L_r$. Equation (2.22) plots figure 2.4 into a dimensionless form of general application; and again the results depend strongly on the value of λ.

2.2.4. Further Publications on the Rigid-Base Model

Various permutations of the rigid-base model have been described by other authors. Some of these are described as follows.

El-Aini (1976) describes a numerical analysis to investigate the effect of a "soft" base. He analysed a railway track in two separate parts, the central lifted-off section is analysed as one part, and the two end sections in contact with the base as the second part. He reports that his solution is virtually identical to the standard rigid-base solution and that the value of the minimum buckling load is slightly higher than for the rigid-base model. He suggests therefore, that the standard rigid-base solution be used as a lower bound solution. Note that this analysis would be similar to an elastic-base model where the track was allowed to lift-off from the base.

Kerr (1979) comments on the implication from equation (2.4), that theoretically a perfectly straight track has an infinite buckling load. He argues that this result arises from the incorrect assumption that the lateral load W is constant. The lateral load is in fact linear for small deflections, and a perfectly straight track will behave like a track on an elastic-base; with buckling occurring at the finite load corresponding to P_e from equation (2.30).

Kerr (1974) cites a considerable volume of early experimental work on railway tracks, which is published in German, French and Russian, but which has not been reviewed for this chapter. He gives no indication of how well the track buckling data corresponds with the rigid-base model.

Ju & Kyriakidies (1988) describe a numerical analysis to investigate the effect of initial imperfections on the buckling behaviour of a pipeline. They describe three types of imperfection. These are illustrated in figure 2.6, and are described as follows:

A prop type of imperfection, as illustrated in (a), occurs because of the presence of an object under the pipe; the pipe having a single point of contact with the imperfection. A partially contacting type of imperfection, as illustrated in (b), occurs if the pipe is in contact with the foundation along a partial section of the imperfection length. A fully contacting imperfection is shown in (c) and occurs if the pipe is in full contact with the foundation along the entire length of the imperfection.

These authors report similar conclusions to those of Hobbs. The presence of small initial imperfections does not affect the minimum buckling load; and snap-through buckling will only occur for imperfections which are smaller than a certain critical size. For larger imperfections, the size of the imperfection grows steadily as the temperature increases, but buckling does not occur.

The effect of imperfections on the buckling behaviour of a pipeline, according to Ju & Kyriakidies, is shown in figure 2.7. The temperature-rise ΔT, is plotted versus the uplifted length L, for various sizes of initial imperfection H_0. Note, that in this example, the value of $W_0=0.5$ N/m corresponds to an uncovered pipeline. According to their analysis, no movement of the pipeline occurs until the temperature-rise $\Delta T=\Delta T_u$. At this point the pipeline starts to deflect and the wavelength L steadily increases as the temperature-rise increases. For small imperfections the temperature-rise reaches a peak value at $\Delta T=\Delta T_c$, and snap-through buckling occurs. For larger imperfections there is no peak value of the temperature-rise ΔT_c and no snap-through buckling occurs. If the shape of the imperfection is changed, the effect is to alter the values of ΔT_u and ΔT_c, but ΔT_L remains the same.

It is possible to use the value of ΔT_u as a maximum, permissible temperature-rise for design purposes, although generally the value of ΔT_u is so low as to be impractical. Instead, the authors suggest that a maximum allowable displacement ΔH_d, should be used as the design criterion. Note that, $\Delta H_d=H-H_0$. If ratcheting, (the incremental upward movement of the pipe

due to cycling of the axial load) is likely to be a problem, the value of ΔH_d, should be smaller than the proportional limit of the soil.

An example of the use of this type of design method is shown in figure 2.8, and is taken from Pedersen & Jensen (1988), using the authors' own data. The maximum temperature-rise ΔT is plotted versus the minimum depth of soil cover Q, for various heights and lengths of imperfection. The authors have specified the maximum pipe displacement due to the axial load as being 20 mm, for the particular pipeline in question. This figure would obviously vary for each instance. The vertical load W corresponding to a particular depth of soil cover Q, can be calculated from equations (2.15) or (2.16). For a given temperature-rise ΔT, the minimum depth of soil cover required to prevent buckling, increases as the imperfection amplitude and wavelength increases.

Klever, van Helvoirt & Sluyterman (1990) have developed a dedicated finite element package named UPBUCK which allows pipeline imperfections of any shape to be analysed. A weakness of previous analyses is that the imperfections were assumed to be regular and symmetrical. The UPBUCK package runs on a PC and allows the designer to analyse the behaviour of fully buried, partly buried and unburied pipelines and to examine the effect of continuous or intermittent rock dumping or residual lay tension. The designer is able to allow for the following parameters:

The elastic and plastic pipe material behaviour.

The non-linear pipeline response at large deflections.

The interaction of the pipe with the foundation and the soil cover.

Irregular pipeline and soil cover profiles.

Both vertical and inclined buckling.

The program calculates the deflection of the pipe as the temperature is increased by small increments. It is found from many runs of the program that, generally, there is no displacement of the pipe until the temperature-rise is close to the buckling temperature. At that point, the pipe starts to displace and the onset of buckling is rapid.

Allan (1968) and Baldry (1973) performed a series of experiments to investigate the buckling behaviour of a compressed strip with a single prop imperfection of height H and

length L. Allan used strips of shim steel which were weighted to increase the vertical loading. Baldry used strips of silicone rubber, Perspex, aluminium and brass, with no extra weight. Both authors report that buckling occurs at a load close to the rigid-base buckling load P_r, as calculated from equation (2.4).

According to theory, the wavelength of a prop imperfection of height H, vertical load W and zero axial load, is approximately 1.3 times the rigid-base wavelength L_r; as calculated from equation (2.5) and using the same values of W, EI and H. There is a localised reaction load R =2WL/3 at the prop. If an axial load is applied, the length of the imperfection will shorten and the reaction load at the prop will decrease. Buckling occurs when the axial load equals the rigid-base buckling load P_r, as calculated from equation (2.4). At that point, the length of the uplifted section should equal the rigid-base buckling length L_r, and the reaction load at the prop should have reduced to zero.

2.2.5. Summary of the Rigid-Base Model

The rigid-base model provides a useful model of the vertical buckling of railway tracks. The model enables the post-buckling behaviour of the track to be analysed and the stable and unstable post-buckling configurations to be calculated. For this purpose, the model assumes that a buckle has already formed: the track has lifted clear of the base and the vertical load due to the weight of the track is constant.

The rigid-base model is unable to tell us anything about how buckling actually occurs. For the analysis of a railway track this is unimportant as buckling is usually initiated by the passage of a train. By using the rigid-base model, it is possible to calculate a safe temperature-rise below which buckling should not occur.

The rigid-base model is unsatisfactory for the analysis of pipeline buckling because in that case buckling is initiated as a result of the pipe moving upwards through the soil when an axial load is applied. The movement of the pipe through the soil is a function of various pipe and soil parameters. These include: the flexural stiffness of the pipe EI, the height of the initial imperfections on the pipe H_0, and the relationship between the forces exerted on the pipe by the soil and the pipe displacement. This is a similar situation to the analysis of the lateral

buckling of railway tracks, where the track remains in contact with the soil and the rigid-base model is unsatisfactory.

Several attempts have been made to modify the rigid-base model in order to overcome its shortcomings. In general, these have involved increasingly complex numerical solutions which allow for various non-linearities in the system, but which appear to produce a broadly similar type of result to the standard rigid-base analysis.

The important point then in the analysis of pipeline buckling is to determine the conditions under which buckling is initiated, rather than the post-buckling equilibrium conditions. A much more satisfactory type of analysis is the modified elastic-base model proposed by Tvergaard and Needleman (1981), and which is described in the next section.

2.3. The Elastic-Base Model

2.3.1. Kerr's Railway Track Model

Kerr (1974) also describes an "elastic-base" model of the railway track. The track is modelled as a continuous weightless beam supported on a linear, elastic base. This is shown in figure 2.9.a. The beam has flexural stiffness EI Nm^2 and is compressed by an axial load P N. The base has a vertical elastic stiffness K N/m^2, and exerts a vertical force on the beam proportional to and in the opposite direction from the vertical displacement. The beam is assumed to be initially straight, and to remain in full contact with the elastic-base at all times. The overall x, y co-ordinate system is shown in the figure. The forces and moments acting on an element of length dx are shown in figure 2.9.b. From small deflection beam theory the governing equation for this arrangement can be written as:

$$EI\frac{d^4y}{dx^4} + P\frac{d^2y}{dx^2} + Ky = 0 \qquad (2.26)$$

The difference between this and equation (2.1) is that the downwards force acting on the beam is no longer a constant self weight, as in the rigid-base model, but is now proportional to the vertical displacement y. The simplest solution of this equation has the form:

$$y = V \sin\left(\frac{2\pi x}{L}\right) \qquad (2.27)$$

which is an indefinitely extended sine wave of amplitude V and wavelength L. This corresponds to the continuous buckling mode shown in figure 2.10.e. Note that the height H of the rigid-base buckle is twice the value of V, i.e. H=2V. Substituting for y, into equation (2.26) gives the following expression for the buckling load P as a function of L:

$$P = \frac{\pi^2 EI}{(L/2)^2} + \frac{K(L/2)^2}{\pi^2} \qquad (2.28)$$

The buckling load P, has a minimum value P_e with respect to L, when L is given by:

$$L_e = 2\pi\sqrt[4]{\frac{EI}{K}} \qquad (2.29)$$

The corresponding value of P_e is:

$$P_e = 2\sqrt{KEI} \qquad (2.30)$$

The subscript $_e$ has been used here to denote the elastic-base model. In this analysis, the track is assumed to be initially straight, and to remain straight until the elastic buckling load P_e is reached. At that point it buckles in the mode described above and with the amplitude V being indeterminate. The values of L_e and P_e are constant. If EI and $P=EA\alpha\Delta T$, are known for a particular track, equation (2.30) can be used to calculate the minimum base stiffness required to prevent buckling. Kerr comments that neglecting the weight of the beam does not affect the result of the analysis provided that the elastic response of the base is linear.

Unfortunately this type of model doesn't agree well with the observed behaviour of real tracks. The differences between theory and observation are listed as follows.

(i) Real tracks lift-off from the base, and so do not remain in full contact.

(ii) For a real soil, such as a coarse granular fill, the response of the soil is linear for small displacements only. For large displacements the response is in-elastic and reaches a virtually constant plateau value.

(iii) A real track has initial imperfections.

(iv) Buckling tends to occur as a single buckle, as shown in figure 2.10.a, rather than the periodic mode shown in figure 2.10.e.

$$y = V \sin\left(\frac{2\pi x}{L}\right) \qquad (2.27)$$

which is an indefinitely extended sine wave of amplitude V and wavelength L. This corresponds to the continuous buckling mode shown in figure 2.10.e. Note that the height H of the rigid-base buckle is twice the value of V, i.e. H=2V. Substituting for y, into equation (2.26) gives the following expression for the buckling load P as a function of L:

$$P = \frac{\pi^2 EI}{(L/2)^2} + \frac{K(L/2)^2}{\pi^2} \qquad (2.28)$$

The buckling load P, has a minimum value P_e with respect to L, when L is given by:

$$L_e = 2\pi\sqrt[4]{\frac{EI}{K}} \qquad (2.29)$$

The corresponding value of P_e is:

$$P_e = 2\sqrt{KEI} \qquad (2.30)$$

The subscript $_e$ has been used here to denote the elastic-base model. In this analysis, the track is assumed to be initially straight, and to remain straight until the elastic buckling load P_e is reached. At that point it buckles in the mode described above and with the amplitude V being indeterminate. The values of L_e and P_e are constant. If EI and $P=EA\alpha\Delta T$, are known for a particular track, equation (2.30) can be used to calculate the minimum base stiffness required to prevent buckling. Kerr comments that neglecting the weight of the beam does not affect the result of the analysis provided that the elastic response of the base is linear.

Unfortunately this type of model doesn't agree well with the observed behaviour of real tracks. The differences between theory and observation are listed as follows.

(i) Real tracks lift-off from the base, and so do not remain in full contact.

(ii) For a real soil, such as a coarse granular fill, the response of the soil is linear for small displacements only. For large displacements the response is in-elastic and reaches a virtually constant plateau value.

(iii) A real track has initial imperfections.

(iv) Buckling tends to occur as a single buckle, as shown in figure 2.10.a, rather than the periodic mode shown in figure 2.10.e.

(v) The measured buckling loads are considerably lower than P_e.

2.3.2. Tvergaard & Needleman's Model.

A more useful model has been proposed by Tvergaard & Needleman (1981). They proposed a modified version of the elastic-base model, in which the track has an initial sinusoidal imperfection of amplitude V_0 and length L, and the response of the soil is non-linear. In their analysis, the authors used empirical soil-response data which had been measured from an actual railway track. They reported that their computed results were in reasonable agreement with the observed experimental results; regarding both the buckling loads and the buckling wavelengths. They also commented that the buckling loads are independent of the value of the axial-friction force acting between the track and the soil.

The authors analysis has been duplicated in this Chapter using a simplified version of their model. Despite the small differences from the model described by Tvergaard & Needleman, the results of the two analyses are qualitatively the same.

For the modified Tvergaard and Needleman model, the track or pipe is modelled as an elastic beam of flexural rigidity EI, and is compressed by an axial load P. The beam has an initial sinusoidal imperfection of amplitude V_0 and wavelength L, and is supported on a base with an exponential soil-response, similar to the type shown in figure 2.11. From small deflection beam theory, the governing equation can be written as:

$$EI\left(\frac{d^4y}{dx^4} - \left.\frac{d^4y}{dx^4}\right|_{y_0}\right) + P\frac{d^2y}{dx^2} + W_{(y-y_0)} = 0 \qquad (2.31)$$

Here $\left.\frac{d^4y}{dx^4}\right|_{y_0}$ is the fourth derivative of the initial profile of y with respect to x. The vertical load $W_{(y-y_0)}$ is some arbitrary function of the displacement $\Delta y = y - y_0$. In order to proceed to a solution, it is assumed that y is a sine function of the form:

$$y = V\sin\left(\frac{2\pi x}{L}\right) \qquad (2.32)$$

For simplicity, the distribution of the vertical load along the length of the pipe, has been approximated by a sinusoidal profile. Thus, equation (2.31) can be re-written as:

$$\left[EI\left(\frac{2\pi}{L}\right)^4(V-V_0)-P\left(\frac{2\pi}{L}\right)^2 V+W_{(V-V_0)}\right]\sin\left(\frac{2\pi x}{L}\right)=0 \quad (2.33)$$

Re-arranging and dividing by sin(2πx/L), the axial load P can be expressed as:

$$P=\frac{W_{(V-V_0)}}{V}\left(\frac{2\pi}{L}\right)^2+EI\frac{(V-V_0)}{V}\left(\frac{L}{2\pi}\right)^2 \quad (2.34)$$

Adding the geometric shortening term, N_0 can be expressed as:

$$N_0=\frac{W_{(V-V_0)}}{V}\left(\frac{2\pi}{L}\right)^2+E\left(\frac{I(V-V_0)}{V}+A\left(V^2-V_0^2\right)\right)\left(\frac{L}{2\pi}\right)^2 \quad (2.35)$$

The geometric shortening term is proportional to V^2.

The values of P and N_0 are plotted against V in figure 2.12, for a half-wavelength L/2=0.6 m, and showing the effect of variations in the amplitude of the initial imperfection. It can be seen that the N_0 curves rise up above the P curves, due to the geometric shortening term which is described in Section 2.2.1. As the imperfection level increases the peak values of both P and N_0 decrease. There is an intermediate imperfection level at which there is a peak in P but no peak in N_0, and for large imperfections, neither P nor N_0 have a peak.

Figure 2.13 illustrates the effect of varying the imperfection half-wavelength L/2. In this case, V_0=0.3 mm. For short wavelengths, as in (a) where L/2=0.4 m, neither P nor N_0 has a peak. As the wavelength increases, first a peak appears in P, as in (b) where L/2=0.57 m, but with no peak in N_0. If the wavelength is increased slightly more, as in (c) where L/2=0.63 m, a peak has also appeared in N_0. For longer wavelengths, as in (d) where L/2=0.8 m, the size of the two peaks increases as the wavelength increases.

In general, buckling due to restrained thermal expansion can only occur at a peak in the value of N_0. Thus, from the example shown in the previous figure, the lowest value of N_0 at which buckling can occur is N_0=115 N, and this corresponds to a half-wavelength L/2=0.63 m. However, Tvergaard & Needleman have demonstrated that when multiple imperfections exist, a "localisation" phenomenon can occur, and that buckling is then initiated at a peak in the value of P.

Such a localisation occurs when one of a series of neighbouring imperfections reaches a peak on the P curve. That imperfection then tends to become unstable and localises, i.e. it grows at the expense of its neighbours. This has the effect of shifting the positions of the P and N_0 curves as shown by the dashed lines in figure 2.13.b, so that both lines are steeper and a peak is formed in the N_0 curve.

The peak value of P varies with the wavelength, and it has a minimum value which can be regarded as the buckling load. From the example given, the shortest half-wavelength at which a peak occurs is at $L_t/2=0.54$ m, and this corresponds to a peak load $P=107$ N. The minimum peak value $P_t=105$ N occurs at a slightly longer half-wavelength, $L_t/2=0.57$ m. The subscript $_t$ has been used here to denote the values from the Tvergaard & Needleman analysis. The maximum allowable temperature-rise ΔT_t can be calculated by dividing P_t by $EA\alpha$.

The calculated values of P_t, are shown plotted against the imperfection amplitude V_0, in figure 2.14. As can be seen, the value of P_t decreases as the size of the imperfection increases. The Tvergaard and Needleman model assumes that the wavelength of the imperfection equals the buckling wavelength. This is the critical wavelength, at which a particular imperfection is most likely to buckle. In most cases, the actual wavelength of an imperfection will be different to the buckling wavelength; which has the effect of reducing the likelihood of buckling occurring.

Some of the buckling modes which can occur in vertical and lateral buckling are shown in figure 2.10. Vertical buckling generally occurs as a single symmetrical buckle as in (a), because it is easier for the pipeline or track to deflect upwards rather than downwards. For lateral buckling, the pipeline or track can deflect to either side with equal ease. The preferred lateral buckling mode can be either the anti-symmetric double mode in (b), or the symmetric triple mode in (c). The continuous, or periodic buckling mode predicted by the elastic-base model is shown in (*e*).

2.4. Palmer's Maximum Vertical Load Model

Palmer, Ellinas, Richards & Guijt (1990), have proposed a rather different model. Their idea is to calculate the maximum vertical load W N/m required to hold an imperfection profile in equilibrium and to compare this with the restraining force provided by the soil. To do this they have taken a set of data points which have been calculated using the UPBUCK program, and have plotted these in a dimensionless form. The resulting plot yields a set of generalised curves which can be used for all cases.

In general, the required vertical load W, for a particular profile shape can be calculated by an equation of the form:

$$W = AHP\left(\frac{\pi}{L}\right)^2 - BHEI\left(\frac{\pi}{L}\right)^4 \qquad (2.36)$$

where A & B are unknown constants, H is the height of the imperfection, P is the buckling load and EI is the flexural stiffness of the pipe. The first term of the equation is a simple arch term, and the second term is a reduction in W due to the flexural stiffness of the pipeline. The equation can be rewritten in a dimensionless form as:

$$\Phi_w = \frac{A}{\Phi_L^2} - \frac{B}{\Phi_L^4} \qquad (2.37)$$

where Φ_w is a dimensionless vertical load:

$$\Phi_W = \frac{WEI}{HP^2} \qquad (2.38)$$

and Φ_L is a dimensionless length:

$$\Phi_L = \frac{L}{2}\left(\frac{P}{EI}\right)^{1/2} \qquad (2.39)$$

Data from the UPBUCK program has been used to determine the value of the constants A and B, for each of the three types of imperfection illustrated in figure 2.6. The three generalised curves are shown plotted in figure 2.15, and correspond to the following three regions:

Region 1. $\Phi_w = 0.0646$ for $\Phi_L < 6$

Region 2. $\Phi_w = 5.68 / \Phi_L^2 - 88.35 / \Phi_L^4$ for $6 < \Phi_L < 9$

Region 3. $\Phi_w = 9.6 / \Phi_L^2 - 343 / \Phi_L^4$ for $9 < \Phi_L$

Each of the three curves represents a different relationship between Φ_w and Φ_L, depending on the particular type of imperfection. Region 1 represents an isolated prop imperfection. Regions 2 and 3 represent fully contacting imperfections; with prop profile and rigid-base profile respectively. The general relationship between Φ_w and Φ_L could also be represented by a single descending curve, and neglecting region 1.

The results from the UPBUCK program can thus be presented in a generalised, dimensionless form. In theory, the data from any pipeline imperfection should plot on to one of the three curves, so that if for example H, L, W and EI are known, then the buckling load P can be determined.

The Palmer plot is one method of presenting the buckling data in dimensionless form. An alternative dimensionless plot has been described previously in Section 2.2.3. The advantage of the Palmer plot is that it allows for the effect of varying the wavelength of the imperfection, something which the previous dimensionless plot, does not do.

The rigid-base model can be represented by a single data point, since it turns out that the values of Φ_w and Φ_L are both constant. From equation (2.4), $\Phi_w = 0.0637$ and from equation (2.3), $\Phi_L = 4.493$. This is because of the fixed relationship between H, EI, L & P.

It can be seen from the figure, that the rigid base data point lies within the Palmer curves. Thus, the UPBUCK data, which is presented by the Palmer curves, is essentially similar to the standard rigid-base data. However, the Palmer plot may be a useful method for presenting the data from the Tvergaard and Needleman model, as it allows for the effect of variations in the imperfection wavelength.

2.5. Figures

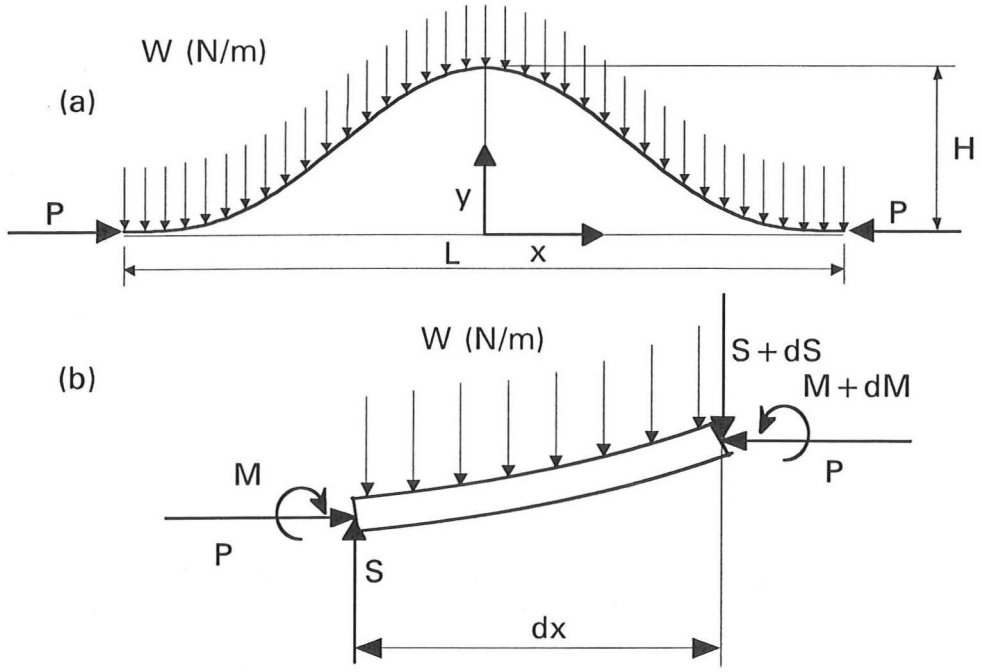


Figure 2.1. A schematic diagram of the rigid-base model showing: (a) The beam profile with constant vertical load W. (b) The forces and moments acting on an element of length dx. Note: the vertical scale is exaggerated.

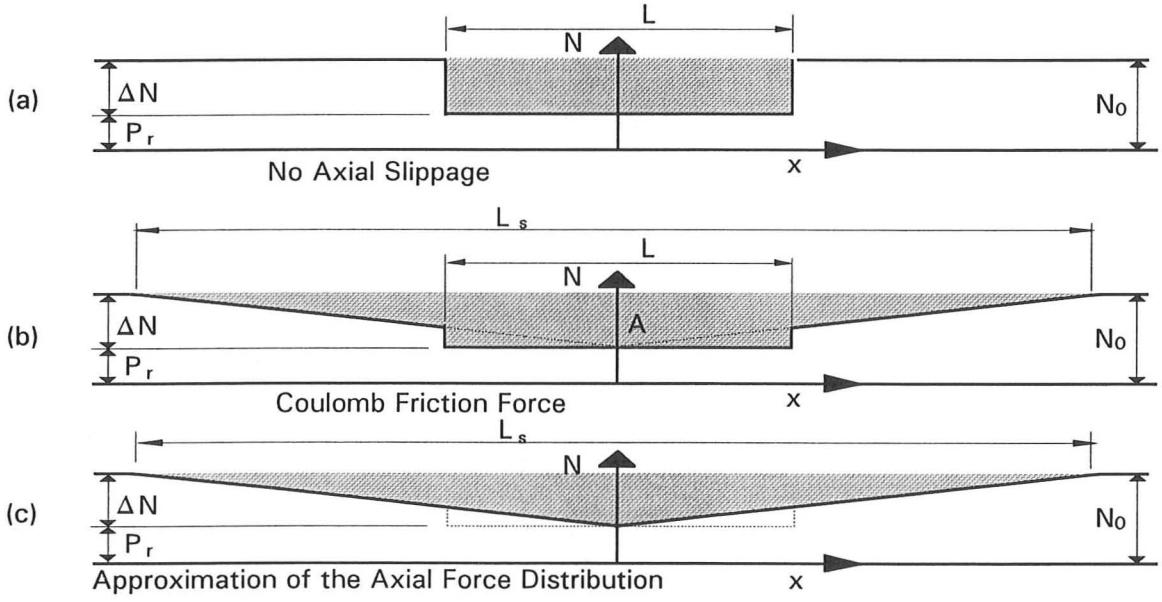


Figure 2.2. The axial-load distribution in a buckled pipeline corresponding to the following friction models: (a) No axial slippage. (b) Coulomb axial friction. (c) The approximate friction model, provided that $L_s >> L$. Note: the vertical scale is exaggerated.

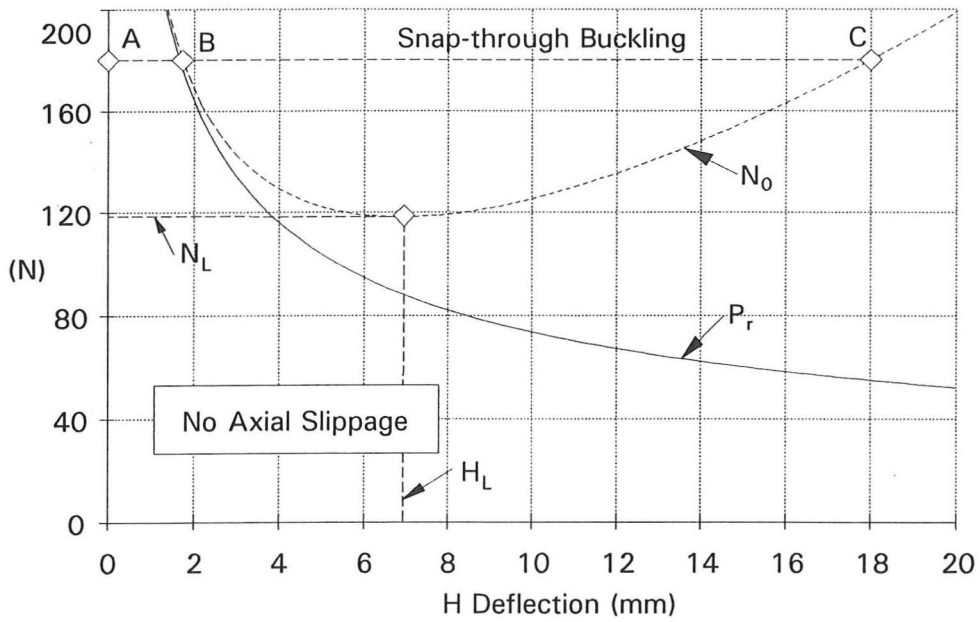


Figure 2.3. The buckling load according to the rigid-base model with no axial slippage. The thermally induced load N_0 and the buckling load P_r, are plotted versus the deflection H. The minimum buckling load $N_L \approx 118$ N and $H_L \approx 7$ mm. W=1.1 N/m, EI=3.131 Nm^2, EA=650 kN and $\alpha = 9.4 \times 10^{-6}$ $^oC^{-1}$.

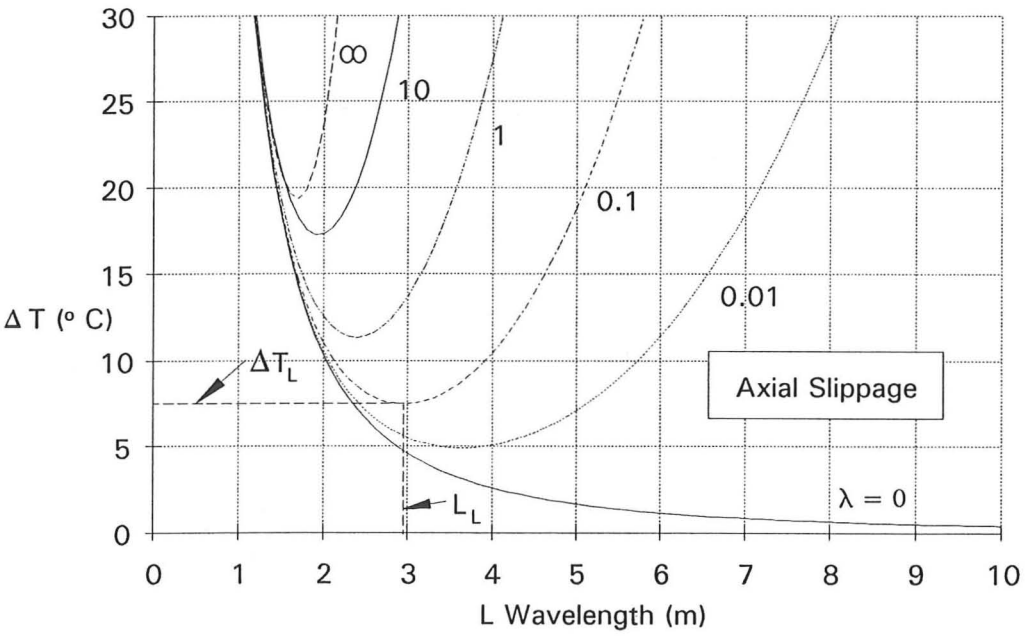


Figure 2.4. The effect of axial friction on the rigid-base model. The temperature rise ΔT is plotted versus the buckle wavelength L, for various values of the Coulomb friction coefficient λ using the approximate friction model described by equation (2.12). EI=3.131 Nm^2, EA=650 kN, W=1.1 N/m, $\alpha = 9.4 \times 10^{-6}$ $^oC^{-1}$.

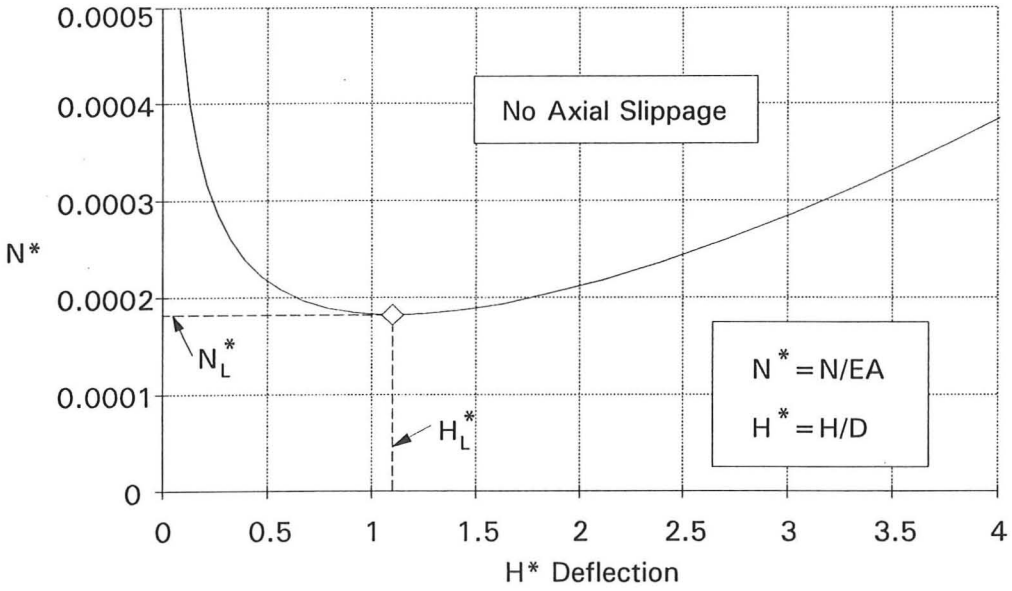


Figure 2.5. A dimensionless plot of the data from the rigid-base model. $H^*_L = 1.109$ & $N^*_L = 1.77/\sqrt{W^*}$.

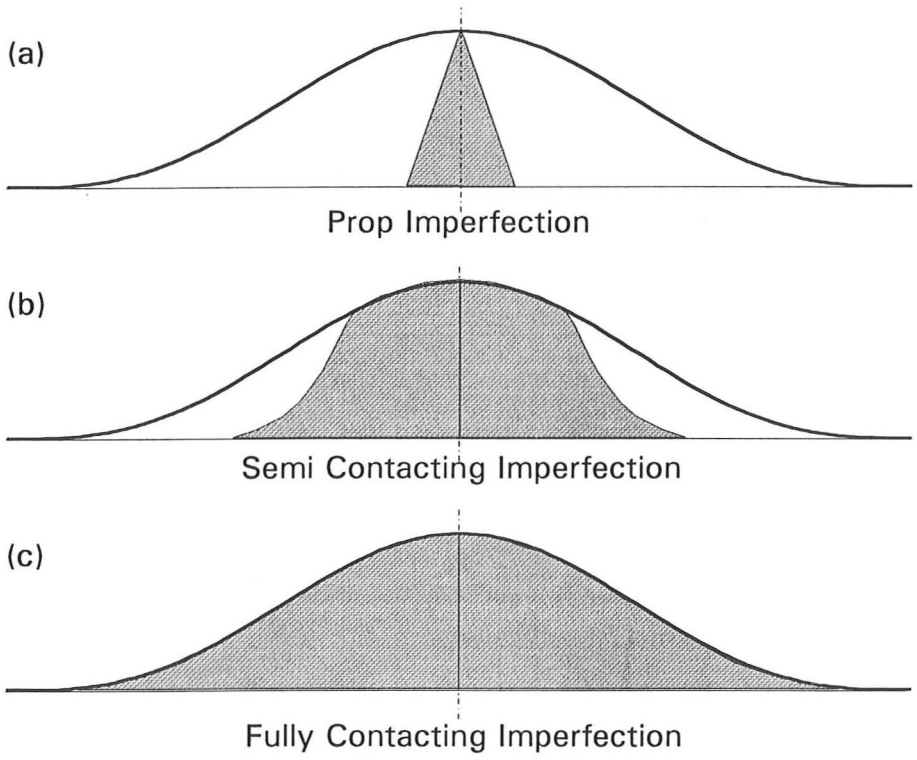


Figure 2.6. The three types of imperfections: (a) a prop imperfection, (b) a semi-contacting imperfection, and (c) a fully-contacting imperfection.

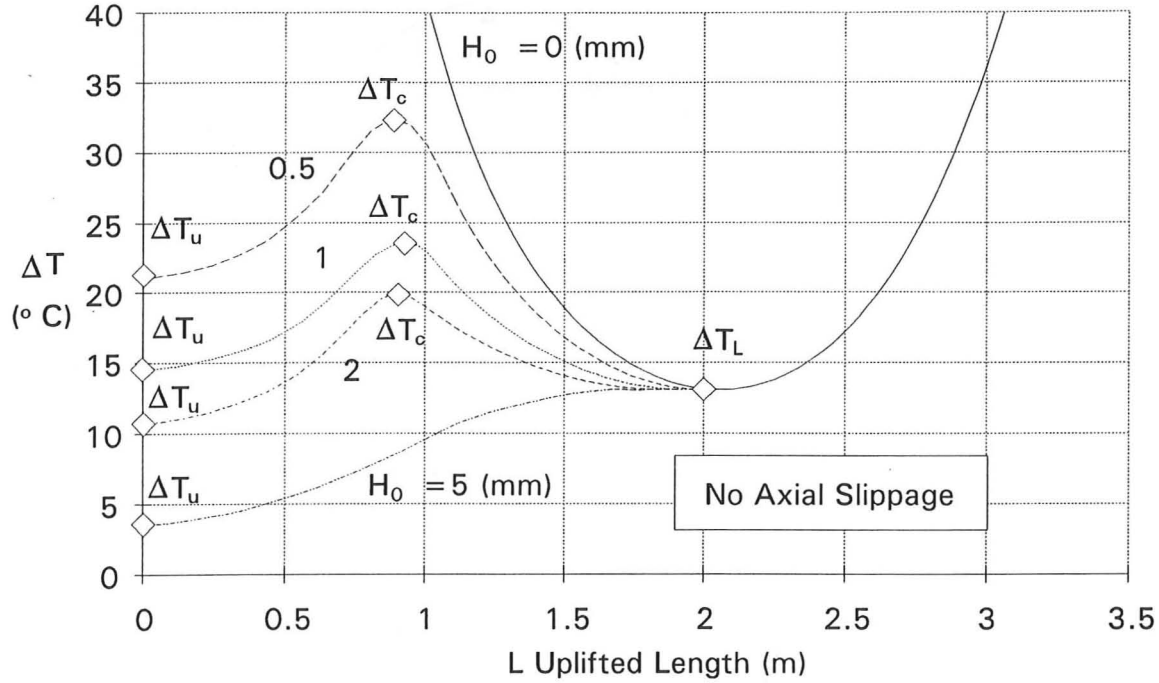


Figure 2.7. The effect of imperfections according to Ju & Kyriakidies' model (1988). The temperature rise ΔT is shown plotted against the uplifted buckle length L, for various sizes of initial imperfection H_0=0.5 to 5.0 mm. EI=3.131 Nm^2, W=0.5 N/m, EA=650 kN and α =9.4 x10^{-6} $^oC^{-1}$. $T_L \approx 13$ °C. Note the value of W_0 corresponds to an uncovered pipe.

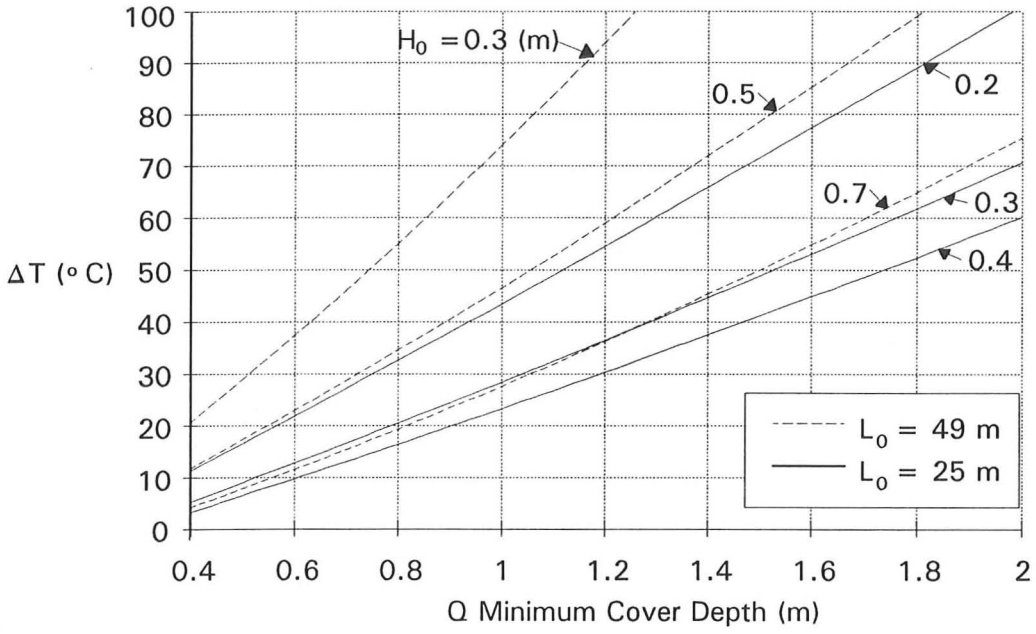


Figure 2.8. Pedersen & Jensen's maximum displacement model (1988). The maximum temperature rise ΔT °C is plotted versus the minimum depth of soil cover Q, for various imperfection heights and wavelengths, using the authors data. ΔH_{max}=20 mm, D=0.214 m, t=0.0142 m, E=207 GPa, α=11 x10^{-6} $^oC^{-1}$.

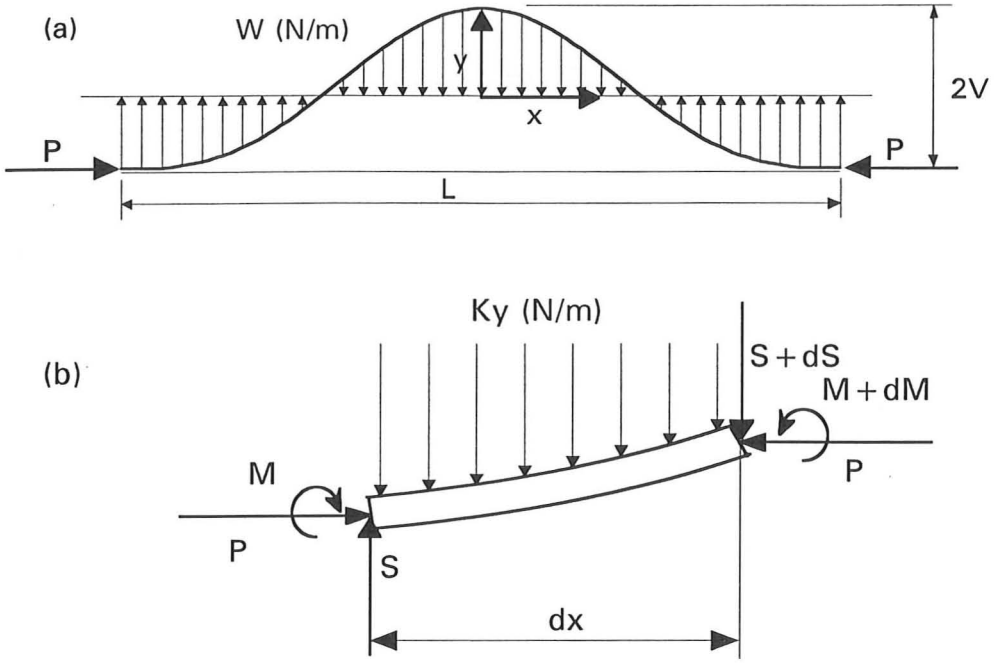


Figure 2.9. A schematic diagram of the elastic-base model showing (a) The beam profile with the vertical load W, proportional to and in the opposite direction to the displacement. (b) The forces and moments acting on a beam element of length dx.

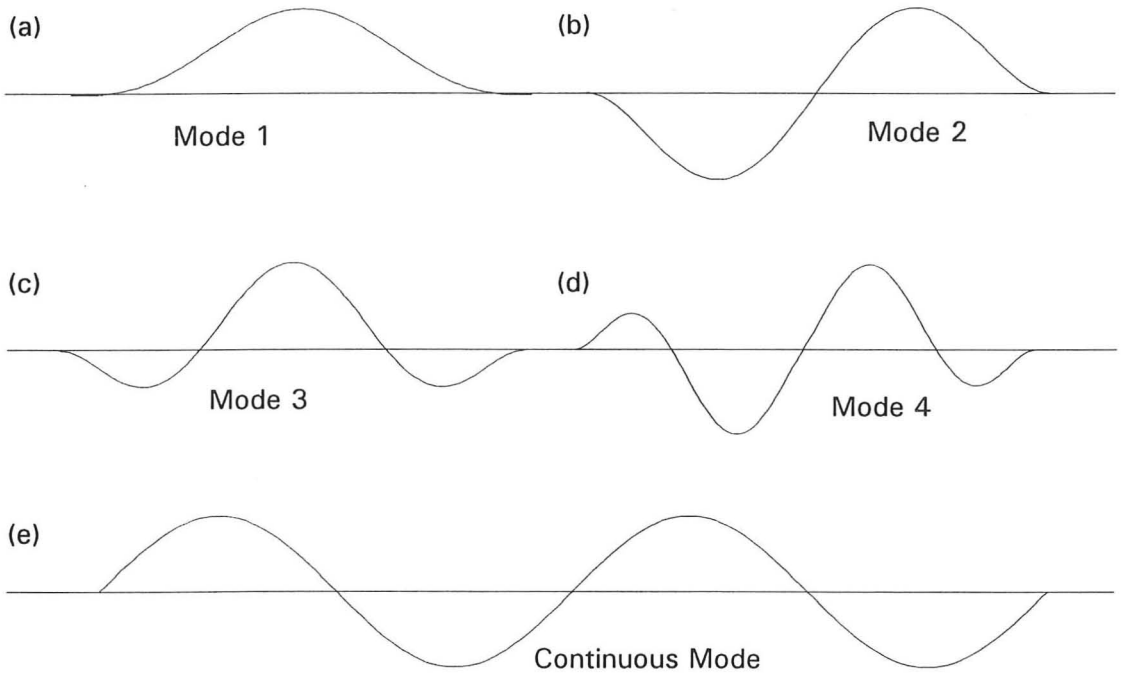


Figure 2.10. A schematic diagram of the buckling mode-shapes. (a) the single mode (b) the double mode (c) the triple mode (d) the quadruple mode and (e) the continuous or periodic mode.

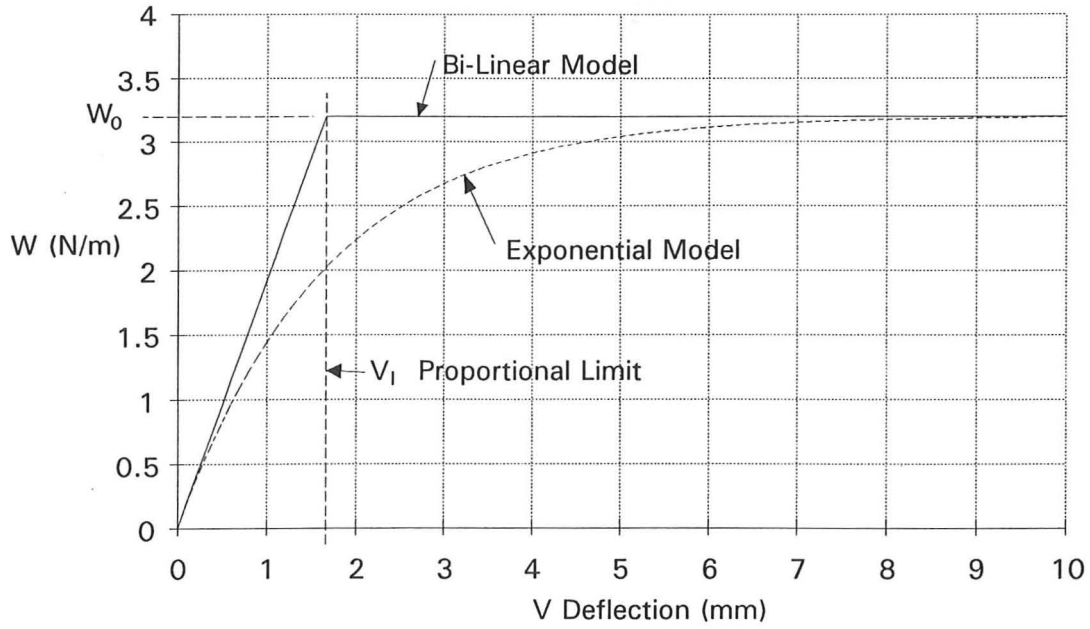


Figure 2.11. Two soil-response models. (a) The bilinear model. $W=K\Delta V$ for $\Delta V < V_I$, where $K=W_0/V_I$, & $W=W_0$ for $V \geq V_I$. (b) The exponential model. $W=W_0(1-\exp(-\Delta V/V_I))$. $W_0=1.1$ N/m & $V_I=0.1$ mm.

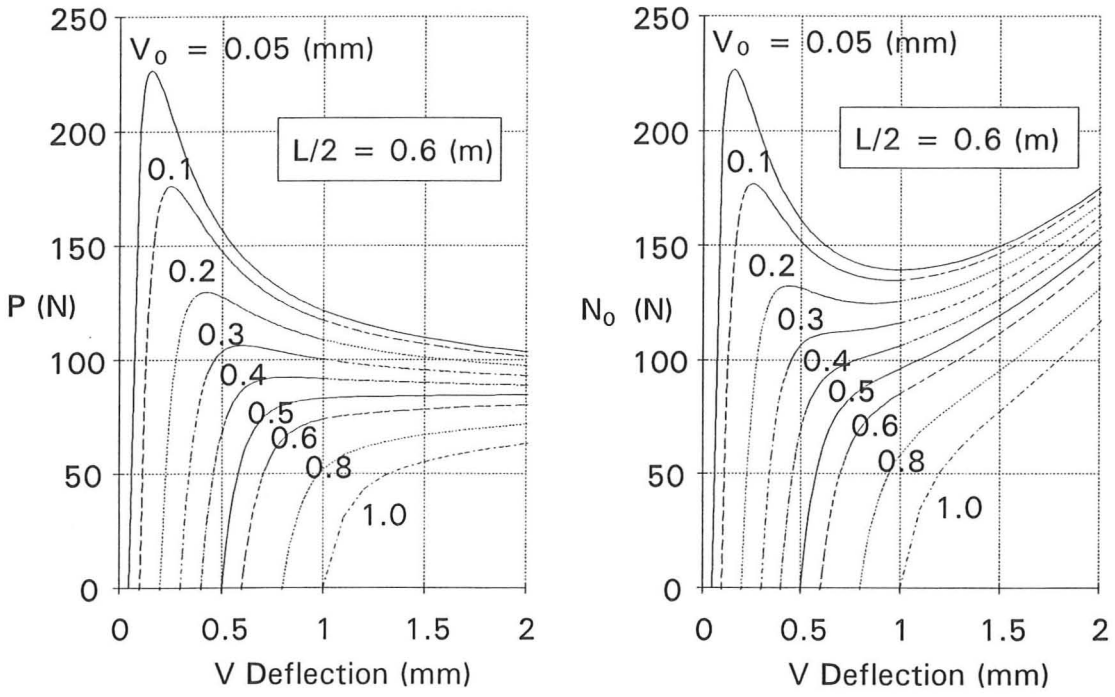


Figure 2.12. The effect of initial imperfections according to Tvergaard & Needleman's model (1981). The soil response is assumed to be exponential, as shown in figure (2.11). $W_0=1.1$ N/m, $X_I=0.1$ mm, $EI=3.131$ Nm^2, $EA=650$ kN, $\alpha=9.4 \times 10^{-6}$ $^oC^{-1}$.

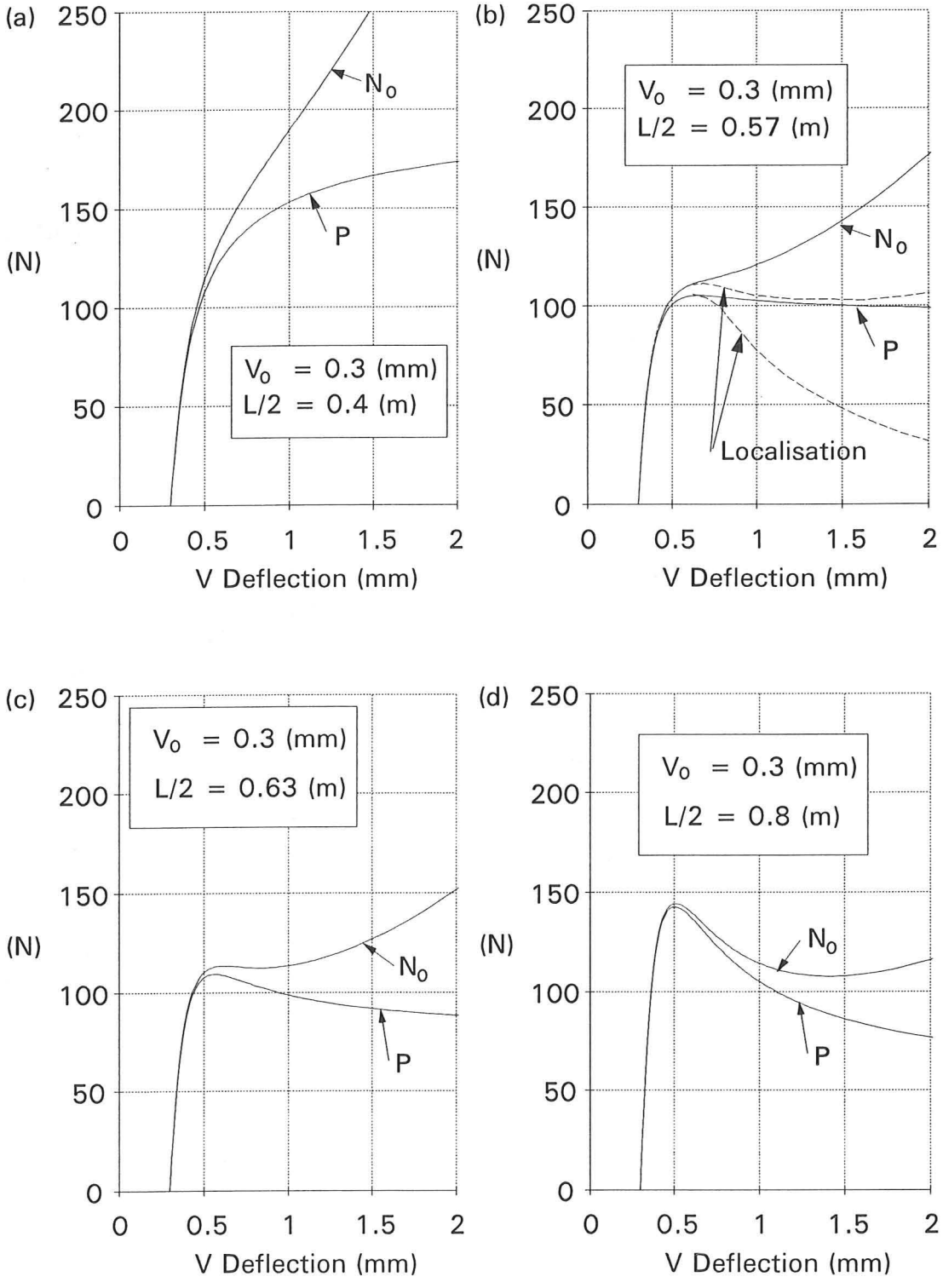


Figure 2.13. The effect of varying the wavelength. P and N_0 are plotted versus the deflection V for the half-wavelengths shown, with an exponential soil response model. W_0=1.1 N/m, V_1=0.1 mm, EI=3.131 Nm^2, EA=650 kN, α=9.4 x 10^{-6} $^oC^{-1}$.

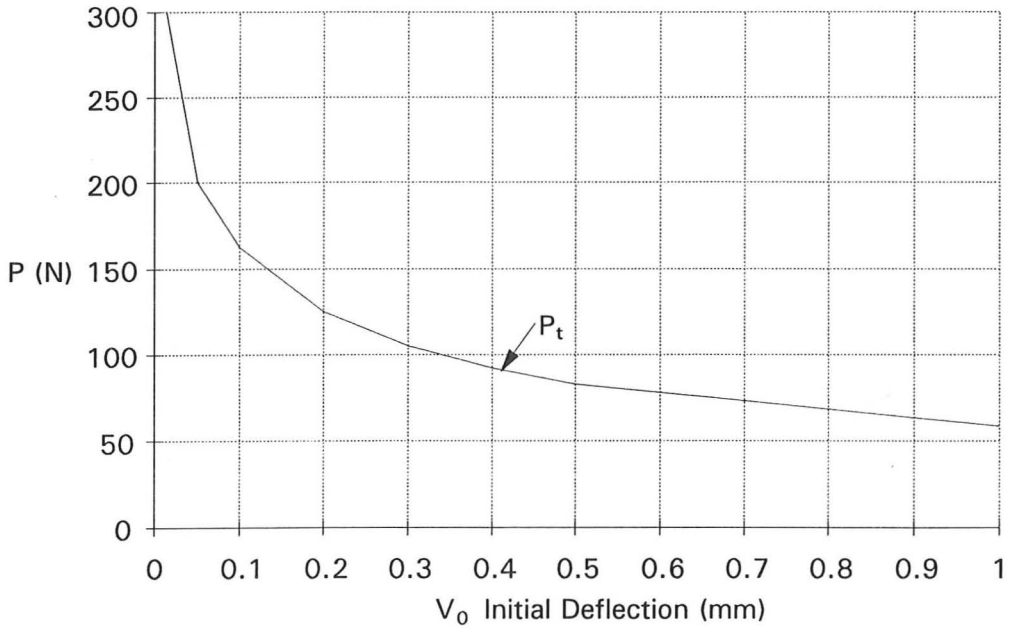


Figure 2.14. The buckling load according to Tvergaard & Needleman's model. The value of P_t is plotted against V_0, noting that $H_0=2V_0$. The soil response is assumed to be exponential, as shown in figure (2.11). $W_0=1.1$ N/m, $V_1=0.1$ mm, EI=3.131 Nm^2, EA=650 kN and α = 9.4 x 10^{-6} $^oC^{-1}$.

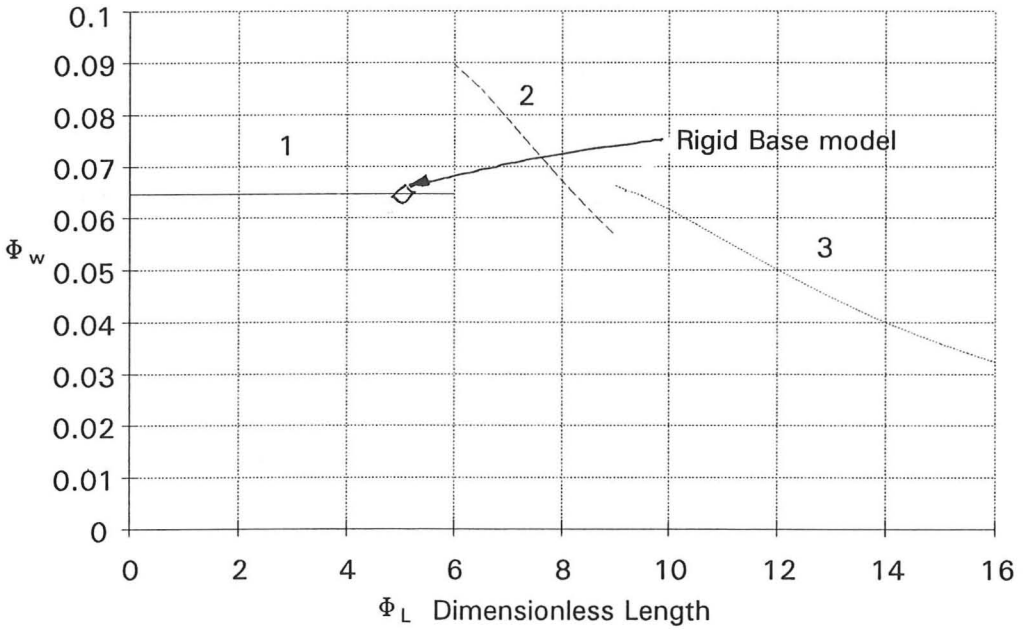


Figure 2.15. (a) The Palmer model of the maximum vertical load. The dimensionless vertical force $\Phi_w = WEI/HP^2$, is plotted versus the dimensionless wavelength $\Phi_L = \frac{L}{2}\sqrt{(P/EI)}$. The rigid base model is represented by a single data point, $\Phi_w = 0.0637$ and Φ_L, = 4.493

3. Theory

3.1. Introduction

This Chapter describes three simple models, which have been developed in the course of this Thesis.

The first model is a simplified version of the Tvergaard and Needleman model, which was described previously in Chapter 2. According to this model, both the buckling wavelength and the buckling load can each be expressed by simple equations in terms of: the flexural stiffness of the pipe EI Nm^2, the plateau value of the vertical soil force W_0 N/m, and the amplitude of the initial imperfections on the pipe V_0 m. The buckling load and the buckling wavelength are virtually independent of the shape of the soil-response curve.

A second model describes the effect of variations in the wavelength of an imperfection. According to the buckling model described above, there is a preferred relationship between the amplitude of an imperfection and the buckling wavelength. The model presupposes that buckling is most likely to occur when the wavelength of an imperfection matches the buckling wavelength, and is less likely when the wavelengths do not match. The tendency for a particular imperfection to buckle is described by the effective amplitude. For a particular size of imperfection, the effective amplitude decreases and the buckling load increases, as the wavelength of the imperfection increases.

An example is given in Section 3.3, of the combined use of both the effective amplitude model and the simplified buckling model.

A third model is proposed as a method for estimating the size of the initial imperfections on the test pipe used in the experiments. A problem arises because the remote-sensing system used in the experiments, is not sufficiently accurate to measure the actual size of the imperfections. Instead, the approximate size of the imperfections must be estimated from the experimental data. The method proposed, is to use a Southwell plot to compare the experimental data with theoretical data, which has been calculated from a numerical Tvergaard and Needleman type of model, and to thus estimate the size of each imperfection.

3.2. The Simplified Buckling Model

It is apparent from the review of the literature in Chapter 2, that the Tvergaard and Needleman model (1981), is the most satisfactory model of observed buckling behaviour. The reason for this is that the Tvergaard and Needleman model most accurately accounts for the effect of the non-linear interaction between the pipe and the soil.

In their original analysis, Tvergaard and Needleman used a numerical procedure so that they could include the experimental data on the force-displacement response of a real track. They found that their results agreed reasonably well with the observed buckling behaviour of real tracks, both in terms of the buckling loads and the buckling wavelengths.

Surprisingly, the soil-response data can be approximated by a simple bilinear model, without significantly affecting the results of the analysis. This has been done in the simplified buckling model, which is presented here as a simplified analytical form of the Tvergaard and Needleman model. It is described as follows.

As for the modified Tvergaard and Needleman model described in Chapter 2, the pipeline is modelled as a beam of flexural stiffness EI Nm^2, which is compressed by an axial force P N. Such a beam is shown schematically in figure 3.1. The beam is assumed to have an initial sinusoidal imperfection of amplitude V_0 m and wavelength L m, and is assumed to retain its sinusoidal shape as it deflects. In consequence, the distribution of the vertical load W N/m along the beam, is assumed to be sinusoidal.

The soil is assumed to have a bilinear response, as shown in figure 2.11; i.e. the soil-response is linear for small displacements, less than the proportional limit V_1, and has a constant value W_0, for displacements greater than the proportional limit, such that:

$$W_1 = \frac{W_0}{V_1}\Delta V \qquad \text{for } \Delta V \leq V_1 \qquad (3.1)$$

$$W_1 = W_0 \qquad \text{for } \Delta V > V_1$$

The vertical load at the peak of the imperfection is denoted by W_1. From equation (2.34), the buckling load P can be expressed as:

$$P = \frac{W_1}{V}\left(\frac{L/2}{\pi}\right)^2 + EI\left(\frac{V - V_0}{V}\right)\left(\frac{\pi}{L/2}\right)^2 \qquad (3.2)$$

The first term of this equation is due to the "arch" effect, while the second term is due to bending.

Tvergaard and Needleman (1981) demonstrated that buckling can be assumed to occur at the minimum peak value of the buckling load P, with respect to the deflection V. Such a peak occurs when dP/dV=0. Differentiating equation (3.2) and equating with zero, yields the following expression:

$$W - W'V\left(\frac{L/2}{\pi}\right)^2 = EIV_0\left(\frac{\pi}{L/2}\right)^2 \qquad (3.3)$$

Here, W'=dW/dV. Re-arranging, L/2 can be expressed as:

$$L/2 = \pi\sqrt[4]{\frac{EIV_0}{W - W'V}} \qquad (3.4)$$

For the bilinear soil model, buckling is assumed to occur when the displacement reaches the proportional limit, i.e. $\Delta V \geq V_1$, and thus $W = W_0$ and $W' = 0$. Substituting these values into equation (3.4), yields the following expression for the buckling half-wavelength $L_b / 2$:

$$L_b/2 = \pi\sqrt[4]{\frac{EIV_0}{W_0}} \qquad (3.5)$$

The wavelength L_b is the shortest wavelength at which buckling can occur, and for the bilinear soil model it also corresponds to the minimum peak value of P. Substituting for $L_b/2$ in equation (3.2), yields the following expression for the minimum peak value of P, which is taken as the buckling load P_b:

$$P_b = \sqrt{\frac{EIW_0}{V_0}} \qquad (3.6)$$

We now have expressions for the buckling wavelength L_b and the buckling load P_b, which for the bilinear soil model, are independent of the proportional-limit V_1 and are dependent only on EI, W_0 & V_0. The maximum temperature rise ΔT_b, can be calculated by dividing P_b by $EA\alpha$.

The value of P_b is plotted against the initial displacement V_0, in figure 3.2. According to the figure, a perfectly straight pipe has an infinite buckling load. However as explained by

Kerr (1974), the behaviour of a perfectly straight pipe will be dominated by the linear region of the soil-response, and buckling will occur at the elastic buckling load P_e, as described by the following equation:

$$P_e = 2\sqrt{\frac{EIW_0}{V_l}} \qquad (3.7)$$

where V_l is the proportional-limit of the soil-response. Thus the elastic buckling load P_e, which is shown on the figure, forms an upper limit to the value of P_b.

At this point, it is interesting to compare the results obtained from the simplified buckling model, with those obtained from a numerical Tvergaard and Needleman model. This is done in figure 3.3, which shows the buckling loads plotted against the initial imperfection size. The buckling loads have been calculated from three different models: the simplified buckling model P_b, the numerical, finite-difference version of the Tvergaard and Needleman model P_f, and the modified Tvergaard and Needleman model P_t, described in Chapter 2. The numerical version is a simple, finite-difference model, and is described in more detail in Appendix A.3. Both the modified and numerical versions of the Tvergaard and Needleman analysis, use an exponential soil-response model. (as illustrated in figure 2.11.)

As can be seen, the three sets of results are in close agreement. This demonstrates that the approximations we have made in the simplified buckling model, have a relatively small effect on the accuracy of the analysis. This result is quite surprising, as we would expect that the shape of the soil-response curve had a greater effect on the calculated results.

The reason for this is illustrated in figure 3.5, which shows the two terms of P from equation (3.2), plotted against the deflection V using the bilinear soil model. The first term of P, an arch term is proportional to L^2. The second term, a bending term is inversely proportional to L^2. The sum of the two terms equals P, and is also plotted. The arch term has a peak and dominates P when L is large. The bending term has no peak and dominates P when L is small.

For short wavelengths as shown in (a), the bending term is dominant and the P curve does not have a peak. If the wavelength is increased to the point shown in (b), the two terms

are evenly balanced and the P curve forms a plateau. This is because both terms are hyperbolic, one rising and one falling, and balance each other. This is the shortest wavelength at which a peak occurs and corresponds to the minimum peak value of P. At longer wavelengths as in (c), the arch term dominates and P has a higher peak value; the peak value increases as the wavelength increases.

The effect of a more general soil-response is shown by the dashed line in (d). At this particular wavelength, which is the shortest wavelength at which a peak occurs, both curves rise to the same plateau value. For the bilinear soil model, this wavelength also corresponds to the minimum peak value of P. For the exponential soil model, the minimum peak value occurs at a slightly longer wavelength and has a lower value.

This is illustrated further, in figure 3.4. The peak value of P is plotted against the half-wavelength, for both the bilinear soil model and the exponential soil model. The initial imperfection amplitude $V_0=0.1$ mm.

For both soil models, the shortest half-wavelength at which a peak in P occurs, is $L_b/2=0.401$ m, as calculated by equation (3.5). Both models have the same peak value $P=186$ N, as calculated by equation (3.6). For the bilinear soil model, the shortest half-wavelength also corresponds to the minimum peak value of P; the peak value increases for longer half-wavelengths. For the exponential soil model, the minimum peak value occurs at a slightly longer half-wavelength $L/2=0.505$ m, and has a lower value $P=163$ N. It can be seen that varying the soil-response profile results in a noticeable variation in the buckling load and the buckling wavelength, but the variation is small.

The simplified buckling model can thus be applied to any soil provided that the plateau value of the soil-response curve is known. According to the model, a pipe with initial imperfections will form lobes at the imperfection positions. The lobes grow as the axial load increases, until buckling occurs at the buckling load P_b. The buckling wavelength is equal to L_b.

Note that equations (3.5) and (3.6) for L_b and P_b, are of the same form as equations (2.5) and (2.4) for L_r and P_r, from the rigid-base model. For a given imperfection size $H_0=2V_0$, $P_r=2.8\ P_b$ and $L_r=1.71\ L_b$.

3.3. The Effective Imperfection Amplitude

In the previous theory, the effect of varying the wavelength of an imperfection has been ignored. Tvergaard and Needleman assumed that buckling is most likely to occur when the actual wavelength of an imperfection matches the buckling wavelength, and this is the critical case assumed by their model. In general, the actual imperfection wavelengths are random, and do not match the buckling wavelengths. However, they suggest that the wavelengths should be assumed to match as a "worst case" analysis for design purposes. The effect of variations in the imperfection wavelength can thus be ignored.

There are however instances where it is necessary to determine the buckling load of a particular imperfection, and a possible method is presented here. The method is based on the assumption that buckling will always occur in such a way that the theoretical relationship between the imperfection amplitude and the buckling wavelength is preserved.

From the simplified buckling theory described above, the theoretical relationship between the amplitude of an imperfection V_0, and the buckling wavelength $L_b/2$ can be described by the ratio $z_b = V_0/(L_b/2)$. Equation (3.5) can thus be re-arranged to give the following expression for the ratio z_b:

$$z_b = \frac{1}{\pi}\sqrt[4]{\frac{W_0 V_0^3}{EI}} \qquad (3.8)$$

It is assumed that this theoretical relationship is preserved during buckling.

An arbitrary imperfection of amplitude V_0 and length L/2, is shown schematically in figure 3.6. For simplicity, the profile is assumed to be sinusoidal. The overall amplitude to wavelength ratio $z_0 = V_0/(L/2)$. If a slice is taken through the top of the imperfection as shown on the figure, the section above the slice forms an imperfection of height Δ, length ξ and amplitude to length ratio $z = \Delta/\xi$. If the position of the slice is moved up or down the value of Δ/ξ will vary accordingly. Buckling is assumed to occur at the particular position of the slice so that $\Delta/\xi = z_b$, i.e.:

$$\frac{\Delta}{\xi} = \frac{1}{\pi}\sqrt[4]{\frac{W_0\Delta^3}{EI}} \qquad (3.9)$$

This is illustrated in the figure, where a lobe has formed on a section of the wavelength, as indicated by the dashed line. The effective amplitude of the lobe $V_{eff}=\Delta$, and the half-wavelength $L/2=\xi$. The buckling load P_b can be calculated by substituting the value of V_{eff} into equation (3.6). The maximum temperature rise ΔT_b is calculated by dividing P_b by $EA\alpha$.

3.4. An Example

An example of this method is illustrated in figures 3.7, 3.8 and 3.9. The data is taken from the test pipe used in the experiments. $EI=3.131\ Nm^2$ & $W0=1.1\ N/m$. The initial imperfection is assumed to be of amplitude $V_0=1$ mm, and half-wavelength $L/2=1$ m. The calculated buckling half-wavelength $L_b/2=0.73$ m, which is approximately three quarters of the actual half-wavelength.

The value of Δ/ξ can be plotted versus Δ as in figure 3.7. This corresponds to varying the height of the slice. The value of z_b, as calculated from equation (3.8) and substituting $V_0=\Delta$, is also plotted on the figure. The effective amplitude $V_{eff}=0.37$ mm, is found at the intersection of the two lines, and in this case is approximately one third of the actual amplitude.

A second method for determining the effective amplitude is from the dimensionless plot of V_{eff}/V_0 versus L_0/L_b shown in figure 3.8. According to this figure, if $L/L_b>1$, then the effective amplitude will be smaller than the actual amplitude. Conversely, if $L/L_b<1$, then the effective amplitude is assumed to equal the actual amplitude, i.e. $V_{eff}=V_0$.

For the example shown, the value of L_b corresponding to the imperfection amplitude V_0, can be calculated from equation (3.5) as:

$$L_b/2 = \pi\ \sqrt[4]{(3.131 * 0.001 / 1.1)} = 0.726\ m$$

and:

$$L/L_b = 1 / 0.73 = 1.38$$

From the graph $V_{eff}/V_0 = 0.37$ and:

$$V_{eff} = V_0 * 0.37 = 0.37\ mm$$

The buckling load P_b is calculated by substituting $V_0=V_{eff}$ into equation (3.6), thus:

$$P_b = \sqrt{(3.131 * 1.1 / 0.001)} = 97 \text{ N}$$

The maximum temperature rise ΔT_b can be calculated as:

$$\Delta T_b = 97 / (650000 * 9.4 \times 10^{-6}) = 16 \ (^oC)$$

where ΔT_b is measured from the temperature where there is zero axial stress on the pipe. By comparison, the buckling load, as calculated from the actual amplitude, is 59 N.

The data can also be presented as a dimensionless Palmer plot, as discussed in Chapter 2. This is demonstrated in figure 3.9, which shows the dimensionless vertical load Φ_W, plotted versus the dimensionless wavelength Φ_L. Note, that the simplified buckling model corresponds to a single data point at the position $\Phi_W=0.5$ & $\Phi_L= \pi$.

From the previous example, the dimensionless wavelength Φ_L, can be calculated as:

$$\Phi_L = \sqrt{(97/3.131)} = 5.55$$

Similarly, the dimensionless vertical load Φ_W, can be calculated as:

$$\Phi_W, = (1.1*3.131)/(0.002*97^2) = 0.183$$

These values are shown on the figure. Note, that if the value of P is unknown, it cannot be calculated directly from the graph, but must be determined by iteration.

3.5. Determining the Initial Imperfection Amplitude

A particular shortcoming of the experimental apparatus is that it was not possible to measure the amplitude of the initial imperfections on the test pipe. It is thus necessary to estimate the approximate amplitude, from the experimental data.

One possible way of doing this is by means of the Southwell plot, which is a plot of $\Delta V/P$ versus ΔV. If the soil has a linear response, the Southwell plot will be a straight line of slope $1/P_e$ and with an x intercept at $-V_0$. The values of ΔV and P for the test pipe, can be measured so that provided the soil-response is linear, it is a simple matter to determine the size of the initial imperfection.

Unfortunately, the response of the test soil is non linear, and the Southwell plot can not be used directly to determine V_0. This is illustrated in figures 3.10 and 3.11, which show the numerical data from the finite-difference model discussed in Section 3.2. The soil-response is assumed to be exponential.

Figure 3.10 is a plot of the axial load P, versus the vertical displacement ΔV. Buckling occurs at the point where the curves stop abruptly. The magnitude of the buckling load decreases and the buckling displacement increases, as the imperfection size increases.

The same data is re-plotted in figure 3.11 as a Southwell plot. At very small displacements the lines are curved, possibly due to truncation error. At large displacements the lines are reasonably straight. However, the slope of each line corresponds to a buckling load which is considerably higher than the actual buckling load. The x-intercept points are also inaccurate; being considerably smaller in magnitude than the values of V_0.

An alternative method of estimating the imperfection amplitude, and the method which has been used for these experiments, is to compare the experimental data with the numerical data from figures 3.10 and 3.11 above. The experimental data can be plotted over the top of the numerical data, and the imperfection amplitude estimated by comparing the lines. The application of this method is demonstrated in Chapter 5.

3.6. Figures

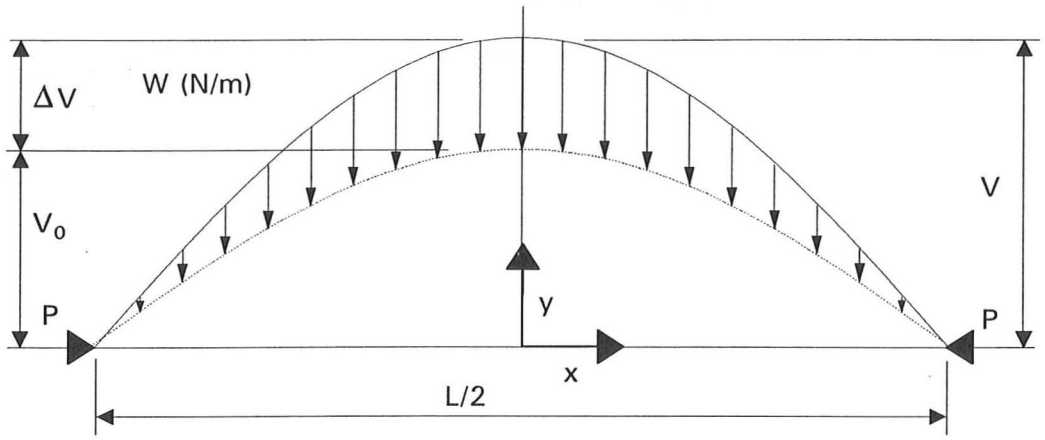


Figure 3.1. A schematic diagram of the simplified buckling model, showing an imperfection of length L/2 and initial amplitude V_0. The vertical load W has a sinusoidal distribution along the beam.

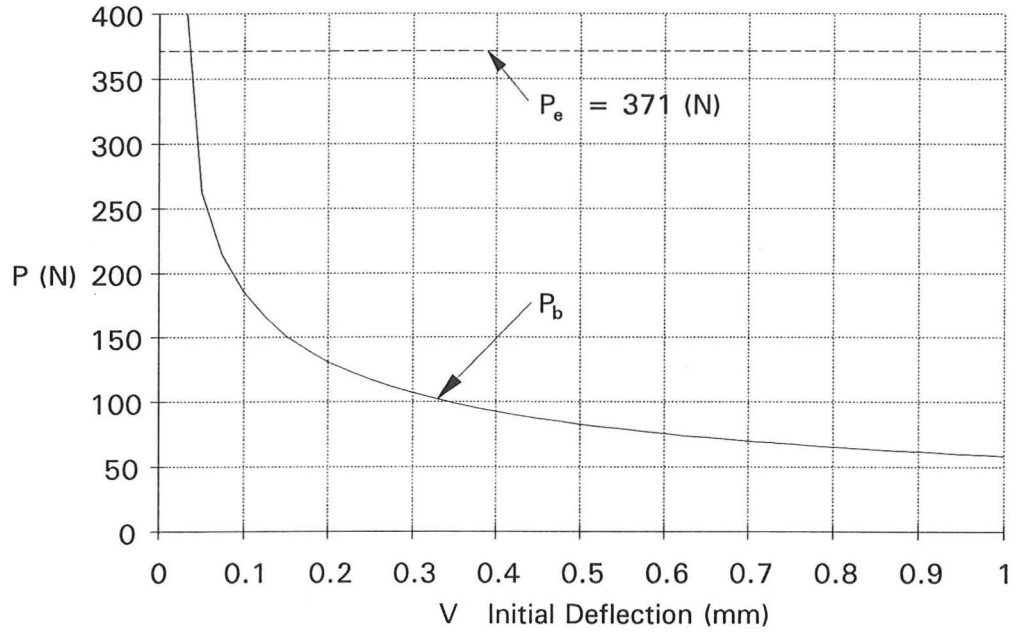


Figure 3.2. The buckling load according to the simplified buckling model P_b,and the elastic base model P_e, are plotted versus the initial deflection amplitude V_0. EI=3.131 Nm^2 & W_0=1.1 N/m.

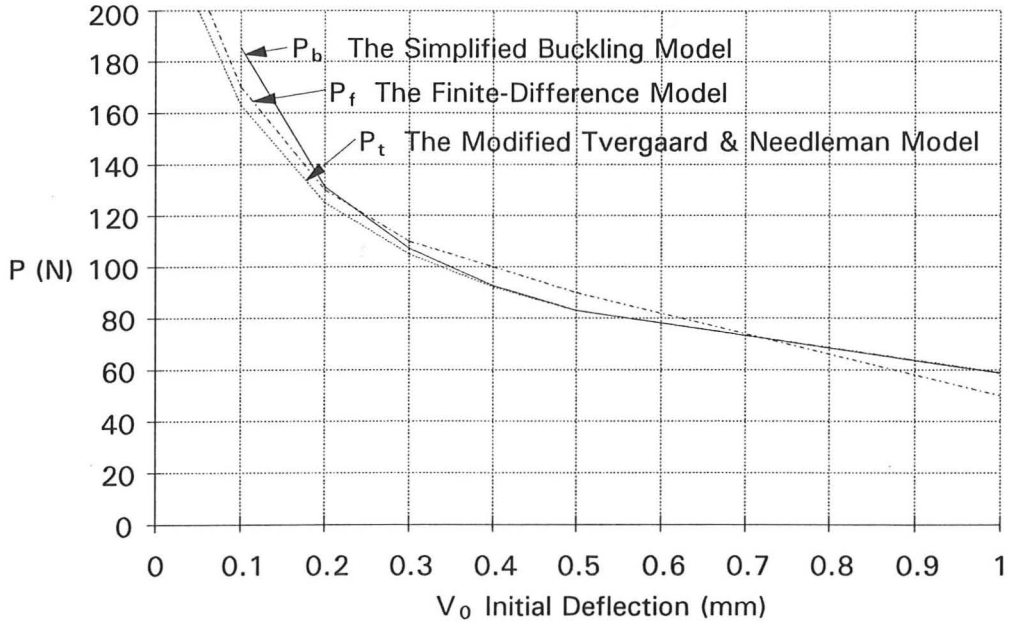


Figure 3.3. A comparison of the buckling loads from three different models; the simplified buckling model P_b, the modified Tvergaard & Needleman model from Chapter 2 P_t, and the finite difference model P_f, are plotted together versus V_0. EI=3.131 Nm^2, W_0=1.1 N/m & V_1=0.1 mm.

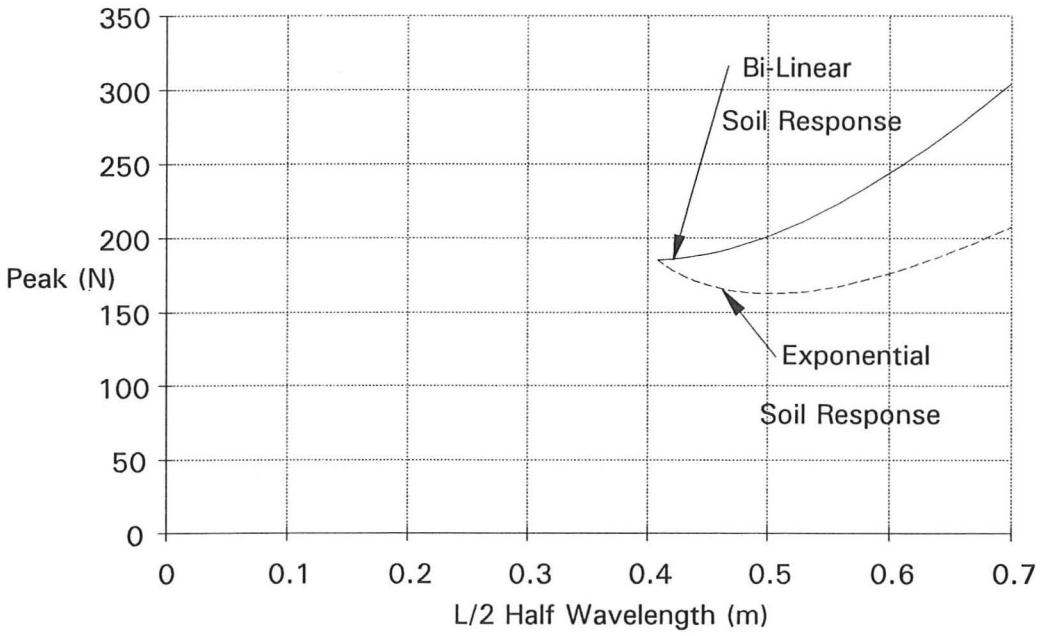


Figure 3.4. The variation of the peak load with the half-wavelength, for the bilinear and exponential soil response models. EI=3.131 Nm^2, W_0=1.1 N/m, V_0=0.1 mm & V_1=0.1 mm.

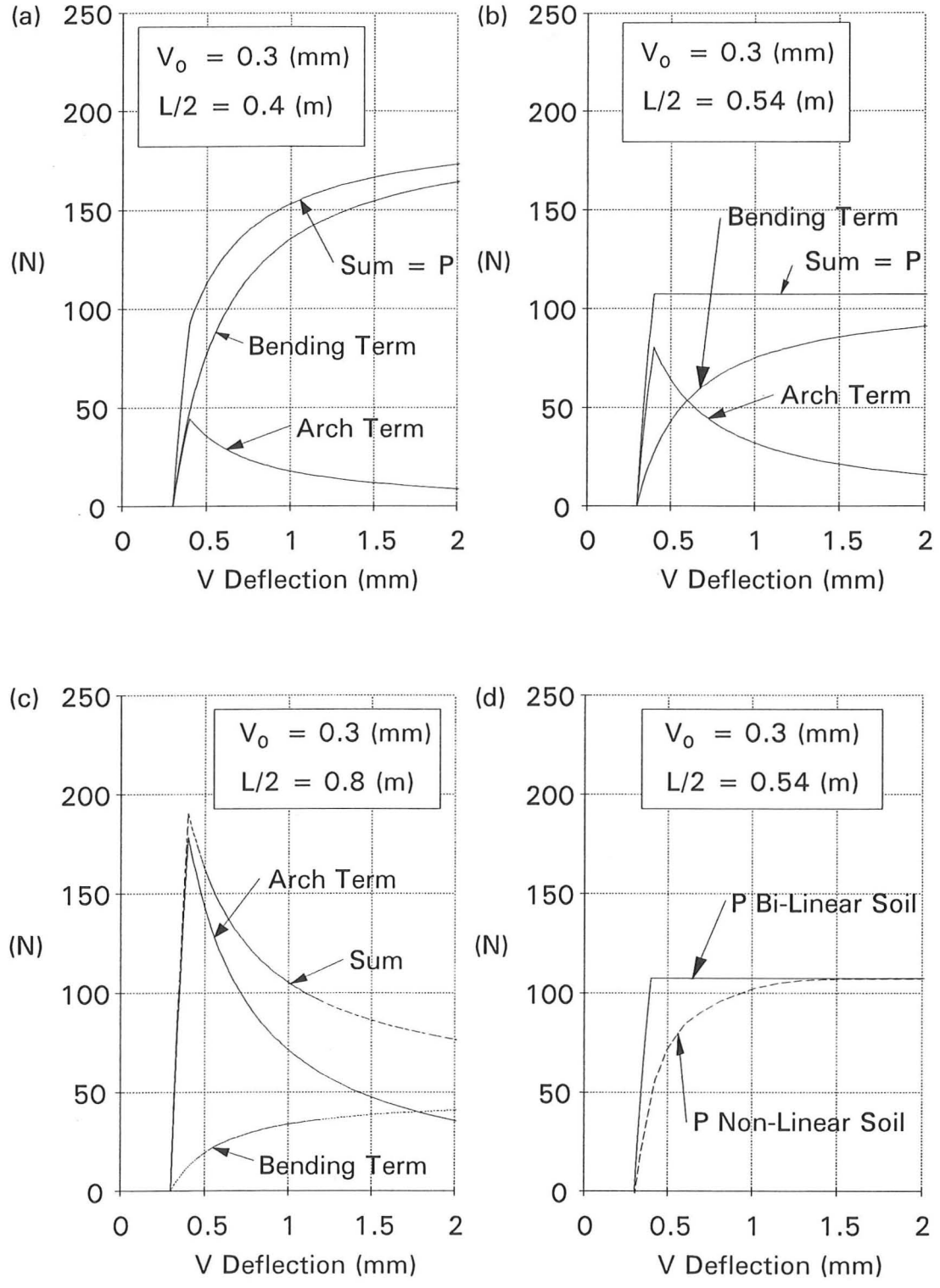


Figure 3.5. The effect of wavelength on the arch and bending terms for the bilinear soil model. (a) L/2=0.4 m, (b) L/2=0.54 m, (c) L/2=0.8 m and (d) The effect of a non-linear soil response, L/2=0.54 m. EI=3.131 Nm^2, W_0=1.1 N/m & V_1=0.1 mm.

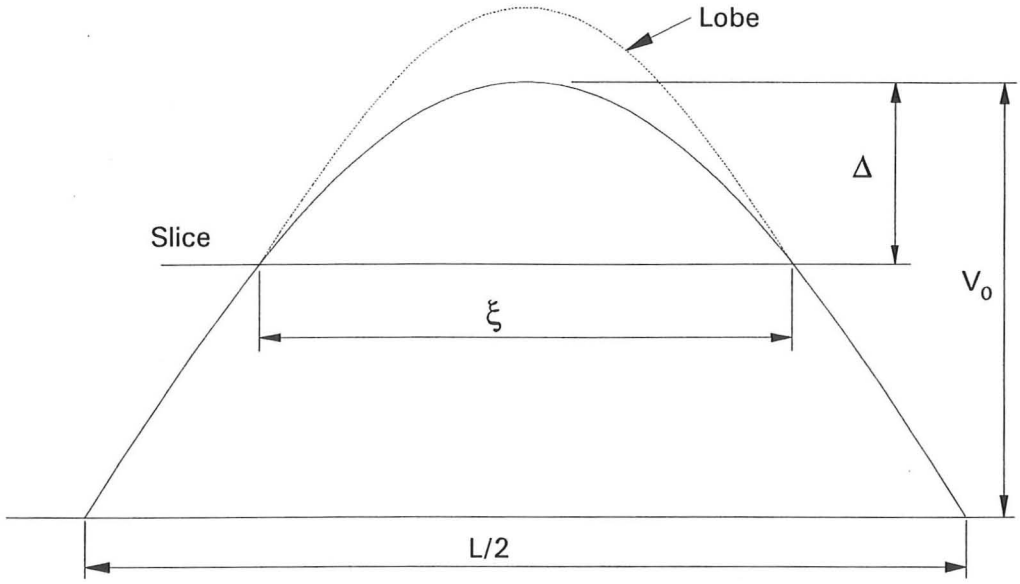


Figure 3.6. A schematic diagram of an arbitrary sinusoidal imperfection of length L/2 and amplitude V_0. The figure shows a slice taken from the imperfection of height Δ and length ξ. The buckle profile is shown as a dotted line.

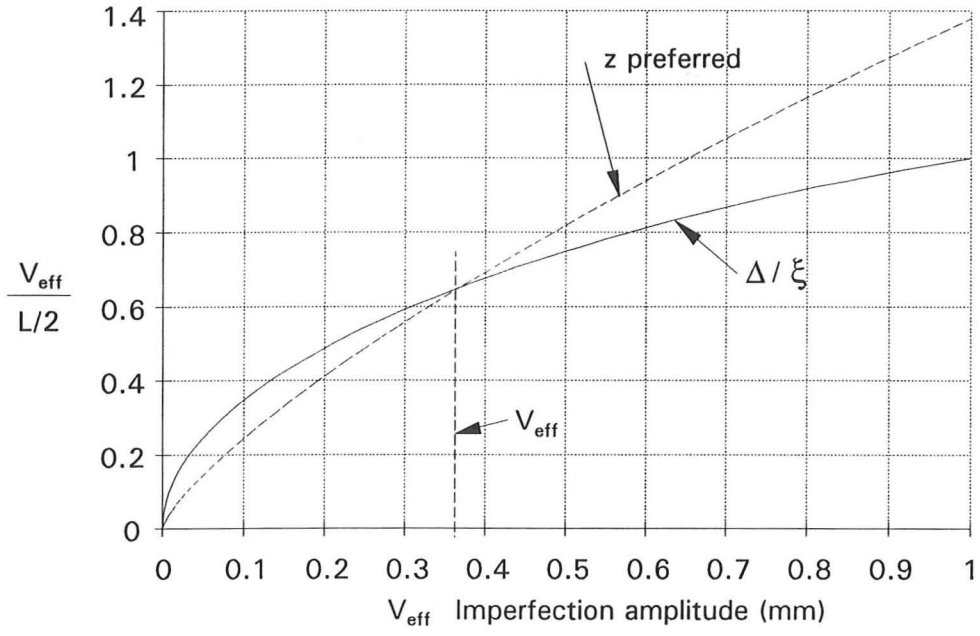


Figure 3.7. A method for determining the effective amplitude V_{eff}. The ratio Δ / ξ for an arbitrary sinusoidal imperfection is plotted versus V_{eff}, along with the preferred amplitude to half wavelength ratio z. The effective amplitude $V_{eff} \approx 0.37$ mm, is found at the intersection of the two lines. $V_0=1$ mm, $L_0/2=1$ m, EI=3.131 Nm^2 & $W_0=1.1$ N/m.

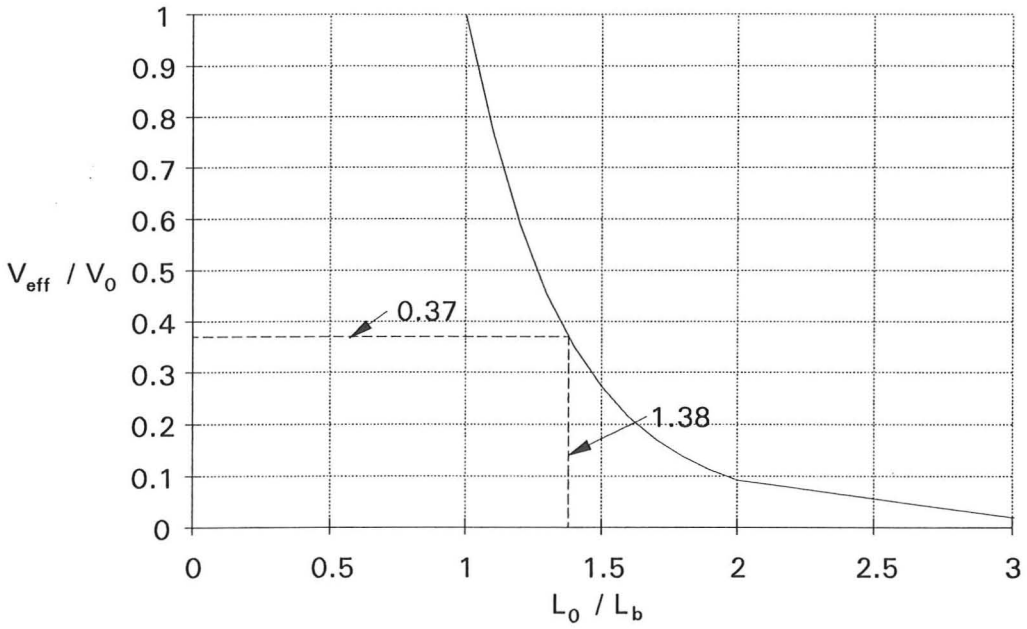


Figure 3.8. A dimensionless plot of the effective amplitude versus the wavelength, where V_0 & L_0 are the imperfection amplitude and wavelength, L_b is the buckling wavelength corresponding to V_0, and V_{eff} is the effective amplitude.

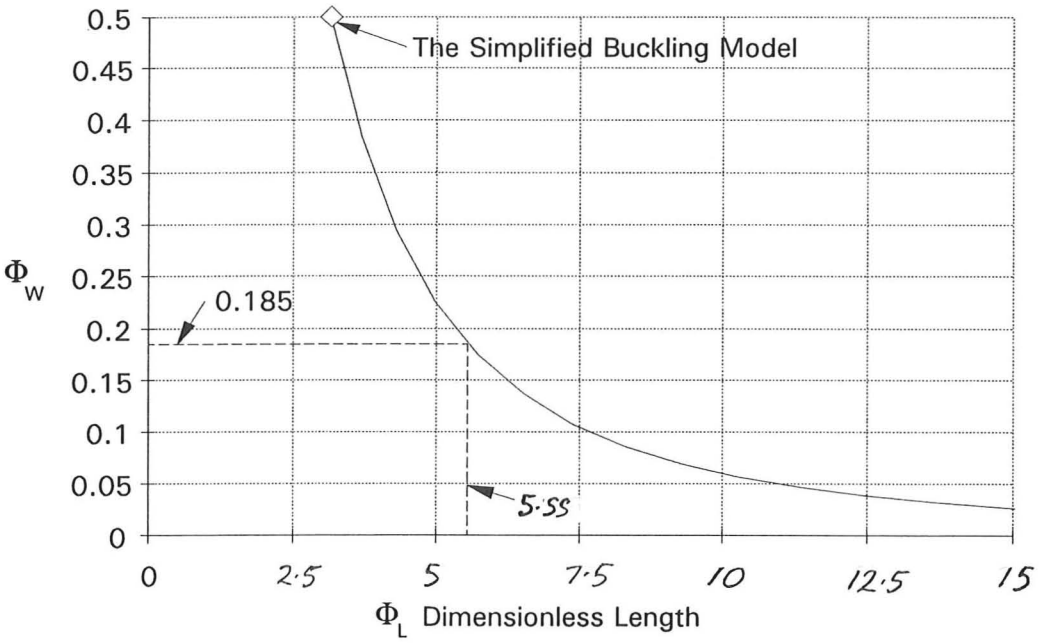


Figure 3.9. A dimensionless Palmer plot of the effective amplitude data. The dimensionless vertical force $\Phi_W = WEI/(2VP^2)$, is plotted versus the dimensionless wavelength $\Phi_L = (L\sqrt{(P/EI)})/2$. The simplified buckling model corresponds to a single data point at the position $\Phi_W = 0.5$ & $\Phi_L = \pi$.

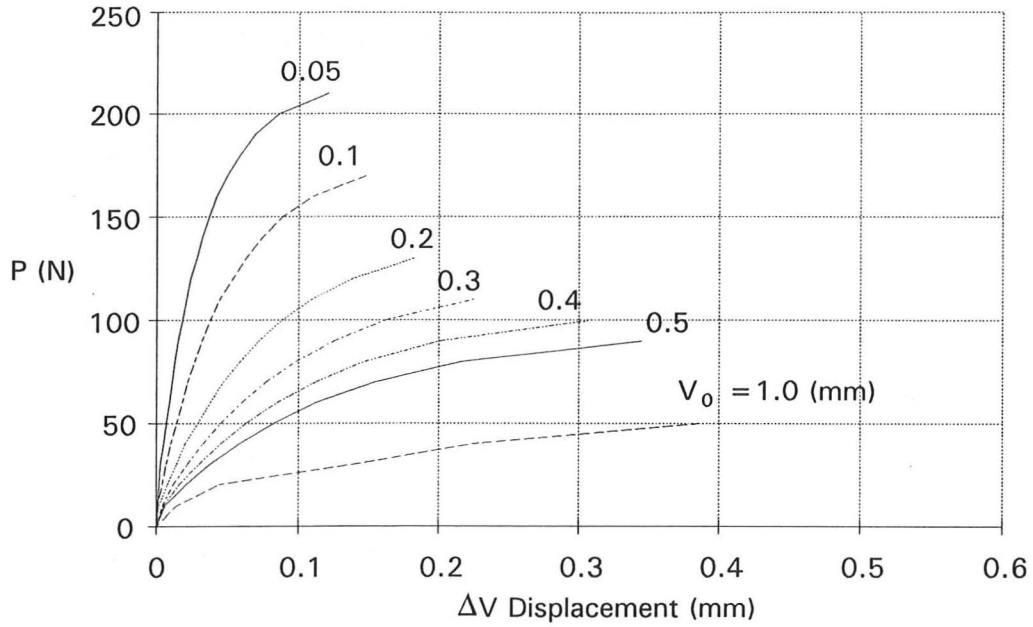


Figure 3.10. The displacement data from the finite difference model. The load P is plotted versus the displacement ΔV, with an assumed exponential soil response. V_0=0.05 to 1.0 mm, EI=3.131 Nm^2, W_0=1.1 N/m & V_l=0.1 mm.

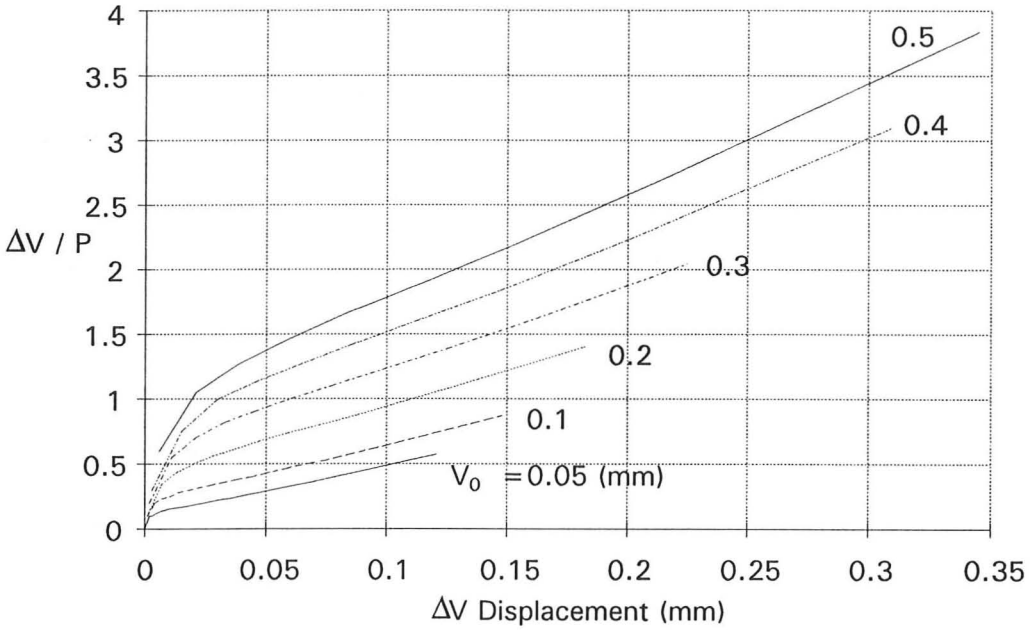


Figure 3.11. A Southwell plot of the data from the finite difference model, using an exponential soil response model. V_0=0.05 to 1.0 mm, EI=3.131 Nm^2 & V_l=0.1 mm.

4. Experimental Apparatus

4.1. Introduction

This chapter describes the experimental apparatus which was used to conduct a series of experiments on various aspects of upheaval buckling. The apparatus includes a model pipeline which was used for the buckling tests, a movable bar which was used to measure the forces exerted on a pipe by the soil, and an apparatus for measuring the reference data for the model pipe. These are described below.

4.2. Overview of the Apparatus

The main experimental apparatus consists of a 5 m length of 6 mm diameter pipe, which is buried in a layer of plastic soil. The pipe and the soil both lie inside an aluminium channel. An axial load can be applied to the pipe either by compressing the pipe from one end with a simple screw mechanism, or by applying internal hydraulic pressure to the pipe while restraining the ends. A lateral load can be applied by means of a string which is attached to the pipe; the string passes over a pulley and is attached at the other end to a hanging weight. The axial load can be cycled by cycling the hydraulic pressure in the pipe. The pressure cycling is controlled by a computer and an electrical solenoid valve. The axial load in the pipe can be measured by a load cell which is attached to one end of the pipe. The hydraulic pressure is measured with a pressure transducer.

The position of the pipe is measured by applying a 1 kHz electrical signal to the pipe and measuring the change in the electrical field. The electrical field is measured by four capacitive sensors attached to the under side of a travelling trolley. The trolley is controlled by the computer and is programmed to scan along the pipe, stopping at approximately 100 mm intervals to take readings, and to calculate the horizontal and vertical position of the pipe. Each complete scan of the pipe takes approximately 5 minutes. The measuring system is capable of measuring the position of the pipe to within $\pm$ 0.5 mm. Alternatively, the position data can be used to measure the pipe movement to within $\pm$ 0.05 mm, provided that the surface of the soil remains undisturbed.

An end view of the trolley is shown in figure 4.1, a view of the under side is shown in figure 4.2, and a photograph of the trolley is shown in figure 4.3. A schematic diagram of the main apparatus is shown in figure 4.4.

A separate apparatus was used to measure the forces exerted on the pipe by the soil, and it is shown schematically in figure 4.6. The apparatus consists of a 300 mm length of 6 mm diameter solid bar, which is attached by its centre to a two axis load cell. The bar and the load cell are both mounted on the side of a 600 mm length of channel, which is filled with soil. The bar and the load cell together, can be moved horizontally and vertically by turning the two wheels shown in the figure. The position of the bar is measured by the two position transducers fitted to the mounting. The horizontal and vertical forces on the bar and the position of the bar, are recorded by the computer.

The same apparatus can be converted and used to record the reference data for the position measuring system. The apparatus is converted by removing the load cell and the 300 mm bar on the mounting, and substituting a 1 m long bar which is mounted at both ends. The bar can be moved horizontally and vertically through the soil inside the channel by turning the two pairs of wheels. The position of the ends of the bar is measured by the two pairs of transducers. The sensor-trolley is positioned on top of the section of channel. To record the reference data, the bar is carefully positioned at each of the grid points shown in figure 4.7, and a set of data readings are taken. The reference grid consists of 11 vertical grid lines, $x = 0$ to 10, and 6 horizontal grid lines, $y = 0$ to 5. The reference data consists of a set of discrete data points which are interpolated by the position measuring system.

Some details of the apparatus are listed in appendix A1.

4.3. Details of the Apparatus

4.3.1. The Channel Section

The channel section is constructed from two 3 m lengths of aluminium "I" section beam which are bolted together in the middle. They are mounted on their side with fish plates on the laboratory window sill. The shape of the channel (⊢┤), is convenient for the experiments

because it acts as a track for the sensor-trolley, and also holds the soil in place. The channel is also used to mount various items of equipment.

The out of straightness of the channel was measured and was approximately $\pm$ 0.5 mm in the vertical direction, and $\pm$ 1 mm in the horizontal direction.

4.3.2. The Test Pipe

The test pipe is constructed from stainless steel tubing of length 5 m, 6.37 mm OD. and wall thickness 0.16 mm. A small diameter test pipe was chosen because the maximum length of the pipe was restricted by the width of the laboratory and a high L/D ratio, that is the ratio of the pipe length to diameter, was desired. A high L/D ratio in the test pipe has the following advantages:

(i) It allows multiple buckles to form independently of one another, and at their preferred natural wavelengths.

(ii) It allows axial friction to be mobilised.

(iii) The central section of the pipe is less affected by the conditions at the end of the pipe.

(iv) Small diameter pipes are easy to handle, although great care must be taken to avoid damage to the pipe during handling.

Conversely, the pipe must be kept reasonably short so that the axial load can be applied from one end of the pipe. If the pipe is too long, the axial friction effect prevents the axial load being transferred evenly along the length of the test pipe. Thus the choice of pipe length is a compromise between the two conflicting objectives. The 5 m length of the test pipe corresponds to an L/D ratio of 830. In real pipelines the L/D ratio is infinitely large.

The test pipe was straightened before any tests were performed so that any initial crookedness in the pipe would not affect the tests. This was achieved by stretching the pipe until it had deformed plastically, and was permanently extended by 3 to 5 mm. To do this, one end of the pipe was clamped to the channel and the other end was extended by means of a simple screw device. The calculated load required to deform the pipe plastically is

approximately 700 N, corresponding to a yield strength of 300 MPa. The calculated strength of the glued joint is approximately 2,000 N.

4.3.3. The Pipe End-Mountings

The pipe end-mountings are illustrated schematically in figure 4.5. The figure shows the mounting block at the North end of the apparatus. The mounting at the South end is similar but is not equipped with either a load-cell or an axial load-screw. The pipe is glued into mounting blocks at both ends, and these are in turn bolted to the channel section. The base of the mounting blocks is slotted so that the bolts can be loosened and allow the pipe to be positioned longitudinally. The guide blocks are machined to fit snugly over the pipe and are designed to prevent the end section of the pipe from buckling. The maximum compressive load which can be applied to the pipe, is limited to approximately 250 N by the buckling strength of the exposed end section of the pipe.

An end load is applied to one end of the pipe by hand turning the axial load-screw. The load-screw turns in a threaded plate, which is fixed to the channel, and pushes the load-plate against the end-mounting block, thus compressing the pipe.

An axial load can also be applied by pressurising the pipe with hydraulic oil, while restraining the ends. The advantage of this method is that the axial load distribution is comparatively uniform. It is also a convenient method for applying a cyclic load because the pressure, and hence the axial load, can be controlled by the computer. Unfortunately the maximum load is limited to about 70 N by the maximum operating pressure of the hydraulic system. The effective load can be increased for cyclic tests by applying an end load in addition to the cyclic load. The end load is kept constant while the pressure is cycled. This method was found to be satisfactory, however the pipe behaviour is affected by both the peak cyclic load and the amplitude of the cycle.

An alternative method for applying an axial load would be by heating the pipe and utilising the restrained thermal expansion. Each degree of temperature rise corresponds to 6 N of axial load. This method is capable of applying large axial loads and produces a uniform axial

load distribution throughout the pipe. It is however slow and cumbersome, especially for cyclic loading, and was considered impractical for these tests.

The high pressure hydraulic oil is supplied by an electric pump fitted with a pressure regulator and a solenoid on / off valve. The pressure regulator is set manually, the solenoid valve is controlled by the computer. The operating pressure of the system is limited to 1,000 psi. A small hand pump is installed in parallel to the electric pump. A flow restricting valve was fitted to the solenoid outlet to prevent a sudden surge of pressure as the solenoid valve opens and closes.

The axial load-cell consists of two sets of strain gauges, which are mounted on the circumference of both the test pipe and the dummy pipe. These can be seen in the figure. The dummy pipe is an additional length of pressurised pipe, which is identical to the test pipe and mounted directly above it. The strain gauges are connected in a half bridge so that the dummy pipe corrects for the effects of temperature and pressure. The load cell output was calibrated by loading the pipe in tension with a calibrated strain gauge. The calibration is used by the computer to convert the load cell output to load in Newtons.

The hydraulic fitting may be removed from the mounting block so that lengths of solder can be fed down the inside of the pipe in order to increase its self weight. (This feature was not used during the experiments) The weight of the empty pipe is approximately 0.23 N/m, the oil in the pipe is 0.25 N/m and of a single strand of solder is 0.09 N/m. A pipe filled with oil and with no solder weighs 0.47 N/m. A pipe filled with oil and with 6 strands of solder weighs 0.92 N/m, approximately double the weight of a pipe with no solder. The bleed screw on the top of the mounting block allows trapped air to be bled out of the pipeline. If air is trapped in the pipeline it can be dangerous at high pressure.

4.3.4. The Pipe and Soil Levelling Tools

For each experiment, the pipe is re-laid as straight as possible and the soil is re-levelled. The pipe is first tensioned with a load of approximately 100 N by means of a calibrated spring balance. The pipe is straightened horizontally by visually checking it with a string line. It is then straightened vertically by running the pipe-levelling tool, shown in figure

4.8.a, along the channel. The tool has a foot which presses down on the pipe and forces it into the soil. After two passes the pipe can be regarded as being level with the channel section flanges.

The soil is levelled over the top of the pipe in a similar manner. The soil-levelling tool shown in figure 4.8.b, has an adjustable blade which sits at 60 degrees to the channel. The tool is run along the channel and it scrapes the soil over and levels it as it passes. The shape of the blade cuts a trench on one side of the channel, and leaves a mound on the other. The purpose of this feature is to increase the amount of soil which is moved at each pass and to make the levelling process less sensitive to the amount of soil in the channel.

As both the laying of the pipe and the re-levelling of the soil rely on the channel section flanges as a datum level, both are affected by any crookedness of the channel. The pipe straightness is also affected by any crookedness of the end-mounting blocks.

4.3.5. The Soil Material

The soil material used for most of the tests was composed of polycarbonate granules of approximately 3.5 mm diameter. The granules were the smallest size available, but are very large in comparison with the test pipe diameter; being about half the pipe diameter. If the model was scaled by physical size, the granules would represent a real soil composed of large rocks. In order to model a real soil composed of fine sand, a model soil of extremely fine granules would be required. This was not possible. Several attempts were made to reduce the size of the granules by crushing and grinding but these were unsuccessful because of the extreme toughness of the polycarbonate granules.

Polycarbonate granules were used for the soil because of their low electrical permittivity. The electrical permittivity of the soil is important for these experiments because it affects the accuracy of the position measuring system. It should be as low as possible. If the permittivity is too high, as with a soil composed of sand granules, the measuring system will in effect measure the position of the soil surface rather than the position of the pipe. Some values of the relative permittivity are given as follows: Vacuum 1.0, air 1.0, polypropylene 2.15,

polystyrene 2.55, sand 8 and polycarbonate 3.0. (Note, that other materials have a lower permittivity than polycarbonate, but polycarbonate was chosen because of availability.)

Even with the polycarbonate soil, any variation in the soil depth has a significant effect on the measured position of the pipe. Each 1 mm change in the soil level produces a 1 mm change in the measured position of the pipe. Figure 4.9 shows the apparent vertical movement of the pipe due to re-levelling of the soil. The pipe appears to move by $\pm$ 0.5 mm after each re-levelling. This is due to variations in the soil level of approximately $\pm$ 0.5 mm between re-levelling. Note that two scans were made between each re-levelling and that the apparent movement between the two scans is only $\pm$ 0.02 mm. This demonstrates the repeatability of the system, provided that the level of the soil is not disturbed between scans.

4.3.6. The Position-Sensors and the Sensor-Trolley

The position-sensors provide the raw data for the position measuring system and must therefore be as accurate as possible. This has been achieved in three ways:

(i) Reducing the effects of electrical interference as much as possible.

(ii) Ensuring that the trolley always returns to the same positions for each scan.

(iii) Using a dummy reference sensor to compensate for fluctuations in the high frequency signal voltage and frequency, and fluctuations in the power supply voltage.

A high frequency electrical signal of 1 kHz is generated by a signal generator and amplified to approximately 16 V, before being applied to the pipe. The sensors are constructed from solid brass spheres of 10 mm diameter. They are mounted at 30 mm spacing in a line along a Perspex block. The block is mounted under the sensor-trolley, as shown in figures 4.1 and 4.2, so that the sensors are in a line perpendicular to the channel and are situated halfway between two of the wheels. The AC signal from each sensor is carried by a short coaxial cable to one of four individually shielded circuit boxes. The circuit boxes are mounted as closely as possible to the sensors to reduce electrical interference. Separate circuit boxes are used for each sensor so that the outputs do not affect each other.

Each circuit box has a high resistance input amplifier, with unity gain, to minimise the current drawn from the sensors. The signal is amplified, with a gain of ten, before being

converted from AC to DC by a digital converter. The DC output signal of approximately 1.5 V is filtered and carried by overhead wire to the logger. The data is logged and recorded by the computer.

The sensor system includes a fifth dummy sensor. This is a complete, separate unit which consists of a short test pipe, a sensor and a circuit box, which are mounted together in a shielded box and are located close to the power supply. The dummy sensor and the dummy pipe are fixed relative to each other. The output from the four position-sensors is divided by the dummy sensor output, in order to standardise the outputs and thus compensate for variations in the voltage etc. In practice, a significant variation in the signal voltage, the signal frequency or the supply voltage produces almost no change in the standardised outputs. The direct sensor output is measured in volts and the standardised sensor output is dimensionless.

The sensor-trolley is constructed from 3 mm aluminium plate. Both the trolley and the channel are earthed to help shield the sensors from electrical interference. The trolley end plates are shown dotted in figure 4.1. They cover the end of the trolley down to just above the level of the flanges. The trolley design has three wheels for positive location. There are two wheels with v-grooves on one side of the trolley and a single, cylindrical wheel supports the other side of the trolley. The v-grooves sit on the channel flange and provide positive lateral positioning of the trolley. One of the v-groove wheels is connected directly to a stepper motor and acts as the driving wheel. The stepper motor provides accurate lengthwise positioning of the trolley.

The output cables are supported up to the overhead wire by the mast. The cables are looped on to Teflon sliders that slide along the support cable behind the trolley. Lead ballast weights were added to the trolley to improve its stability. A disadvantage of the three wheeled design is poor stability.

The stepper motor was itself a very strong source of high frequency electrical interference and could not be adequately shielded. It was therefore necessary to turn it off before each set of data readings are taken. To prevent the trolley slipping while the stepper motor was turned off, a felt pad has been fitted on the inside of each of the wheels to act as a brake.

4.3.7. The Position-Measuring System

In principle, given the outputs from the four sensors, it should be a relatively simple procedure to calculate the position of the pipe. In practice however, this is not the case, and a considerable amount of trial and error was involved to develop a practical system. The system finally evolved works by storing a set of reference data for a known set of grid positions, and comparing this with the data from the position-sensors in order to calculate the pipe position.

The reference data, which we refer to as S_{ref}, is stored for each of the grid points shown in figure 4.7. The grid points are at the intersections of the horizontal and vertical grid lines. There are eleven vertical grid lines, x = 0 to 10, six horizontal grid lines, y = 0 to 5 and 66 grid points. The grid lines correspond to increments of 10 mm in the horizontal direction and 5 mm in the vertical direction. The grid positions are used as the co-ordinate system for the measuring system and the final positions are converted to mm co-ordinates.

Figure 4.10 shows the reference data S_{ref}, from sensor number two. The sensor data is plotted versus the horizontal or x position of the pipe, and forms a series of bell shaped curves corresponding to the vertical or y position. The peak of each curve occurs where the pipe is directly under the sensor, at x=3 for sensor two. The height of the curve increases as the vertical position increases, the maximum being at y=0. There is similar data stored for sensors one, three, and four. The data points are shown joined with straight lines. The data is also stored as a series of polynomials so that the straight lines in figure 4.10 can be replaced with a series of smooth curves.

The system also uses the sensor ratio data which is referred to as SS_{ref}. The sensor ratio is the ratio of the largest sensor reading to the second largest sensor reading. The ratio of sensor two to sensor three, S2/S3, is shown in figure 4.11. In this case, the data polynomials have been used to produce the smooth curves shown in the figure. There is a similar set of curves for each pair of adjoining sensors, i.e. for S1/S2, S2/S1, S2/S3, S3/S2, S3/S4 & S4/S3.

To calculate the pipe position, the system records the four position-sensor readings and ranks them in size. The largest reading S_{data}, is compared with the reference data S_{ref}, in order to interpolate the vertical or y position of the pipe. The ratio of the largest reading to the

second largest reading SS_{data}, is compared with the reference data ratio SS_{ref}, in order to interpolate the horizontal or x position of the pipe. In both cases the interpolation uses a simple Newton Raphson form of iterative solution. The algorithm is described in appendix A1.

4.4. Calibration of the Apparatus

The following items of equipment were calibrated in the standard manner.

(i) The axial load cell

(ii) The two axis, soil force load cell

(iii) The pressure transducer

The calibration data is included in the computer program, and the data outputs are automatically converted to the correct units.

The accuracy of the position measuring system is demonstrated in figures 4.12 and 4.13. The tests were taken with two different depths of soil cover, 6 & 12 mm. From the horizontal tests in figure 4.12 it can be seen that the depth of soil cover has a minimal effect on the measured position. More importantly, the relationship between the measured position and the actual position is linear and has a slope of approximately one. The difference between the measured and the actual positions, is due to the arbitrary location of the reference data scale. To simplify the algorithm, the scale has been shifted so that the midpoint of the reference data occurs at exactly x=5. The small amount of scatter is possibly because the soil was re-levelled before each reading was taken.

The vertical tests in figure 4.13 show a more varied relationship between the actual and measured positions. The slope of the line varies with the vertical position and with the depth of soil. The relationship is however approximately linear, and has an average slope of approximately one.

The measuring system is capable of measuring the position of the pipe to within $\pm$ 0.5 mm, and the movement of the pipe to within $\pm$ 0.05 mm.

4.5. Figures

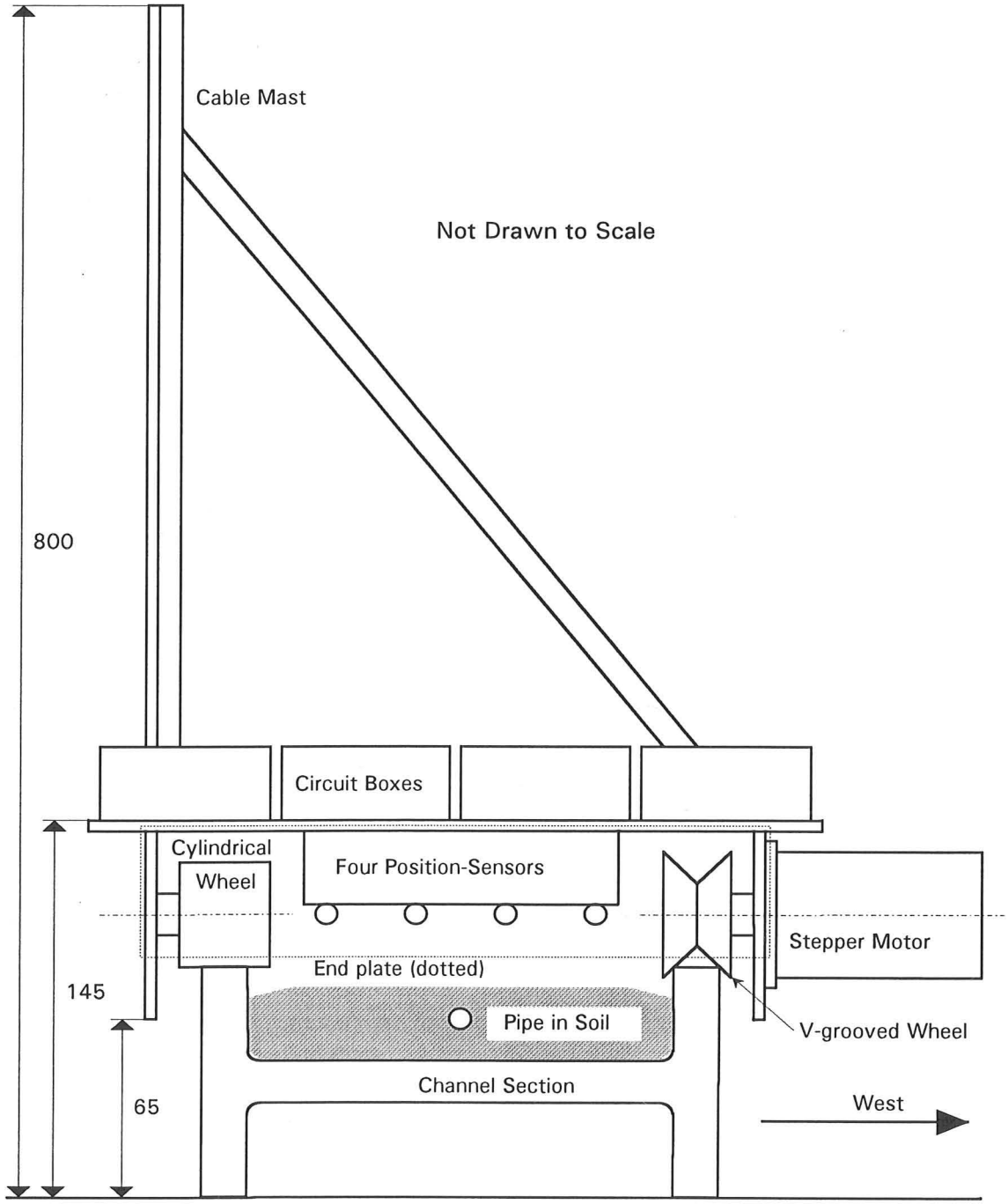


Figure 4.1. An end elevation of the sensor-trolley, shown in position on the channel. The position of the end plate is shown as a dotted line for clarity. Note the positions of the four position-sensors, the cylindrical wheel and the v-grooved wheels. Some leading dimensions are shown in mm. The channel section is 149 mm wide, 79 mm high and the web and flanges are 9.5 mm thick. The test pipe is 6.4 mm outer diameter, and 0.17 mm wall thickness.

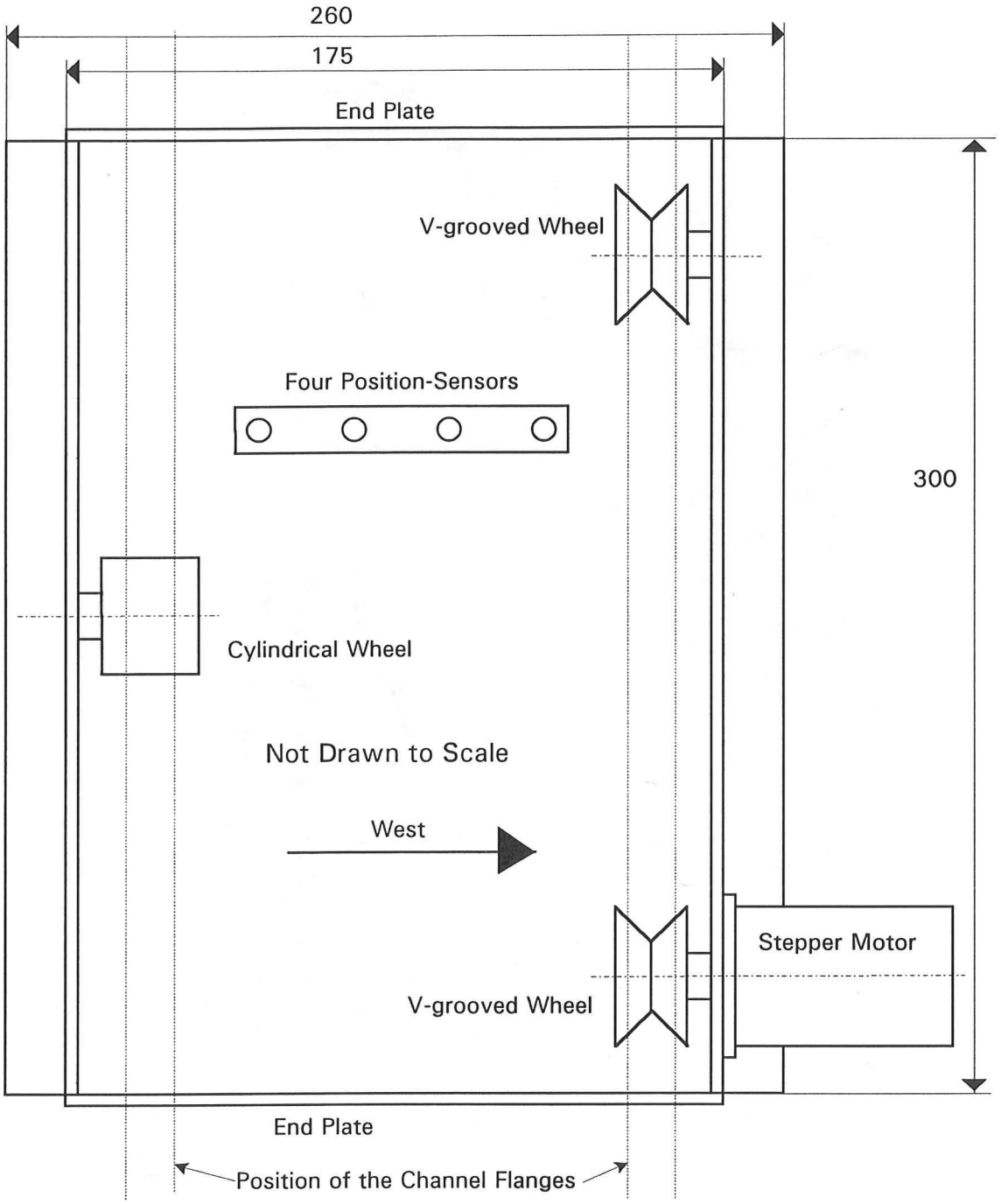


Figure 4.2. A view of the under side of the sensor-trolley, showing the location of the four position-sensors and the three wheels. Refer also to the previous figure. The trolley is located by the two v-grooved wheels on the right hand side, which sit on the channel flange. The position of the channel flanges is shown by the dotted lines. The figure is not drawn to scale. Some leading dimensions are shown in mm.

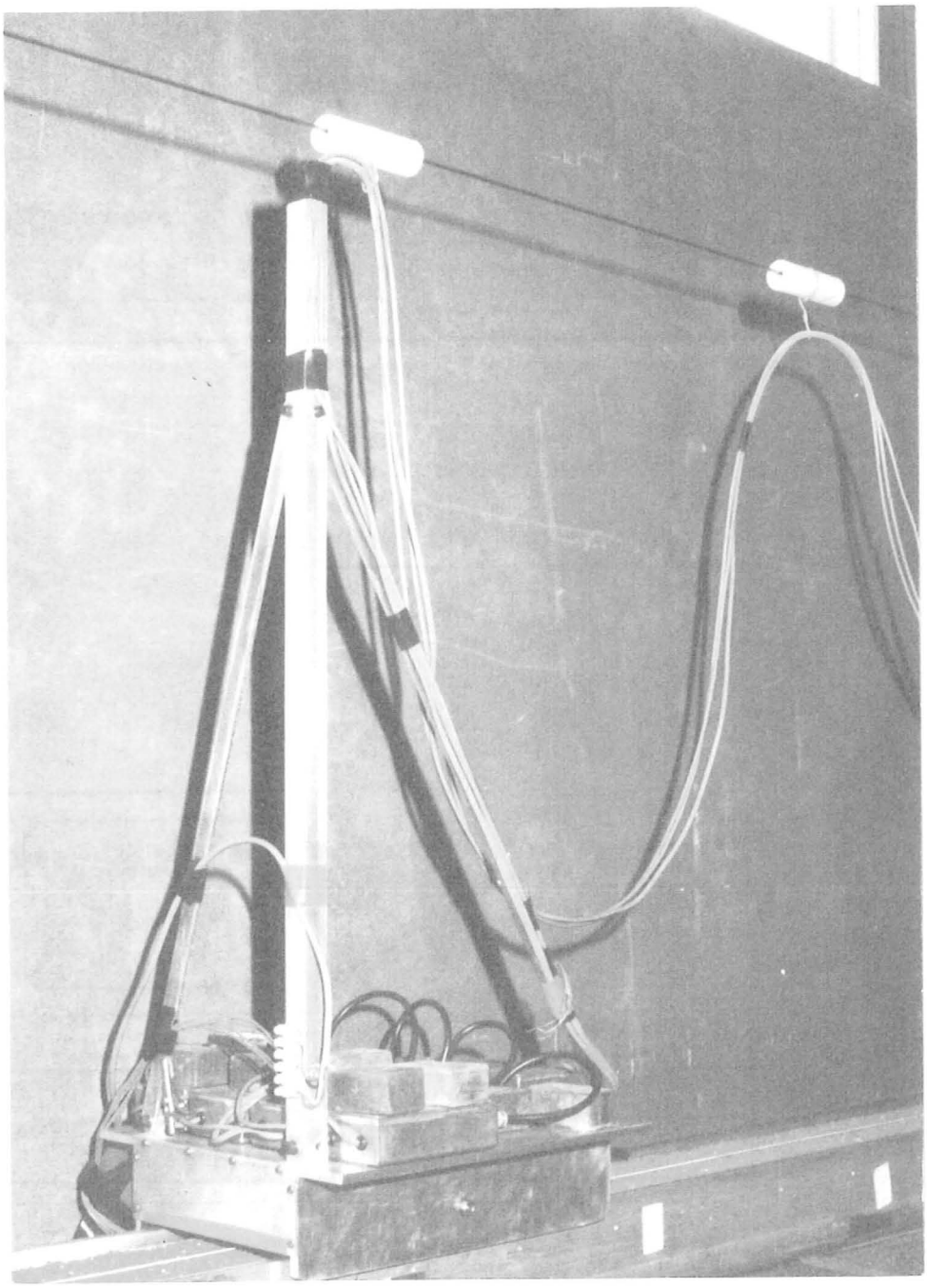


Figure 4.3. A photograph of the sensor-trolley. The mast, overhead cables and Teflon sliders are plainly visible.

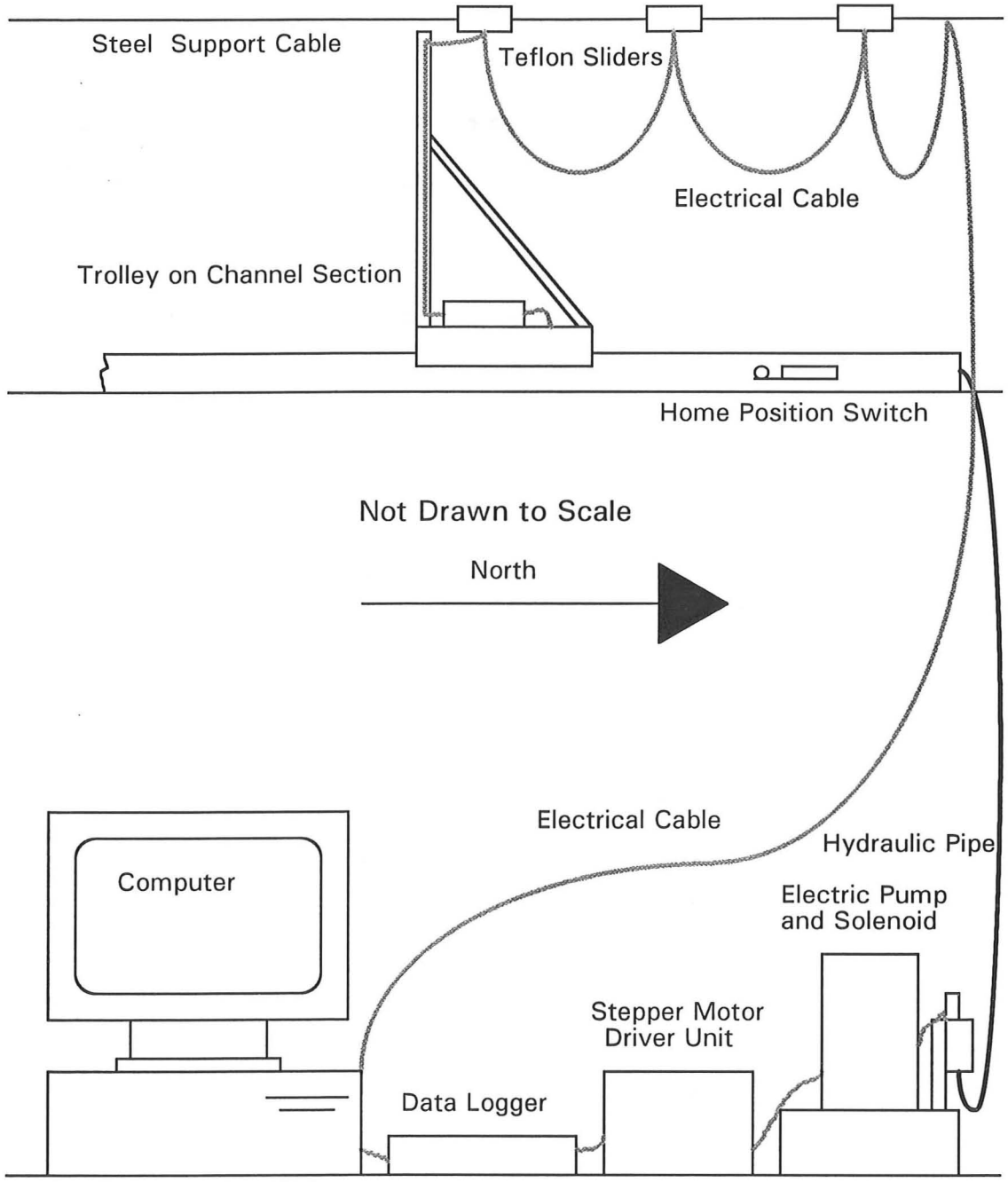


Figure 4.4. A schematic view of the main experimental apparatus. The sensor-trolley is shown on the side of the channel. The electrical cables hang from the steel support cable on the Teflon sliders, and connect the sensor-trolley to the computer. The computer is shown at the bottom of the figure, in the foreground. It is connected to and controls the sensor-trolley, the data logger, the stepper motor drive and the hydraulic pump. The figure is not drawn to scale.

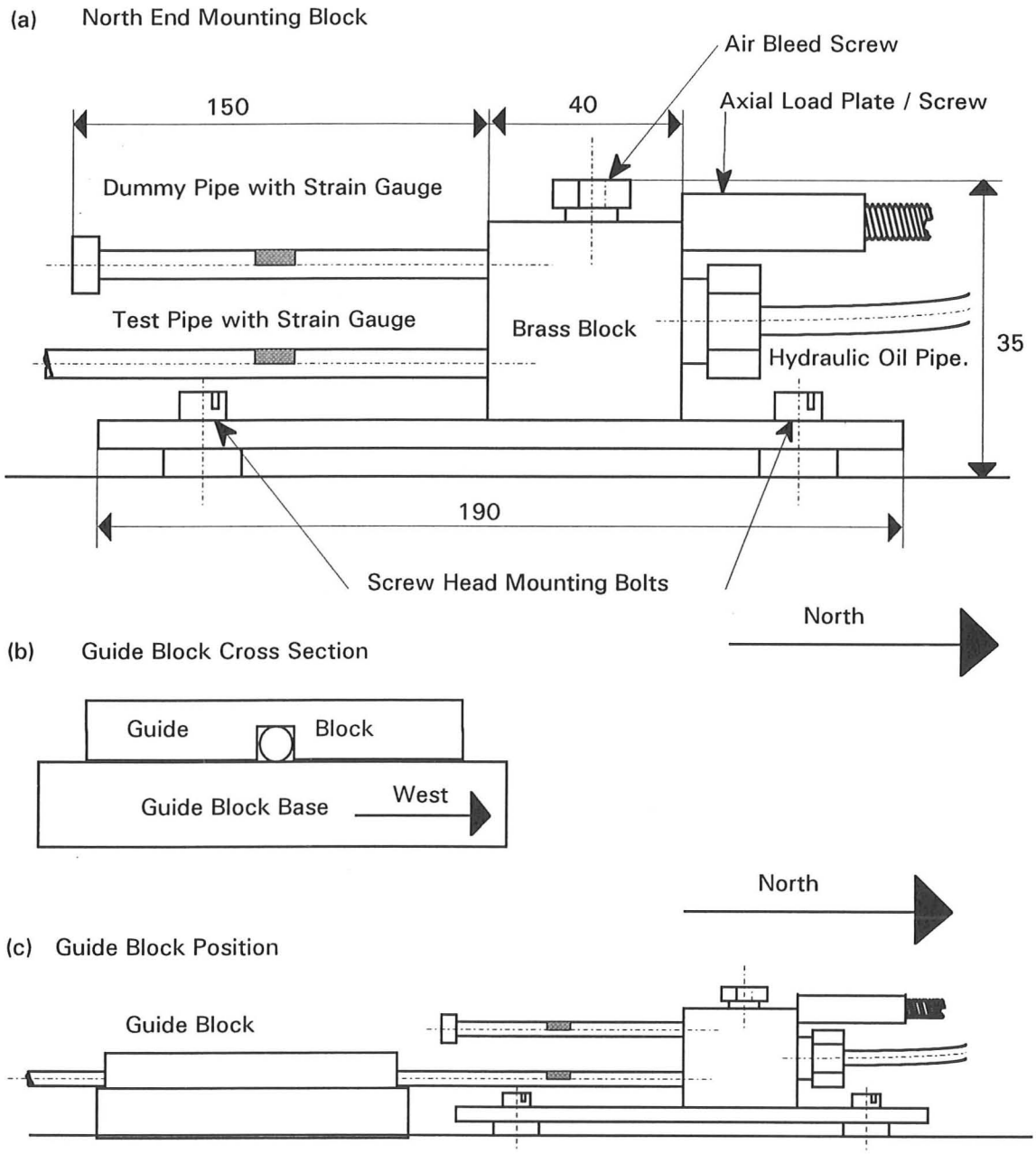


Figure 4.5. The end-mounting blocks (a) A side elevation of the mounting block at the north end of the pipe. Note the position of the dummy pipe and the strain gauges. The pipe is glued into the brass block and extends to the left of the figure (b) A cross section of the guide block. (c) A detail showing the position of the guide block. The figure is not drawn to scale. Some leading dimensions are shown in mm. The mounting bracket is 110 mm wide. The guide block is 200 mm long. The South mounting block is of similar dimensions but does not have a dummy pipe load cell or an axial load screw.

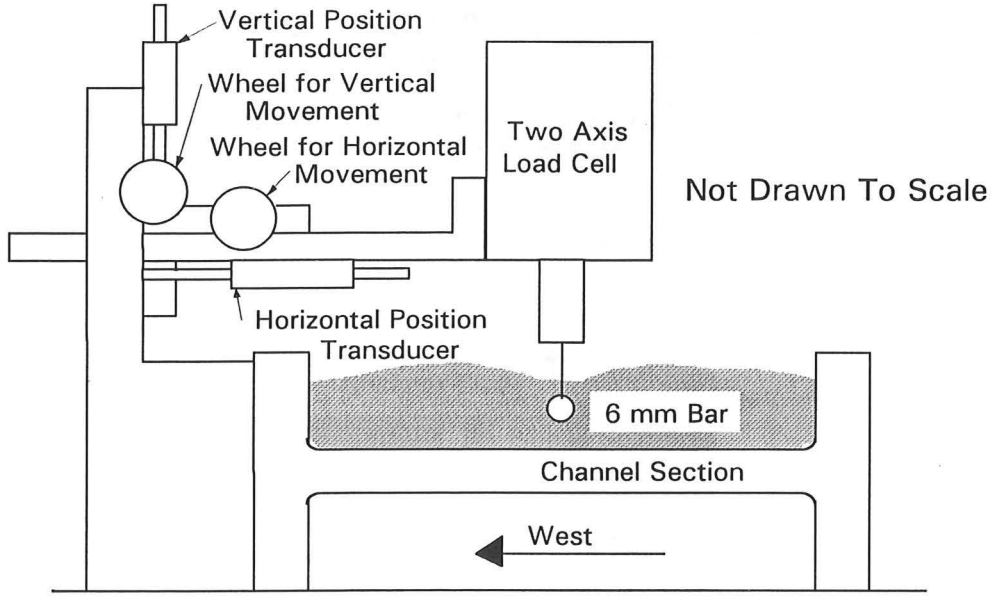


Figure 4.6. A schematic diagram of the apparatus used to measure the forces exerted by the soil on the pipe. The figure is not drawn to scale. The channel section is approximately 600 mm long. The apparatus can also be converted and used to measure the sensor reference data. Refer to figure 4.7 also.

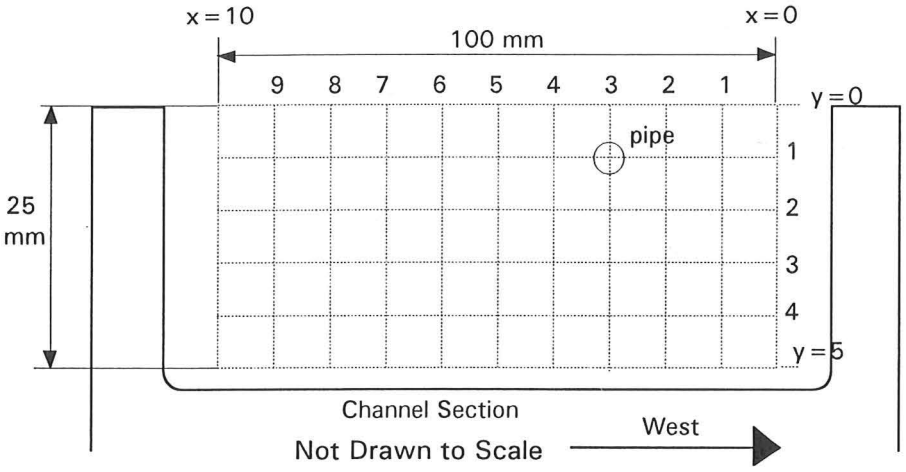


Figure 4.7. A diagram of the reference data grid, and its position relative to the channel. The grid points are at the intersections of the grid lines.

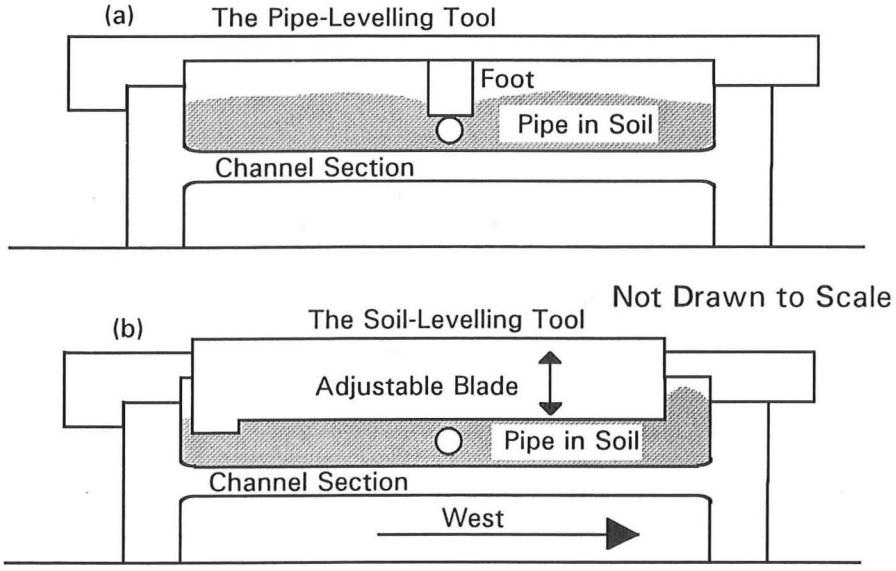


Figure 4.8. An end elevation of the pipe and soil levelling tools. (a) The pipe-levelling tool showing the fixed foot. (b) The soil-levelling tool showing the adjustable blade which is shaped to cut a trench on the left hand side and to leave a mound on the right hand side. Both tools are shown in position on the channel. The figures are not drawn to scale.

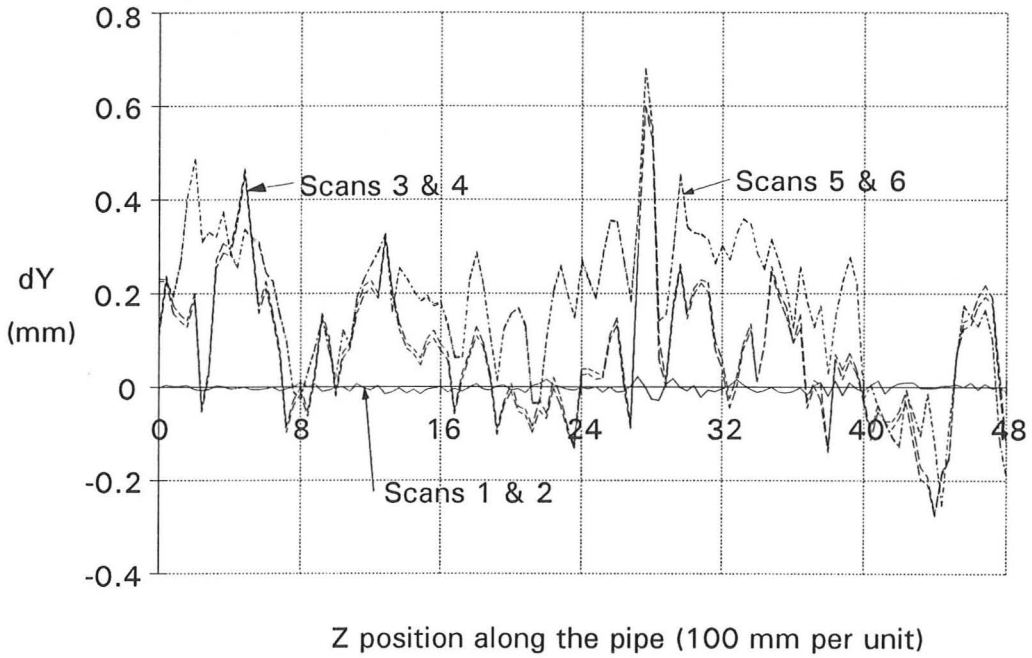


Figure 4.9. The effect of re-levelling the soil on the measured vertical position of the pipe. The change in the vertical position of the pipe dY mm is plotted versus the longitudinal position along the pipe Z (100 mm per unit). Two scans of the pipe were made between each re-levelling. Refer to the following figure also.

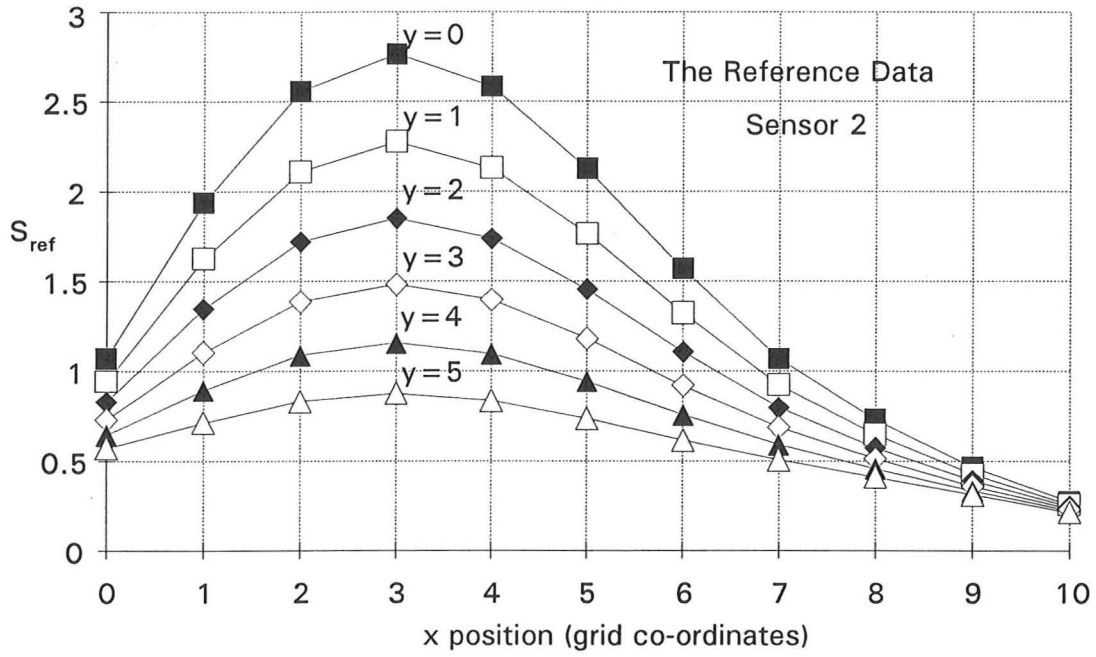


Figure 4.10. A graph of the reference data for sensor number two. The sensor output S_{ref} is plotted versus the horizontal position x (grid co-ordinates). Sensor two is at position x=3.

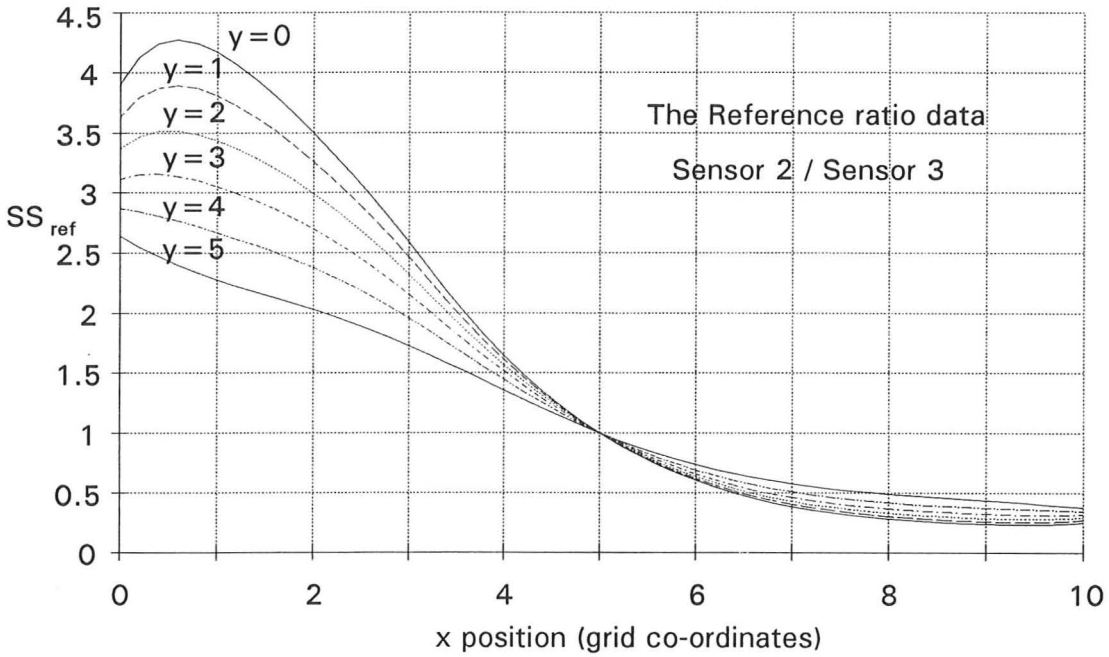


Figure 4.11. The reference ratio data SS_{ref}, for the ratio of sensor two to sensor three. The sensor ratio SS_{ref}, is plotted versus the horizontal position x (grid co-ordinates). The data shown has been interpolated by a polynomial.

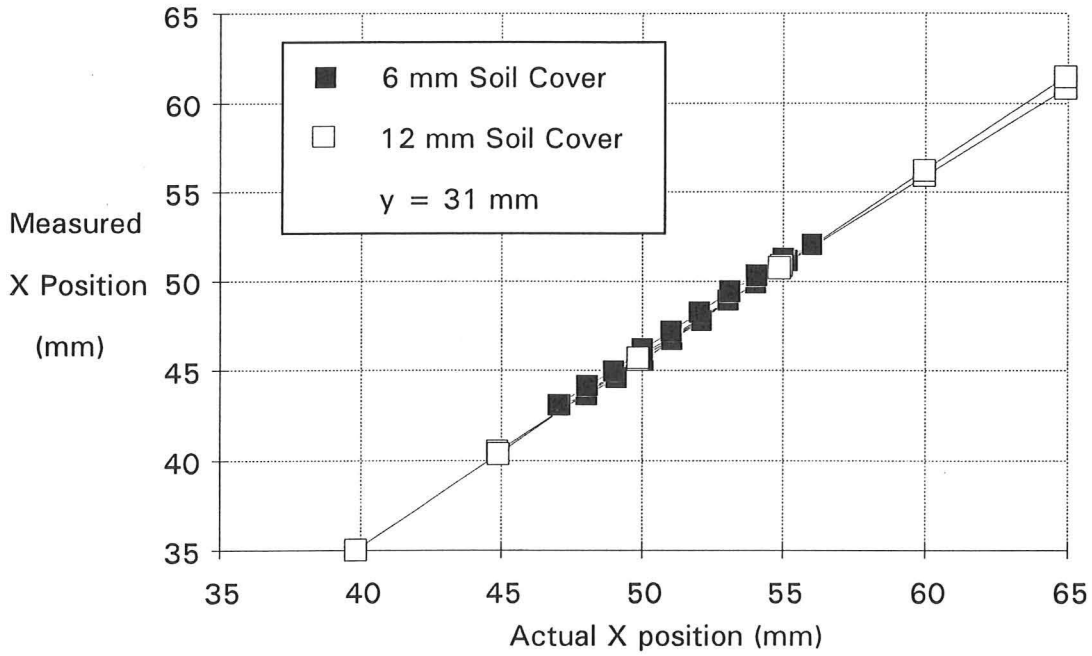


Figure 4.12. A calibration test of the measured horizontal position of the pipe, at two depths of soil cover, 6 mm and 12 mm. The measured horizontal position mm is plotted versus the actual horizontal position mm. The fill was re-levelled between each point. Refer to the following figure also.

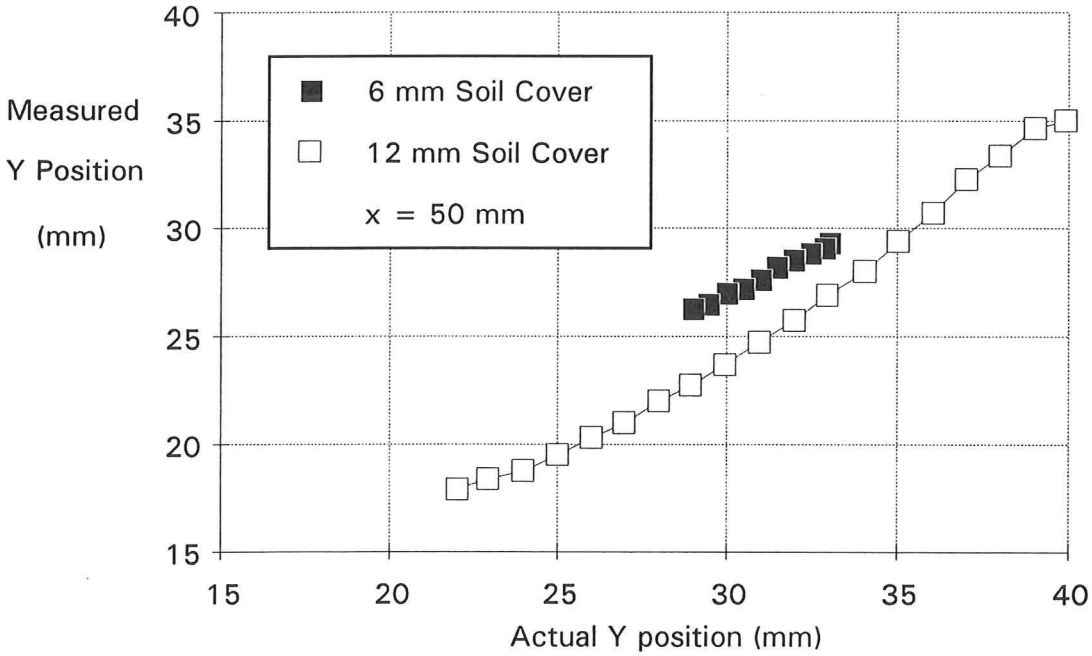


Figure 4.13. A calibration test of the measured vertical position of the pipe at two depths of soil cover, 6 mm and 12 mm. The measured vertical position mm is plotted versus the actual vertical position mm. The fill was re-levelled between each point. Refer to the previous figure also.

5. Experimental Results

5.1. Introduction

A series of experiments was performed in order to determine the following aspects of the soil and pipeline behaviour:

(i) The forces exerted on the pipe by the soil.

(ii) The behaviour of the pipe due to axial loading.

(iii) The behaviour of the pipe due to horizontal loading.

(iv) The behaviour of the pipe due to combined horizontal and axial loading.

(v) The effect of cycling the axial load.

The results from these experiments are described in this chapter. The experiments are listed in Appendix A.2.

5.2. The Soil Forces

The apparatus described in Chapter 4 was used to measure the force w N exerted by the soil on a 300 mm length of 6 mm diameter round bar. A series of 63 tests was performed. The force readings were converted to force per unit length W N/m, by dividing by the length of the bar; the effect of the ends of the bar was assumed to be negligible.

5.2.1. The Horizontal and Vertical Soil-response

In order to measure the soil-response, the bar was first buried in the soil, with the soil forces acting on the bar initially zero. The bar was then moved perpendicular to its axis in small increments, and the vertical and horizontal forces acting on the bar were measured after each increment. The soil used in the experiments was comprised of loose packed, non-cohesive granules. For this type of soil the maximum, vertical force for upwards displacement should correspond approximately to the weight of the wedge of soil above the bar as given by equation (2.15). The maximum horizontal force should correspond to the force required to displace the soil grains.

Figure 5.1 is a plot of the vertical force w N, which was exerted on the bar as it was raised up through the soil. The tests were performed with three different depths of soil cover, Q = 6, 12 & 18 mm. Each of the three plots forms a gently rounded curve which rises to a virtually constant maximum value w_0. The value of w_0 and the slope of the curve increases as the depth of soil cover increases. The three curves have been approximated by the exponential functions w1, w2 and w3 shown on the figure. The exponential functions are of the form:

$$w = w_0\left(1 - \exp\left(-\Delta Y / Y_1\right)\right) \qquad (5.1)$$

where w_0 N is the plateau value of the vertical load, ΔY mm is the vertical displacement of the bar and Y_1 mm is a characteristic length corresponding to the proportional limit of the soil. As before, the forces may be converted to force per unit length by dividing w_0 by the length of the bar. The resulting function is of the form:

$$W = W_0\left(1 - \exp\left(\Delta Y / Y_1\right)\right) \qquad (5.2)$$

where $W_0 = w_0/0.3$ N/m. The values of W_0 and Y_1 for vertical displacement, are given in table 5.1, below.

Table 5.1. The experimental values of W_0 and Y_1 for vertical displacement.

Q mm	W_0 N/m	Y_1 mm
0	0.5	-
6	1.1	0.1
12	2.3	0.1
18	3.7	0.05

Thus we find that for vertical movement, the elastic limit of the soil Y_1, is about 0.1 mm. The value of W_0 has been adjusted to include the weight of the pipe which is approximately 0.47 N/m.

The theoretical value of W_0 can be calculated from equation (2.15). For 6 mm soil cover:

$$W_0 = W_{pipe} + \rho_{soil}\, g\, Q(D + fQ)$$

$$= 0.47 + 769 * 9.81 * 0.006 *(0.006 + 0.1 * 0.006)$$

$= 0.8$ N/m

This is slightly lower than the measured value of 1.1 N/m. The difference is possibly because of the large relative size of the test soil granules compared to the diameter of the pipe, so that an arching effect is occurring in the soil. The theoretical values of W_0 for Q=12 & 18 mm are: 1.7 & 3.2 N/m respectively.

Figure 5.2 shows a plot of the horizontal force exerted on the bar as it was moved horizontally through the soil. The data is plotted for three depths of soil cover, Q=6, 12 & 18 mm. The three curves plotted are roughly similar to the curves for vertical displacement in the previous figure. All three curves have the same initial slope. The elastic limits X_1 and the maximum force w_0 are much larger than for vertical displacement. The jaggedness of the curves occurs because of the displacement of individual grains of soil around the bar. Similarly, the three curves have been approximated by the exponential curves w1, w2 & w3, which are shown on the figure. The corresponding values of the coefficients W_0 and X_1 for horizontal displacement are shown in table 5.2, below.

Table 5.2. The experimental values of W_0 and X_1 for horizontal displacement.

Q mm	W_0 N/m	X_1 mm
6	5	0.3
12	8.3	0.5
18	13.3	0.8

The experimental values of W_0 and X_1 for horizontal movement, are somewhat higher than for vertical movement. The soil-response can also be modelled by the simple bilinear model which is shown in figure 3.2.

The interaction of the horizontal and vertical forces is illustrated in figure 5.3. Both the horizontal and vertical forces are plotted versus the displacement of the bar as: (a) the bar was raised up vertically and (b) the bar was moved horizontally. In both cases the depth of soil cover, Q= 12 mm.

It can be seen in (a) that there was a small initial horizontal force $w \approx 0.15$ N, which decreased in size as the bar was raised. In (b) the initial vertical force $w \approx -0.4$ N is acting

upwards and it increased in magnitude to a maximum value of $w \approx -2$ N. The increase in the upwards force occurred because as the bar moved sideways it tended to ride up over the grains and was gradually forced upwards.

The variation of W_0 N/m and K_0 N/m^2, is plotted against Q, the depth of soil cover, in figure 5.4. The value of $K_0 = W_0/Y_1$, for the vertical displacement and $K_0 = W_0/X_1$. for the horizontal displacement. This corresponds to the initial slope of the curves in figures 5.1 and 5.2. For both the horizontal and vertical displacement lines, W_0 increases linearly with Q. For the vertical displacement line, a straight line through the data points should intercept the ordinate line at approximately 0.47 N/m. This corresponds to the self weight of the pipe.

The variation of K_0 is somewhat more complicated. For the horizontal displacement line, K_0 is constant. For the vertical displacement line, K_0 increases non-linearly with Q.

5.2.2. The Soil Hysteresis

The hysteresis behaviour of the soil was determined by measuring the soil forces as the bar was moved repeatedly, either backwards and forwards or up and down, by approximately ± 1 mm. The vertical hysteresis is shown in figure 5.5. The curve is non-symmetrical because of the non-symmetry of the vertical soil-response. It is more difficult to push the bar downwards into the soil than it is to pull it upwards. This is because the maximum upwards soil-response is approximately equal to the weight of the wedge of soil above the bar whereas the maximum downwards response corresponds to the force required to displace the soil underneath the bar. The soil in a trench behaves in a similar manner.

The horizontal hysteresis is shown in figure 5.6. In this case the hysteresis curve is more symmetrical because of the symmetry of the horizontal soil-response, i.e. the bar can be moved to either side equally easily. A consequence of the difference in symmetry between the horizontal and vertical directions is that vertical buckling tends to favour the single buckling mode illustrated in figure 2.9.a, and horizontal buckling favours the double or triple buckling modes from figure 2.9.b & c.

5.3. The Axial Load Tests

The main experimental apparatus was used to measure the displacement of the pipe as an axial load was applied. A series of 25 tests was performed; 17 tests with a 6 mm depth of soil cover Q, and 8 tests with 12 mm soil cover. For each test the pipe was re-laid and the soil re-levelled, as described in Chapter 4. An axial load was then applied in increments and the horizontal and vertical position of the pipe was measured at each increment.

5.3.1. A Typical Test Result

A typical result is shown in figure 5.7. In this case the axial load was applied in 7 increments of approximately 20 N each. The vertical displacement of the pipe is plotted for each increment. Buckling failure occurred at a load of approximately 150 N. When buckling occurs the pipe jumps out of the soil in a long arch. The Z co-ordinate, the position along the pipe, is measured in units of approximately 100 mm. The axial load is applied at the left hand end of the figure. The horizontal displacement of the pipe from the same test is shown in figure 5.8.

In both figures, six lobes of varying amplitude have formed along the pipe. The largest lobes are to the left of the figures, closest to the end where the axial load was applied. The lobes reduce in size from left to right, of the figures. This is possibly due to the effects of axial friction and the variation in axial load along the pipe. In both cases, the plotted displacements form a series of nested curves. This indicates the absence of "noise" in the position measuring system.

The magnitude of the axial load was measured at the end of the pipe where the load was applied. The actual value of the axial load varies along the length of the test pipe because of the effect of axial friction. Hobbs (1984) suggests practical friction coefficient values of $\lambda=0.3$ to 0.7. If the test pipe is assumed to be perfectly straight, the difference in the axial load between the two ends of the pipe ΔP, can be calculated by the following formula:

$$\Delta P = W_0 \lambda L \qquad (5.3)$$

If the downwards load $W_0=1.1$ N/m, the axial friction coefficient $\lambda=0.5$, and the overall length of the pipe $L=5$ m, then:

$\Delta P = W_0 \lambda L = 1.1 \times 0.5 \times 5 \approx 3$ N

The actual variation in axial load was measured by two different methods and varied between 60-80 N. In one test, one end of the pipe was released and allowed to slide freely, so that the axial load at the free end was assumed to be zero. The pipe was then compressed from the other end, while measuring the applied load. It was found that the applied load increased rapidly to a maximum plateau value of 60 N, which was assumed to be equal to the variation in axial load along the length of the pipe.

In the second test, an axial load of approximately 160 N was first applied to one end of the pipe, and the other end was then released. This caused a drop in the applied load, to a residual value of approximately 80 N, which was assumed to equal the variation of axial load along the pipe.

In both cases the measured variation in axial load is considerably higher than the theoretical value, possibly because of the crookedness of the pipe. The greater variation in the second test is possibly because of the additional crookedness caused by first applying the 160 N load.

The axial load is highest at the left hand end of figure 5.7, the end at which the axial load is applied. The load decreases steadily from left to right on the figure and is lowest at the right hand end of the figure. There is a similar pattern in the amplitude of the lobes, which also decreases from left to right. An exception is the lobe at the right hand end of the figures, which is larger than expected. This is possibly because of misalignment or out of straightness of the end mounting.

Both the displacement of the lobes and the displacement increment increase as the axial load increases; the displacement becoming very large as the axial load approaches the buckling load. For the left-most imperfection at position $Z=3$, the first displacement is negative. This is possibly an apparent result due to a slight settling of the soil as the first reading is taken. The effect of any movement of the soil surface is to cause an apparent movement of the pipe of an equal magnitude.

During each of the tests, the configuration of the imperfections was similar, i.e. the imperfections generally appeared at the same positions along the pipe and deflected in the same

direction for each test. This would seem to indicate some effect due to the end mountings, and a strong tendency for the pipe to deflect at a preferred wavelength. The soil has different properties in the upwards, downwards and horizontal directions. We could therefore expect the deflection of the pipe to behave differently in these three directions. This in fact appears to be the case. The vertical displacement is almost entirely upwards, with virtually no downwards displacement occurring. By comparison the horizontal displacement occurs in both directions, the direction alternating along the pipe. The upwards, downwards and horizontal wavelengths also appear to be slightly different in length. The peaks in the vertical and horizontal wavelengths do not necessarily coincide.

The three dimensional deflection of the pipe is a rather complicated phenomenon to analyse. For simplicity it is convenient to model the upwards, downwards and horizontal deflections separately and to assume that they are independent of each other. In practice, the axial load required for upwards buckling is considerably lower than the load required for downwards or horizontal buckling. It thus seems reasonable to assume that generally buckling failure will occur in the upwards direction, so that only the upwards mode of failure has been analysed.

Figure 5.9 is a polar plot of the peaks of the two largest imperfections from the previous figure. These are at the positions Z=3 and Z=14. The vertical and horizontal axes are not to exactly the same scale. However, as can be seen the displacements of the two peaks are in directions roughly at right angles to each other, and are nearly in straight lines.

As mentioned previously in Chapters 3 and 4, the experimental apparatus is not able to measure the amplitude of the initial imperfections. Instead, the amplitude must be interpolated from the experimental data. One method of doing this is illustrated in figure 5.10. The data from the previous figure for the two lobes at Z=3 and Z=14, is re-plotted as axial load P N versus the upwards vertical displacement ΔV mm. The experimental data is shown plotted over the top of the numerical data from the finite difference model described in Chapter 3. It can be seen that the experimental data curves are reasonably similar to the numerical curves. The size of the imperfections can be estimated by comparing the data curves. In this case the largest imperfection is at position Z=3 and has an approximate magnitude $V_0 \approx 0.2$ mm. The largest

imperfection has the lowest buckling load and is assumed to be the critical imperfection where buckling will first occur.

A second estimation of the imperfection amplitude can be made from a Southwell plot. This has been done in figure 5.11. Similarly to the previous figure, the experimental data has been plotted over the top of the numerical data. The experimental curves are reasonably similar to the numerical curves. The amplitude of the largest (or most critical) imperfection is approximately $V_0 \approx 0.19$ mm. The buckling load P_b can be calculated from equation (3.6) as:

$$P_b = \sqrt{(EIW_0 / V_0)} = \sqrt{(3.131 \times 1.1 / 0.0001)} \approx 135 \text{ N}$$

The actual buckling load was approximately 150 N. Thus we can see that the buckling load predicted by the simplified buckling model is reasonable, provided that the model used to estimate the imperfection amplitude is reasonably accurate. Both models are based on similar principles so that the apparent agreement between the results is not conclusive. Unfortunately, the amplitude of the initial imperfections cannot be measured in any other way.

A rough check on the accuracy of the model can be made by calculating the initial imperfection amplitude which corresponds to the buckling load of 150 N. Re-arranging equation (3.6), V_0 can be calculated as:

$$V_0 = EIW_0 / P^2 = 3.131 \times 1.1 / 150^2 \approx 0.15 \text{ mm.}$$

The expected imperfection amplitude is of the order of 0 to 0.5 mm so that the value predicted seems reasonable.

5.3.2. The Overall Results

The data from a series of experiments is plotted in figure 5.12. For each data point, the experimental buckling load is plotted versus the estimated amplitude of the largest imperfection. The depth of soil Q=6 mm. The curve of values calculated from the simplified buckling model P_b, is also plotted for comparison.

The data appears to fit the P_b curve reasonably well, the curve being a useful lower bound to the plotted data points. It should be noted however that these observations are largely dependant on the accuracy of the model which has been used to estimate the imperfection amplitude.

Most of the data points lie above the P_b curve. This is possibly because of the variation of the axial load along the pipe and the type of imperfection assumed by the model.

Because of the variation of the axial load along the pipe, the actual load in the buckled region is generally lower than the measured load so that the data points should be shifted down on the graph. Conversely, for the same reason the estimated imperfection amplitude is too small meaning that the data points should be shifted to the right on the graph. The magnitude of this effect increases with increasing distance from the load end of the pipe.

A further effect arises because the simplified buckling model assumes that the initial imperfection is a combined foundation and geometric imperfection. This is a worst case analysis, and it requires that the pipe is plastically deformed to the shape of the imperfection. Generally the imperfection will be a simple foundation or geometric type with the result that the actual buckling load will be higher than predicted by the model. The magnitude of this effect increases as the amplitude of the initial imperfection increases.

The model assumes that the deflections are of equal magnitude in both directions. This assumption is true for the horizontal deflection but is not true for the vertical deflection. The vertical deflection is actually highly non-symmetric because of the non-symmetry of the vertical soil-response. Nevertheless, in order to simplify the analysis, the vertical deflections are assumed to be symmetric; the upwards and downwards deflections are regarded as being independent of each other and are analysed separately as if they were each symmetric.

The experimental data points for the series of tests carried out with a depth of soil cover $Q=12$ mm, are plotted in figure 5.13. Similarly to the previous figure, the P_b curve is a useful lower bound to the data.

5.4. Horizontal Loads

A series of tests was performed by applying a horizontal load to the pipe with calibrated weights, and measuring the resulting displacement. The tests included the following:

(i) A horizontal load only, 3 tests.

(ii) A constant horizontal load combined with an increasing axial load, 2 tests.

(iii) Adding and removing a constant horizontal load, combined with an increasing axial load, 63 tests.

The results from these tests are described in the following section. The tests are listed in Appendix A.2.

5.4.1. Horizontal Load Only

The horizontal load tests were performed as a supplementary test of the soil behaviour. This form of test avoids the jagged form of curve displayed in figure 5.2, however because an indefinite length of pipe is involved the results are somewhat more difficult to interpret.

A plan view of a section of the deformed pipe, is shown schematically in figure 5.14. The pipe has a single horizontal lobe with displacement ΔX m which is due to the horizontal load U N. The two points of zero displacement are separated by a characteristic length ξ m. The displacement of the pipe is dependent on two factors, the soil-response and the flexural stiffness of the pipe itself. In order to separate the effects of these two factors, let us assume that the soil-response W N/m can be expressed by the following relationship:

$$W = W_0\left(\frac{\Delta X}{X_1}\right)^{\alpha} \tag{5.4}$$

where X_1 is a standard length such as the elastic limit of the soil. For a linear-elastic soil we would have $\alpha=1$, and for a perfectly plastic base we would have $\alpha=0$.

From a simple force balance, the horizontal force U can be expressed as:

$$U = A\xi W_0\left(\frac{\Delta X}{X_0}\right)^{\alpha} \tag{5.5}$$

where A is a constant. Similarly, from simple beam theory, the displacement ΔX can be expressed as:

$$\Delta X = \frac{B\xi^4}{EI} W_0\left(\frac{\Delta X}{X_0}\right)^{\alpha} \tag{5.6}$$

where B is a constant. These equations can be re-arranged to give the displacement ΔX in terms of the horizontal load U:

$$\Delta X \propto U^{\gamma} \qquad (5.7)$$

where $\gamma = 4 / (1+\alpha)$. Similarly, the characteristic length ξ can be expressed in terms of the horizontal load U:

$$\xi \propto U^{\beta} \qquad (5.8)$$

where $\beta = (1-\alpha) / (1+3\alpha)$. Thus for a perfectly plastic soil with $\alpha = 0$; $\Delta X \propto U^4$ and $\xi \propto U$. But, for a perfectly elastic soil with $\alpha = 1$, $\Delta X \propto U$ and $\xi =$ constant.

The tests were performed by applying a horizontal load to the pipe at position Z=16.5 in increments of approximately 0.8 N. The load was applied by means of weights, hung on the end of a string which passes over a pulley. The position of the pipe was measured at each increment.

This is illustrated in figure 5.15. The horizontal displacement ΔX is plotted versus the axial Z position. It can be seen that both the horizontal displacement ΔV and the characteristic length ξ increase as the horizontal load increases. The abrupt jump in displacement at the load of 3.84 N is due to the weight having been accidentally dropped.

The data is re-plotted as a log - log plot in figures 5.16 and 5.17. The log of the displacement (log ΔX) is plotted versus the log of the horizontal load (log U), in figure 5.16. A line with a slope of 4 is included on the graph for comparison. The slope of the data line is very close to 4, which indicates that the pipe behaviour is what we would expect for a perfectly plastic soil.

Similarly, in figure 5.17 the log of the characteristic length ξ is plotted versus the log of the horizontal load U, along with a line of slope 1 for comparison. Again, the slope of the data line is very close to the expected value of 1, indicating a plastic soil-response.

The approximate value of W_0 can be calculated by re-arranging equation (5.5), and putting $\alpha = 0$. This gives the following expression for W_0:

$$W_0 \approx U / A\xi \qquad (5.9)$$

where the constant A represents the effect due to the small side lobes, $0.75 \leq A \leq 1$. The approximate value of W_0 is plotted versus the horizontal load U in figure 5.18, for an assumed value of A=1. The average value of 4 to 4.5 N/m is reasonably close to the value of 5 N/m

measured in the soil-response tests. Note that for these tests the displacements are large, being up to 3.3 mm and they are considerably larger than the horizontal elastic limit X_l=0.3 mm.

5.4.2. Combined Axial and Horizontal Loads

A combination of axial and horizontal load was applied by first imposing a horizontal load of 1.39 N at position Z=18.5, then applying an axial load in increments of approximately 20 N. The position of the pipe was measured after each increment. The resulting displacement is plotted in figures 5.19 and 5.20.

The horizontal displacement is plotted in figure 5.19. Applying the horizontal load has caused a large initial displacement of approximately 0.3 mm. The pipe has then deflected under increasing axial load, in a similar manner to a normal axial test. Three horizontal lobes have formed on alternate sides of the pipe. The horizontal wavelength remains virtually constant throughout the test.

The corresponding vertical displacements are plotted in figure 5.20. In this case there is only a small initial vertical displacement due to the application of the horizontal load and there are only two vertical lobes on the left of the figure. The smaller lobe is at position Z=3 and the larger lobe is initially at position Z=18.5, which is the point of application of the horizontal load. As the axial load increases the centre of the imperfection has shifted to Z=15 which is closer to the position Z=14 where a lobe occurred in several earlier tests. This behaviour seems to indicate that there is a preferred wavelength for the lobes.

The peak of the vertical lobe at Z=15 coincides with a zero horizontal displacement point. This illustrates the independence of the vertical and horizontal deflections.

The vertical displacement data is re-plotted as a Southwell plot in figure 5.21. As described previously, the experimental data has been plotted over the top of the numerical data from Chapter 3. The largest initial imperfection size is approximately $V_0 \approx 0.38$ mm. This corresponds to a buckling load from the simplified buckling model P_b=95 N. This value is reasonably close to the actual buckling load of approximately 110 N.

5.4.3. Adding and Removing the Horizontal Load

The displacement of the pipeline appears to be strongly influenced by a preference for certain wavelengths. The aim of these experiments was to determine the influence of the preferred wavelength by imposing lateral forces at different positions. From figure 5.8, it appears that position Z=13 seems to be a natural location for a lobe.

The tests were performed as follows: First (step 1) a horizontal load of 1.38 N was applied to the pipe. This was followed by three 25 N increments of the axial load (steps 2 to 4), up to a total of 75 N. The horizontal load was then removed (step 5), and a further two axial load increments of 25 N were applied (steps 6 & 7). These experiments were repeated, with the horizontal load applied at a series of different locations.

A typical result is plotted in figure 5.22, showing the horizontal displacements as a result of applying a horizontal load at the position Z=13.5. It can be seen from figure 5.8, that position Z=13 was the preferred location of a lobe. By placing the horizontal load at this position, we are thus forcing the pipe to deflect in the opposite direction to its preferred orientation, as seen in figure 5.8.

For the first four steps in figure 5.22, the pipe has deflected in the direction of the horizontal load, i.e. in the opposite direction to its preferred natural direction. However, when the horizontal load is released in step 5, the pipe has deflected back towards its preferred orientation. This tendency increases as the axial load is increased in steps 6 &7, so that by step 7 the pipe has actually deflected back to the preferred side. It is clear from this example that the pipe displacement has a very strong preference for this particular orientation.

This is further illustrated by the polar plot in figure 5.23. The figure shows a plot of the displacements of the lobes at positions Z=4 and Z=14. The steps 1 to 7 correspond to the steps described in the previous figure, 5.22. For the lobe at Z=4, the pipe has moved steadily upwards and to the right and was unaffected by the change in the horizontal load. This is similar to the polar plot of position Z=3 in figure 5.9.

By comparison, for the lobe at Z=14 the preferred displacement would be upwards and to the left, as in figure 5.9. However, in this case because of the imposed horizontal load, the

pipe has initially moved upwards and to the right. When the horizontal load was removed in step 5, the pipe has moved back to the left, and by step 7 it has a negative horizontal displacement.

Figure 5.24 shows the data from a series of experiments where the horizontal load has been applied at each of 24 different positions. The position where the axial load has been applied is denoted by Z_1. The figure is a plot of the pipe displacement at position Z_1, versus the position Z_1. The steps, 1, 4, 5 and 7 correspond to the steps from the previous 2 figures.

The steps are: (step 1), after the horizontal load of 1.38 N was applied; (step 4), after the three increments of the axial load totalling 75 N had been applied; (step 5), after the horizontal load was removed and (step 7), after the final two increments of the axial load were applied; to a total load of approximately 120 N. The jaggedness of the curves is due to the uneven application of the horizontal load. It is difficult to apply the horizontal load without dropping the weight slightly.

Clearly, the point of application of the load has a marked effect on the pipe displacement. When the horizontal load was applied in step 1, the largest displacement occurred in the region of Z=12 to 15. This is close to the position Z=13, which is the preferred location for the lobe in figure 5.8. However, the displacement occurred in the opposite direction to the preferred orientation.

After three increments of the axial load at step 4, the lobes have all grown, with the largest displacements occurring at positions at Z=4 and Z=12 to 15.

When the horizontal load was removed at step 5, the displacement at Z=4 was hardly affected, with only a slight decrease observed. By comparison, at position Z= 12 to 15 the behaviour is quite different. The pipe has actually moved back in the opposite direction, with the largest backward movement occurring at position Z=14.

After the last 2 increments of axial load were applied at step 7, this behaviour was extenuated. The peak at position Z=4 has continued to grow in the original direction, which is the same direction as the preferred lobe. The peak at position Z=12 to 15 has continued to grow in the opposite direction. The largest displacement occurred at Z=15.

The overall behaviour strongly supports the existence of a preferred buckling orientation. Both the previous axial load tests and this test indicate that the preferred orientation for horizontal deflection is a positive peak at Z=4 and a negative peak at Z=14 to 15, as in figure 5.8.

5.5. Cyclic Axial Loading

The effect of cyclic axial loading was determined by applying a cyclic axial load to the pipe, by means of hydraulic pressure. A series of 19 tests was performed by applying a hydraulic load, with 6 mm of soil cover. A further series of 6 tests was performed by manually applying an end load, with 12 mm soil cover.

To perform the hydraulic tests a small pre-load of P_p N was applied to the end of the pipe, and a cyclic load of P_c N was applied a number of times, the load varying between P_p and P_p+P_c N. The position of the pipe was measured at intervals with the pressure off, i.e. with zero cyclic load.

The maximum load which could be applied hydraulically was limited to approximately 80 N, because of the operating pressure limit of the apparatus. If a peak load higher than 80 N was required, it was necessary to increase the size of the pre-load. For example to achieve a load of 90 N, a pre-load of 10 N and a cyclic load of 80 N were applied and the load was cycled between 10 and 90 N.

A number of tests were performed to investigate the effect of the size of the pre-load. For these tests, the same peak load was applied in each test, but the relative magnitudes of the pre-load and the cyclic load were varied. In one series of three tests, the loads tested were 40-130 N, 65-130 N & 95-130 N. The results of these tests are shown in figure 5.25. As can be seen there is considerable variation in the test results. We would expect that for a particular value of the peak load, the tendency to buckle should decrease as the size of the pre-load increases. This is true for the 40-130 N test and the 65-130 N test. For these two tests, the displacement of the pipe (which is a measure of the tendency of the pipe to buckle) decreases as the size of the pre-load increases.

For the 95-130 N test, which we would expect to be least likely to buckle, the displacement is actually larger than for the other two tests. Thus, the effect of varying the size of the pre-load is unclear from these results. The reason for the unexpected variation in the results, is possibly because the amplitude of the initial imperfections varies for each test. It is assumed that the initial imperfections in the 95-130 N test were larger than for the other two tests. Unfortunately, the actual amplitudes are unknown.

5.5.1. Typical Results

Some typical results from the hydraulic, load cycling tests are illustrated in figures 5.26 to 5.29. There appear to be two distinct types of displacement which occur. The first type occurs as the general raising of the entire length of the pipe as the load is cycled. Initially, the overall displacement grows rapidly as the load is cycled, but the growth slows after a number of cycles, and the displacement eventually reaches a static plateau value after a large number of cycles. Usually for this type of displacement, buckling does not occur.

A second type of displacement occurs as the appearance of a number of individual lobes along the length of the pipe. The lobes grow rapidly as the load is cycled, and generally buckling occurs when the displacement reaches some critical value.

An example of the first type of displacement is shown in figure 5.26. The vertical displacement is plotted versus the axial position Z, with the cumulative number of load cycles marked on the figure. It can be seen that all points along the pipe have been displaced upwards. Thus, after 860 cycles the maximum displacement at the position Z=28, is approximately 0.23 mm, and the relative height of the displacement is only 0.1 mm. The largest growth in the displacement occurred in the first cycle. Thereafter the growth rate has steadily decreased as the number of cycles increased. After 860 cycles the displacement has reached a virtually static plateau value, without buckling occurring. In this case the load was cycled between 20-90 N.

The horizontal displacement from the same test, is plotted in figure 5.27. A large single horizontal lobe has formed at the position Z=4. This lobe is of the second type of displacement, although in this case buckling has not occurred. The horizontal lobe appears to have formed independently of the vertical displacement. Similarly to the previous figure, a

large initial displacement occurred after the first load cycle. The growth rate has subsequently slowed, as the number of load cycles increased. After 860 load cycles the displacement of the lobe was virtually static.

The second type of displacement is shown more clearly in figure 5.28. A number of vertical lobes have formed, the largest lobe being at the position Z=12. Notice that, in this case the lobes have continued to grow as the axial load was cycled, until buckling failure occurred after 161 cycles.

The corresponding horizontal displacements are plotted in figure 5.29. There are two large lobes on alternate sides of the pipe, the imperfection at Z=12 being the largest. In this case, the positions of the horizontal and vertical lobes coincide.

5.5.2. The Overall Results

As we have seen from the previous results, the occurrence of buckling due to cyclic loading appears to be linked to the type of displacement which occurs, which is in turn related to the magnitude of the peak load and the cyclic load, and to the amplitude of the initial imperfections on the pipe.

This is illustrated in part, in figure 5.30. The relative peak displacements from several different tests are plotted versus the number of load cycles. Generally, increasing the size of the peak load or the cyclic load increases the likelihood of buckling failure. There is however, considerable variation in the results. This is assumed to be due to the variation in the size of the initial imperfections. According to the theory described in Chapter 3, increasing the size of the initial imperfections should make the pipe more prone to buckling.

The 95-130 N test buckled at the lowest number of cycles; buckling occurring after 1 load cycle, at a displacement of 0.33 mm. In the 85-120 N test, buckling occurred after 46 cycles, at a displacement of 0.8 mm. In the 40-130 N test, buckling occurred at a much lower displacement of 0.25 mm, after 11 cycles. The lowest load at which failure has occurred was in the 5-90 N test, with buckling occurring after 161 cycles. By comparison buckling did not occur during the 65-130 N test, despite the peak load being higher than for two of the tests in which buckling did occur. This is possibly because the initial imperfections were small.

It appears that a rough rule of thumb for the occurrence of buckling might be that buckling will not occur provided the amplitude of the displacement due to the first load cycle is less than 0.05 mm. This figure corresponds to half the vertical proportional-limit, Y_1. A simple design criteria could therefore be to limit the maximum initial displacement to some fraction of the proportional-limit, i.e. $\Delta V_{max} = V_1/n$, where n is an integer. For small displacements the soil-response can be regarded as being linear and the relationship between the displacement V and the axial load P can be approximated by the Ayrton Perry formula:

$$\Delta V = \frac{V_0}{\frac{P_e}{P} - 1} \tag{5.10}$$

where P_e is the elastic buckling load from equation (2.30). Re-arranging, the maximum load P_{max} can be expressed in terms of the maximum displacement ΔV_{max} as:

$$P_{max} = \frac{P_e}{\frac{V_0}{V_{max}} + 1} \tag{5.11}$$

where $V_{max} = V_1 / n$, for $n \geq 2$. This can also be expressed in terms of dimensionless variables as:

$$\frac{P_{max}}{P_e} = \frac{1}{n\left(\frac{V_0}{V_1}\right) + 1} \tag{5.12}$$

where P_{max}/P_e is the dimensionless load and V_0/V_1 is the dimensionless displacement.

The effect of varying the peak load P_p and the cycle load P_c, is illustrated in figure 5.31. The peak load P_p and the cycle load P_c are plotted versus the peak displacement of the lobe after 10 cycles. The tests where buckling occurred are marked with a letter; A=5-90 N, B=40-130 N & C=85-90 N, respectively. Generally, buckling has occurred with a combination of large displacements, signifying large initial imperfections, and large loads, although the pattern varies.

The growth of the lobes during individual load cycles is illustrated in figure 5.32. For these tests, an end load was applied and removed three times. The figure shows the

displacement of the largest lobe, before and after each application of the axial load. As can be seen the size of the displacements has steadily increased as the load was cycled. The size of the displacements has also increased with the size of the cyclic load. There is some variation in these effects, possibly because of variations in the size of the initial imperfections. The size of the initial imperfections is unknown.

A surprising feature of these tests, is that the soil displays virtually no elasticity. We might expect, that for small initial displacements which are less than the proportional limit, the pipe would have returned to its original position when the axial load was removed. As can be seen, even for initial displacements less than 0.05 mm, roughly half the proportional-limit, the pipe remains in its deflected position when the axial load is removed.

We would also expect that the lobes would continue to grow at an increasing rate, as the axial load is cycled. However, this is not the case. The displacement tends to level off, and provided that buckling does not occur first, it reaches a static plateau value. Thus it appears that there is some factor which is limiting the growth of the lobes. This could be either; residual forces in the soil which are acting on the pipe, an effect caused by the increasing curvature of the pipe, or the increasing geometric shortening effect as the amplitude increases. Thus, provided that the initial growth rate of the lobes is sufficiently slow, the pipe displacement reaches a static plateau value after a large number of cycles, without buckling occurring.

5.6. Figures

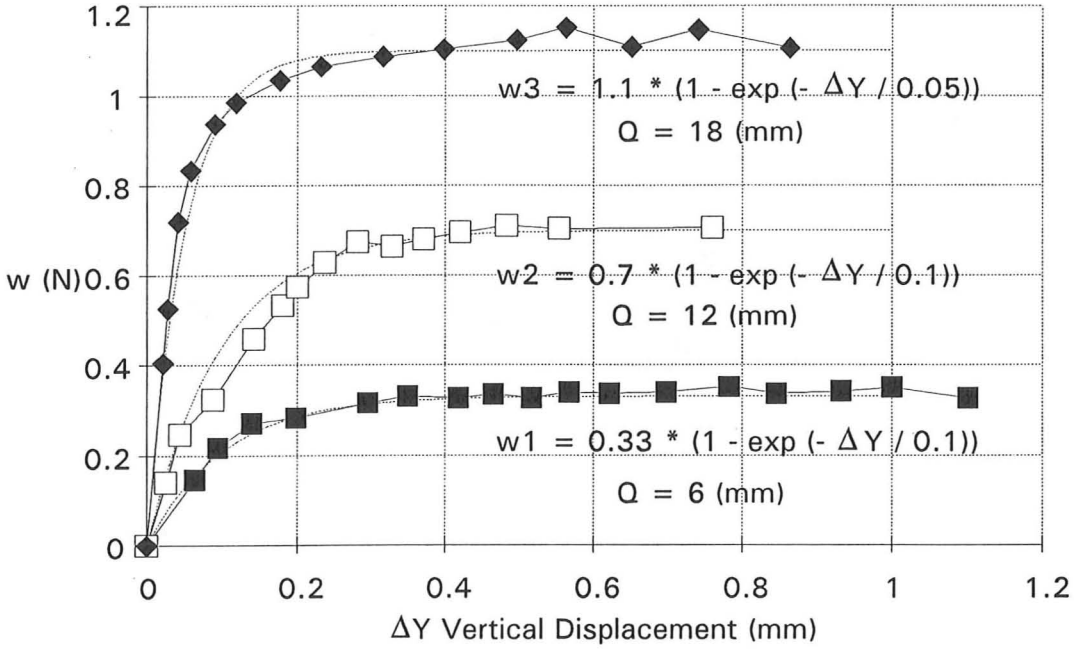


Figure 5.1. The vertical soil force w N versus the vertical displacement ΔY mm, measured on a 300 mm bar for 6, 12 & 18 mm depth of cover. The soil response is modelled by the exponential functions w1, w2 & w3.

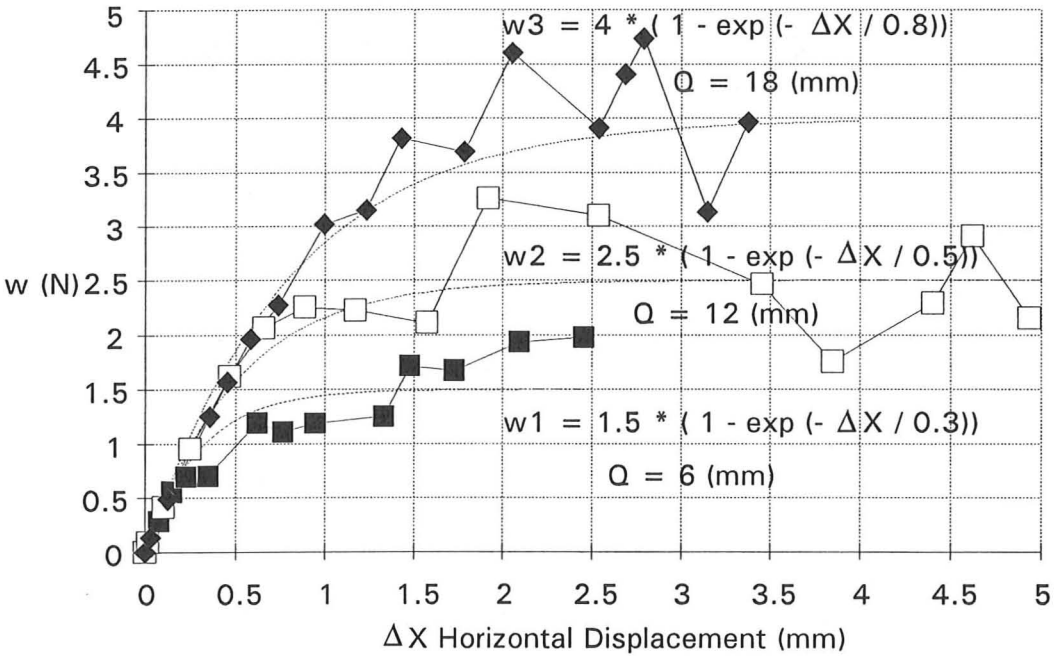


Figure 5.2. The horizontal soil force w N versus the horizontal displacement ΔX mm, measured on a 300 mm bar for Q=6, 12 & 18 mm depth of cover. The soil response is modelled by the three exponential functions w1, w2 & w3.

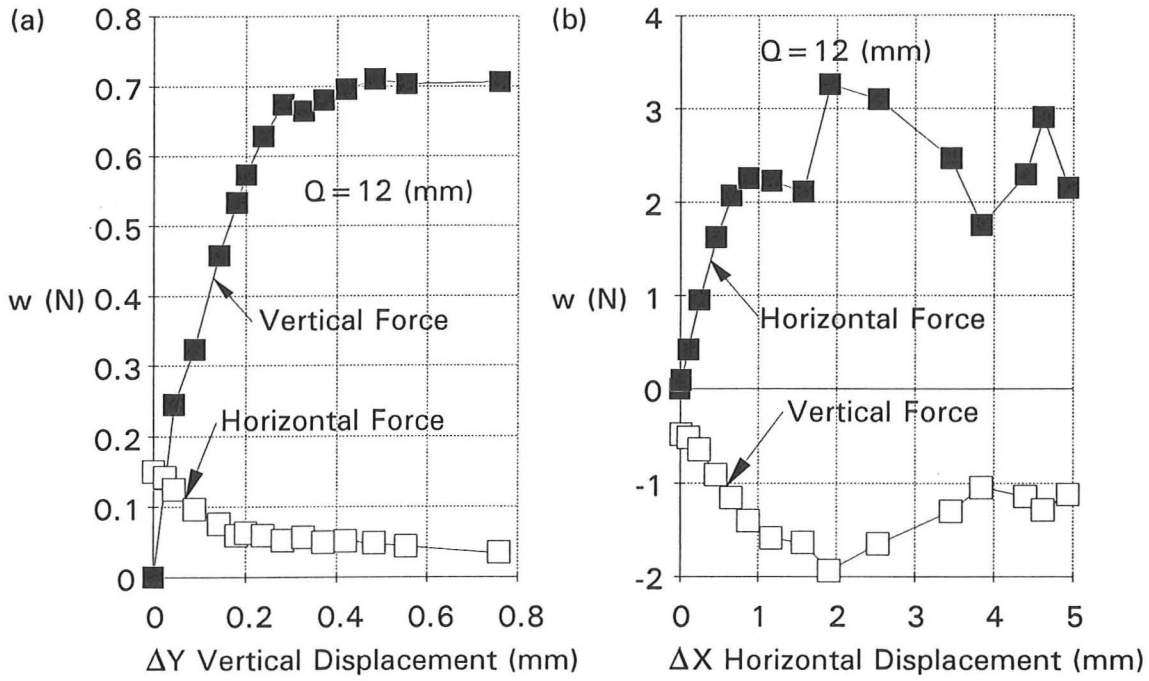


Figure 5.3. The interaction of the horizontal and vertical soil forces, measured on a 300 mm bar for Q=12 mm depth of cover. (a) Vertical displacement and (b) horizontal displacement.

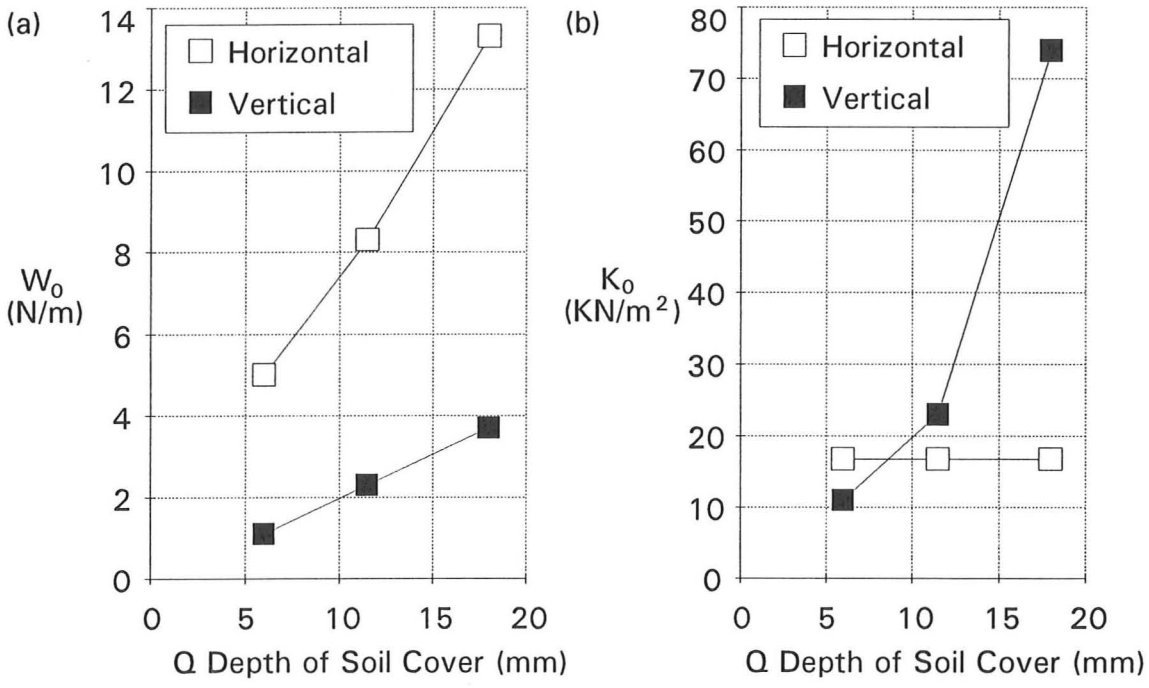


Figure 5.4. The variation of W_0 and K_0 with the depth of soil cover Q. K_0 is the initial slope of the soil response curve, i.e. $K_0 = W_0 / Y_1$ for the vertical response and $K_0 = W_0 / X_1$ for the horizontal response.

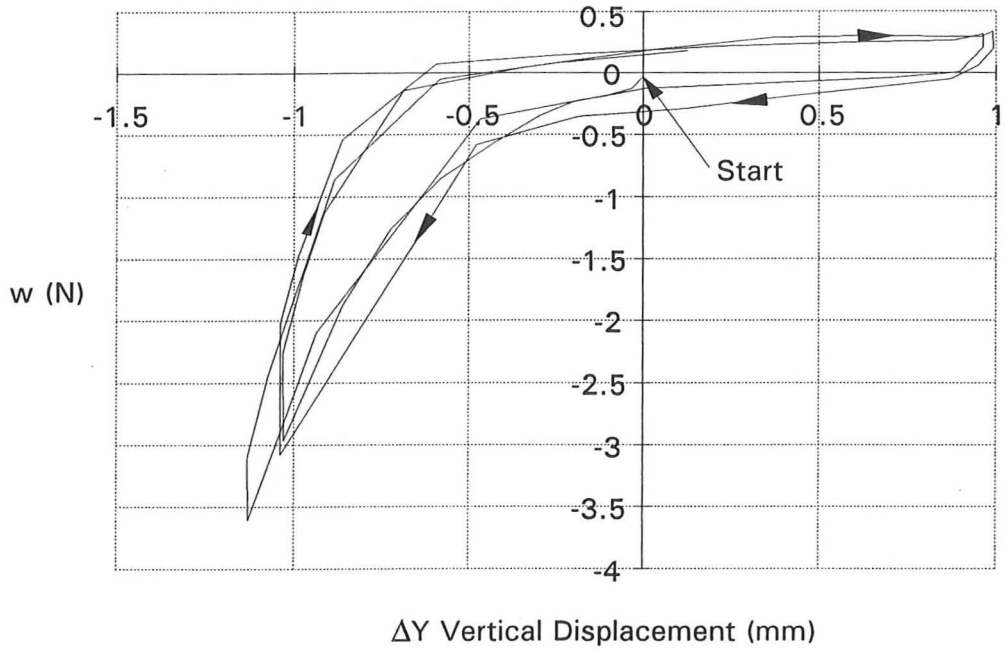


Figure 5.5. The hysteresis of the vertical soil-response. The vertical load w N versus the vertical displacement ΔY mm, as measured on a 300 mm bar. The depth of soil cover Q=6 mm.

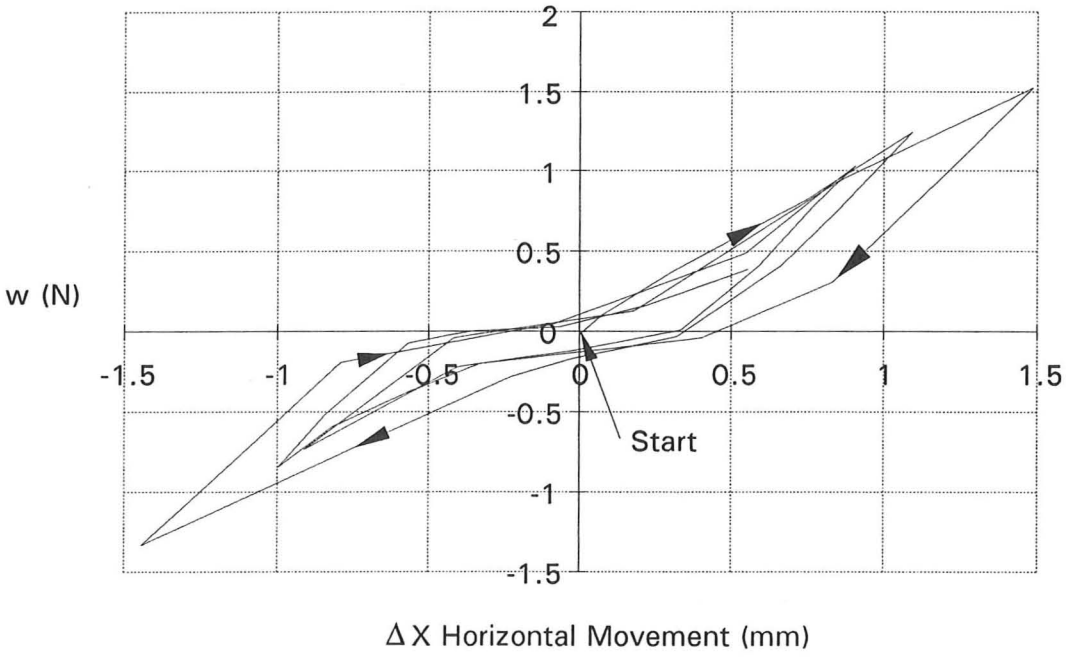


Figure 5.6. The hysteresis of the horizontal soil-response. The horizontal load w N versus the horizontal displacement ΔX mm, measured on a 300 mm bar. The depth of soil cover Q=6 mm.

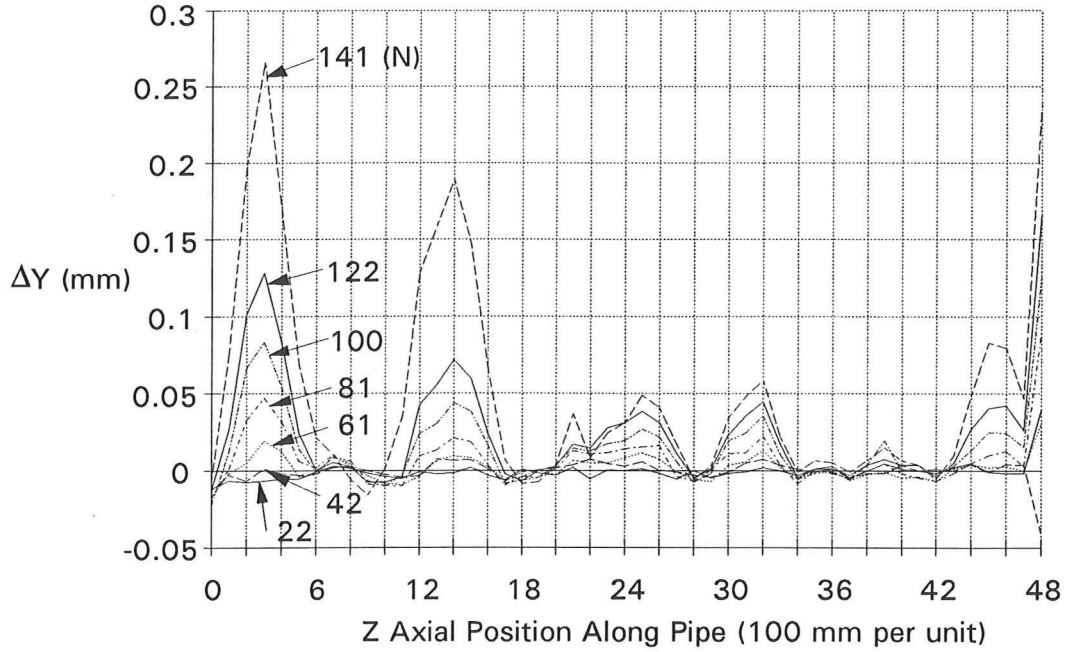


Figure 5.7. The vertical displacement of the pipe for an increasing axial load. The vertical displacement ΔY mm is plotted versus the axial position z (100 mm per unit).

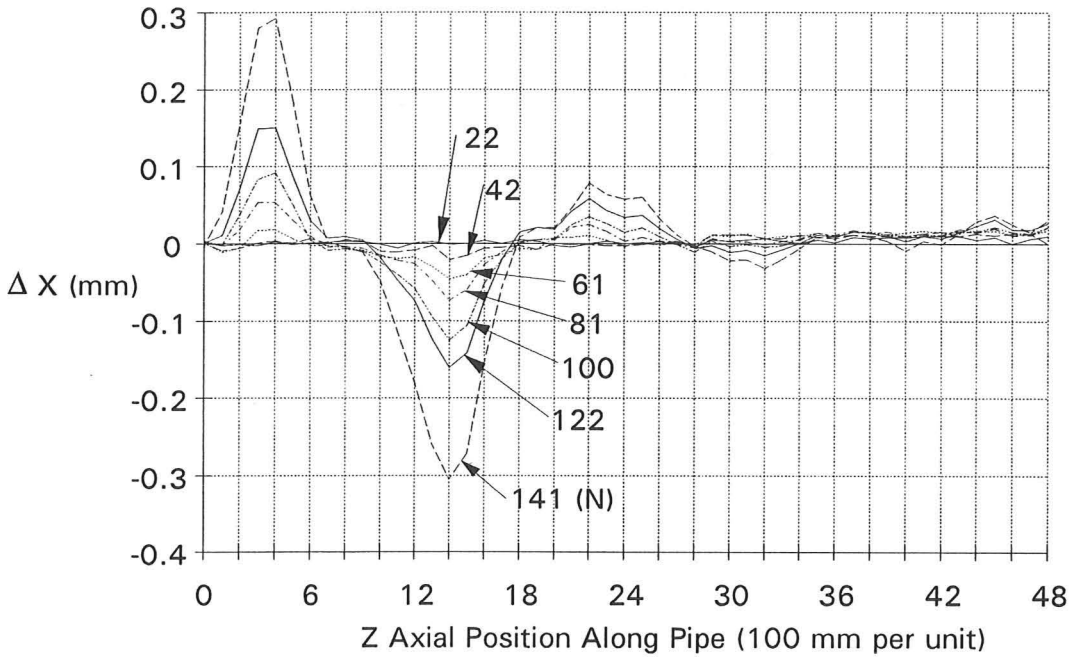


Figure 5.8. The horizontal displacement of the pipe for an increasing axial load. The horizontal displacement ΔX mm is plotted versus the axial position z (100 mm per unit).

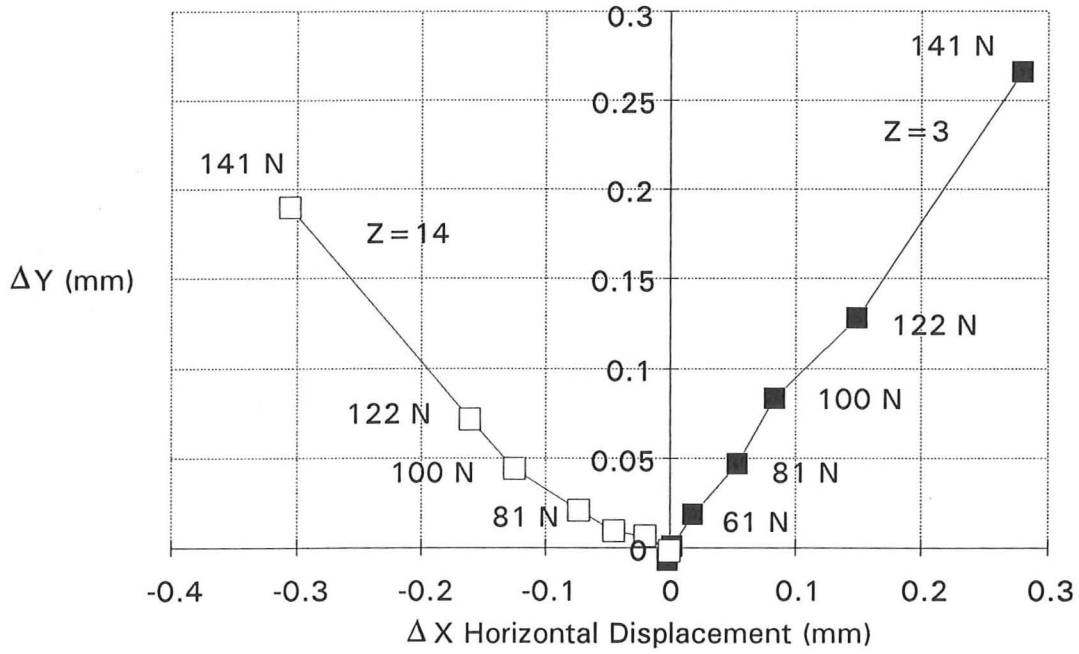


Figure 5.9. A polar plot of the pipe displacement for an increasing axial load. The vertical displacement ΔY mm is plotted versus the horizontal displacement ΔX mm.

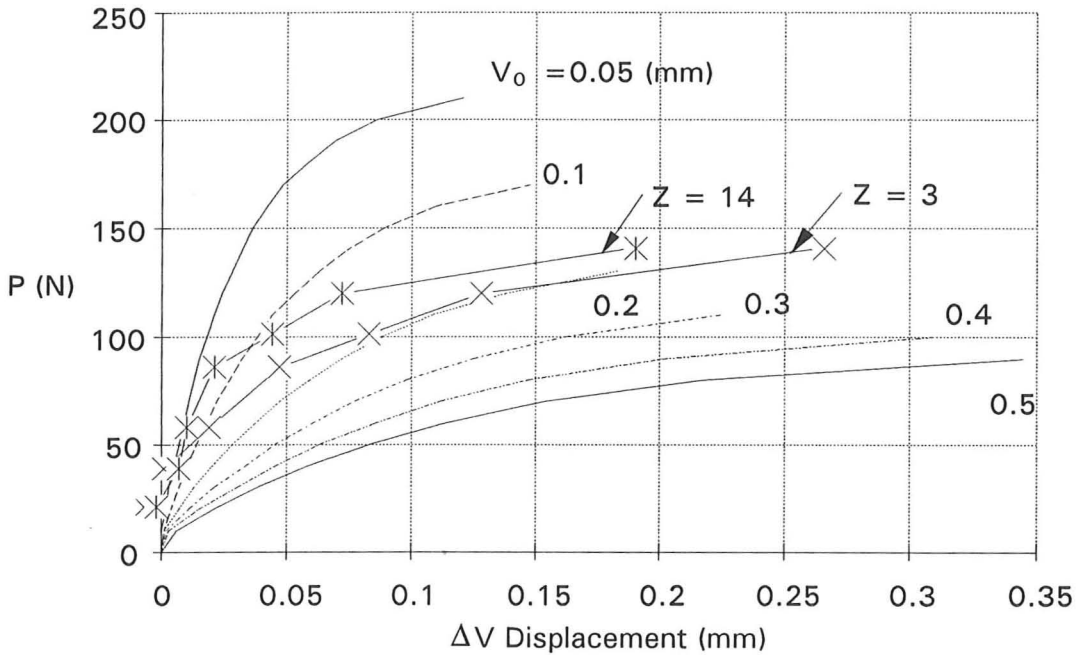


Figure 5.10. A plot of the load versus the displacement for an increasing axial load. Note: ΔV ≡ΔY.

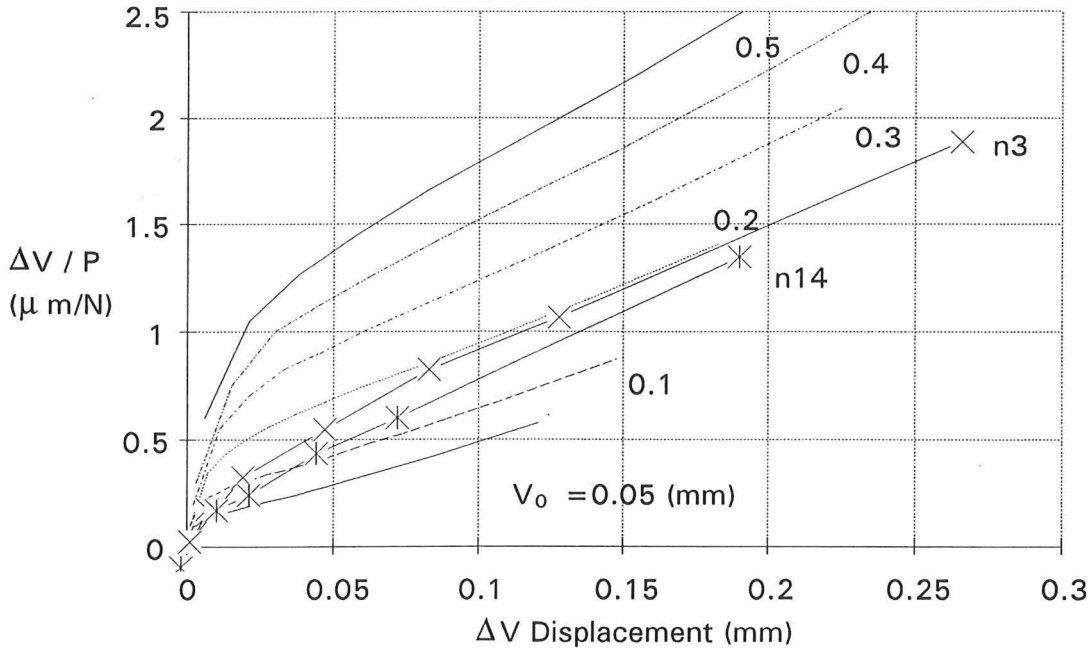


Figure 5.11. A Southwell plot of the pipe displacement for an increasing axial load. Note: $\Delta V \equiv \Delta Y$.

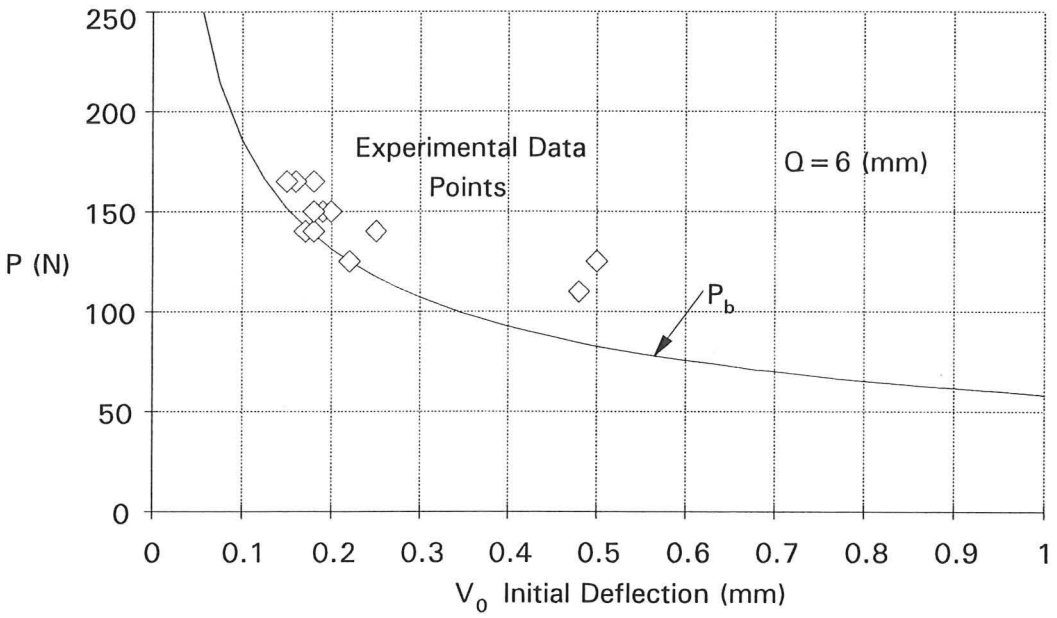


Figure 5.12. A plot of the experimental buckling load P N versus the estimated initial imperfection size V_0 mm for a depth of soil cover Q=6 mm.

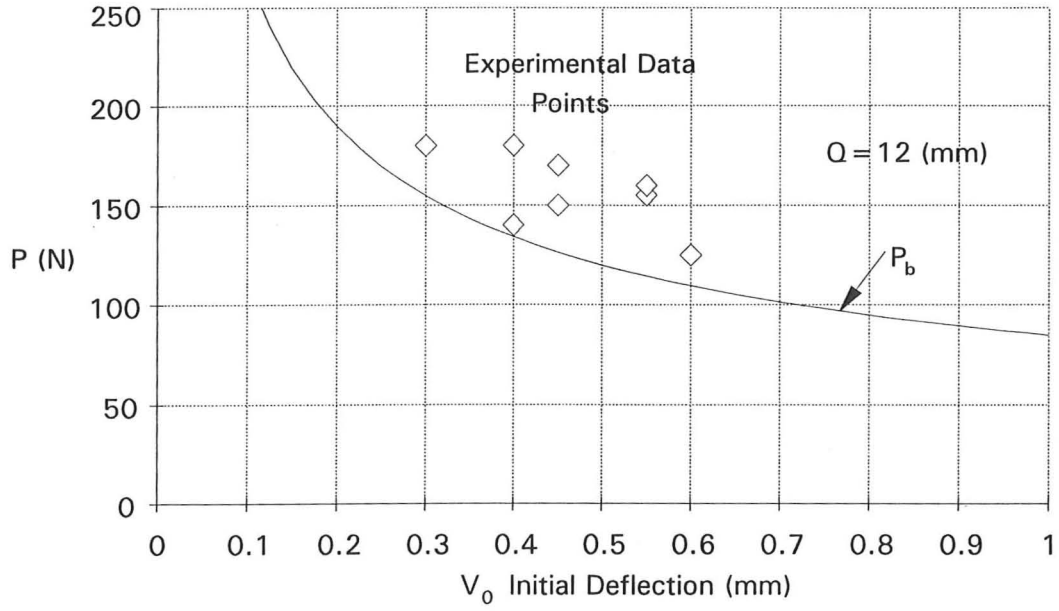


Figure 5.13. A plot of the experimental buckling load P N versus the estimated initial deflection V_0 mm, for a depth of soil cover Q=12 mm.

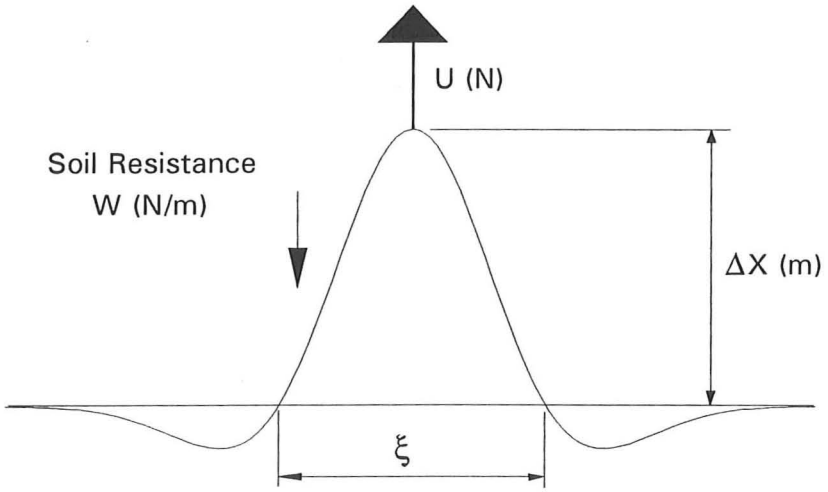


Figure 5.14. A schematic diagram, in plan view, of the application of a horizontal load. Note the single lobe with displacement ΔX m and with a characteristic length ξm.

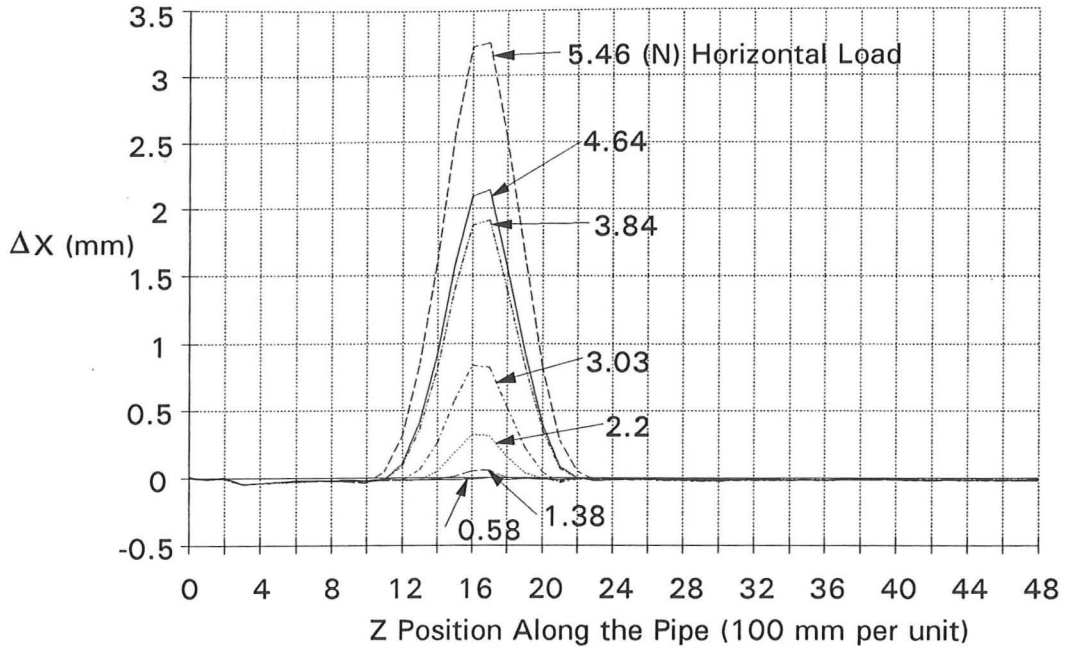


Figure 5.15. The horizontal displacement for an increasing horizontal load.

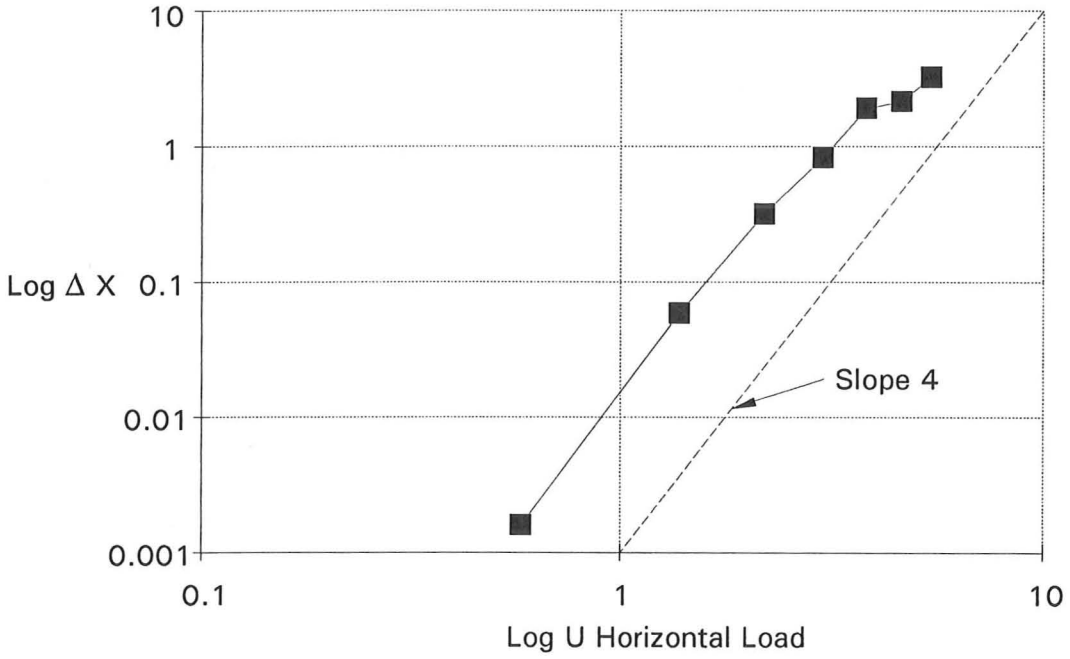


Figure 5.16. The log of the peak horizontal displacement (log ΔX) versus the log of the horizontal load (log U).

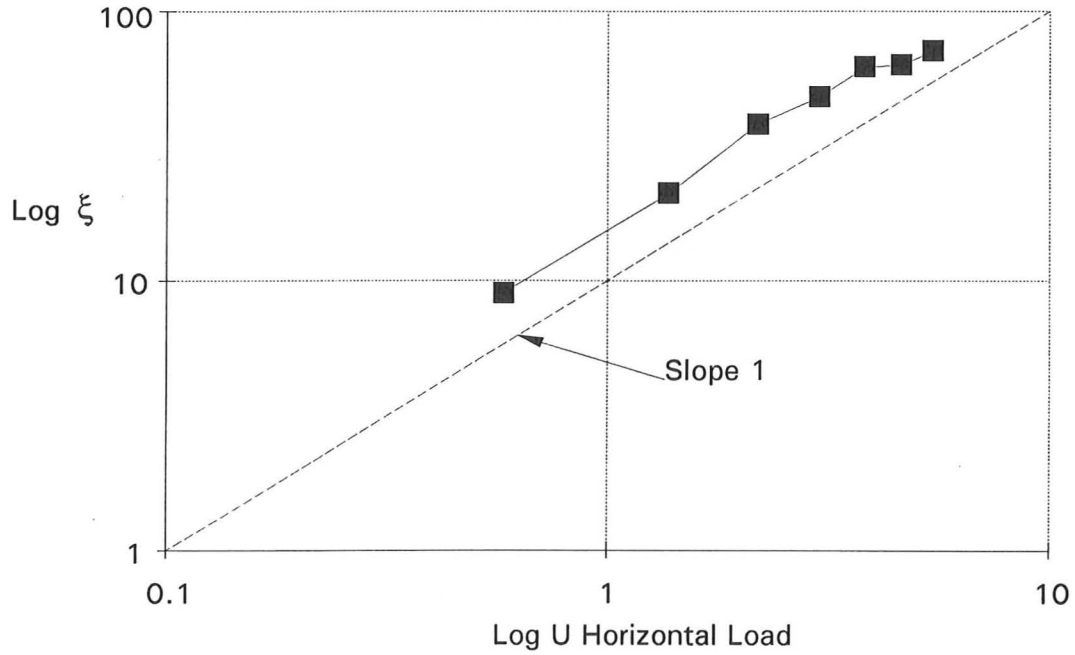


Figure 5.17. The log of the characteristic length (log ξ) versus the log of the horizontal load (log U).

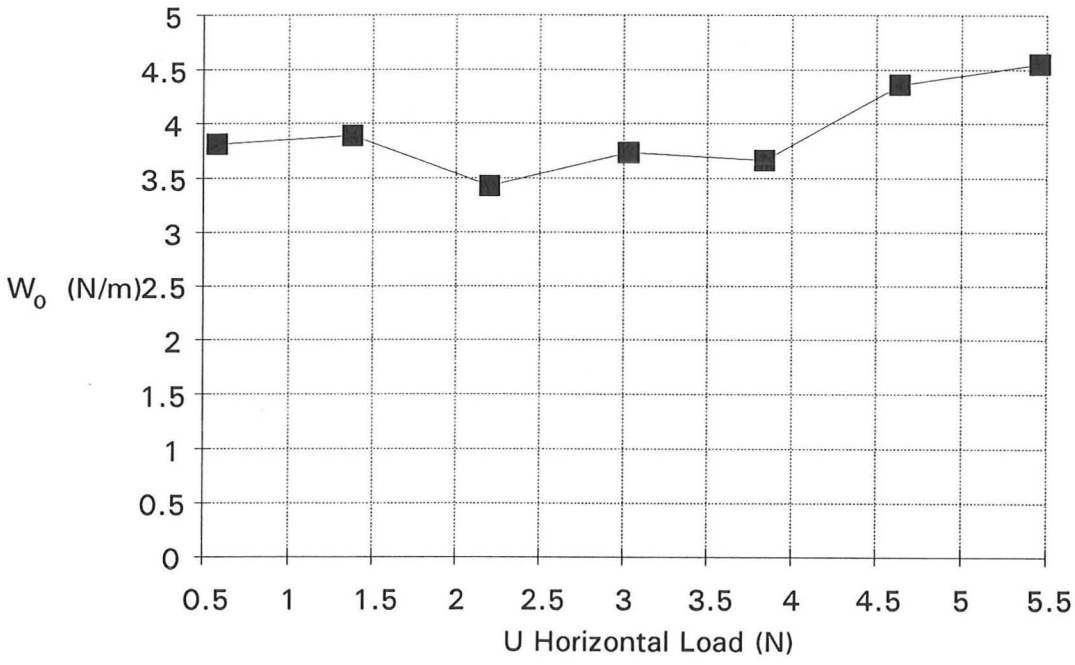


Figure 5.18. The approximate value of W_0, calculated from the horizontal load tests.

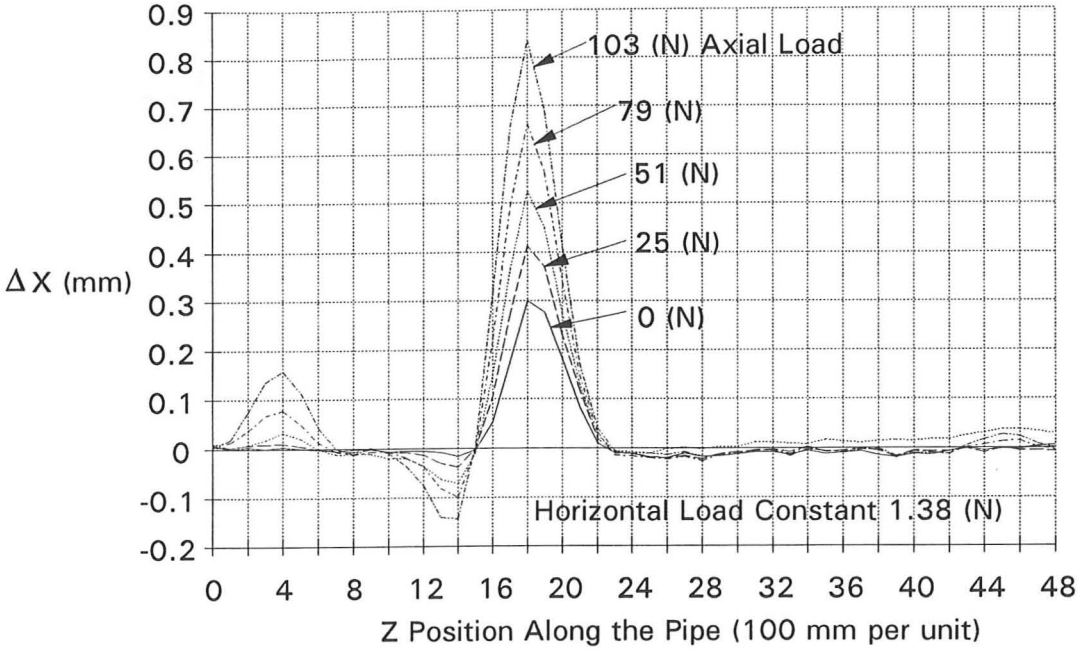


Figure 5.19. The horizontal displacement for a combined horizontal and axial load.

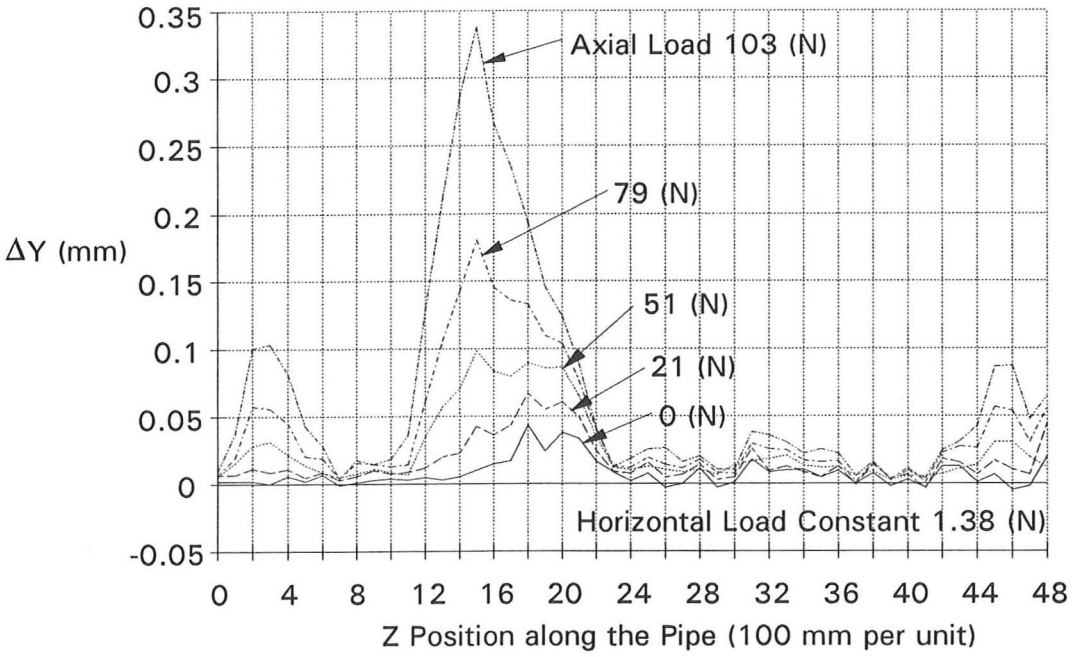


Figure 5.20. The vertical displacement for a combined horizontal and axial load.

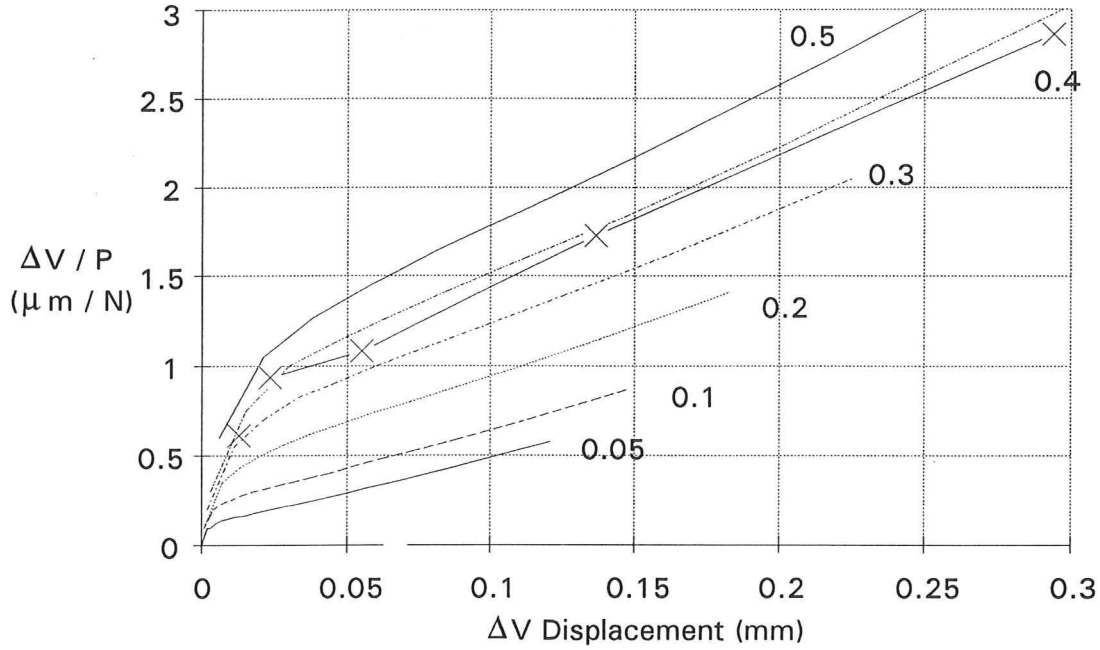


Figure 5.21. A Southwell plot of the vertical displacement due to a combined horizontal and axial load. Note: $\Delta V \equiv \Delta Y$.

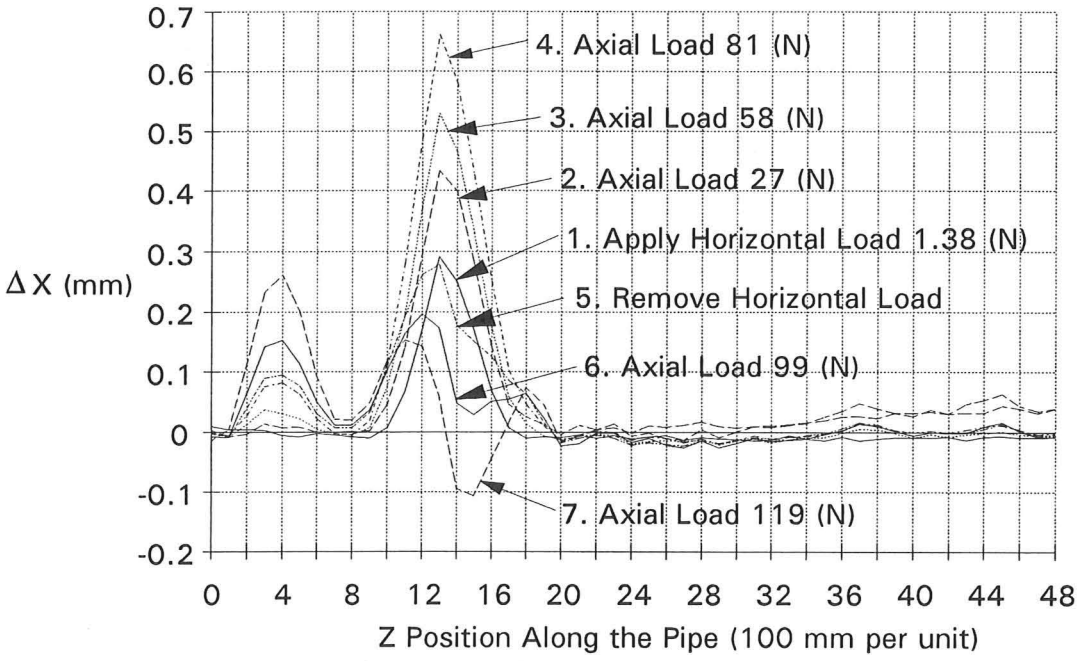


Figure 5.22. The horizontal displacement from adding and removing a horizontal load.

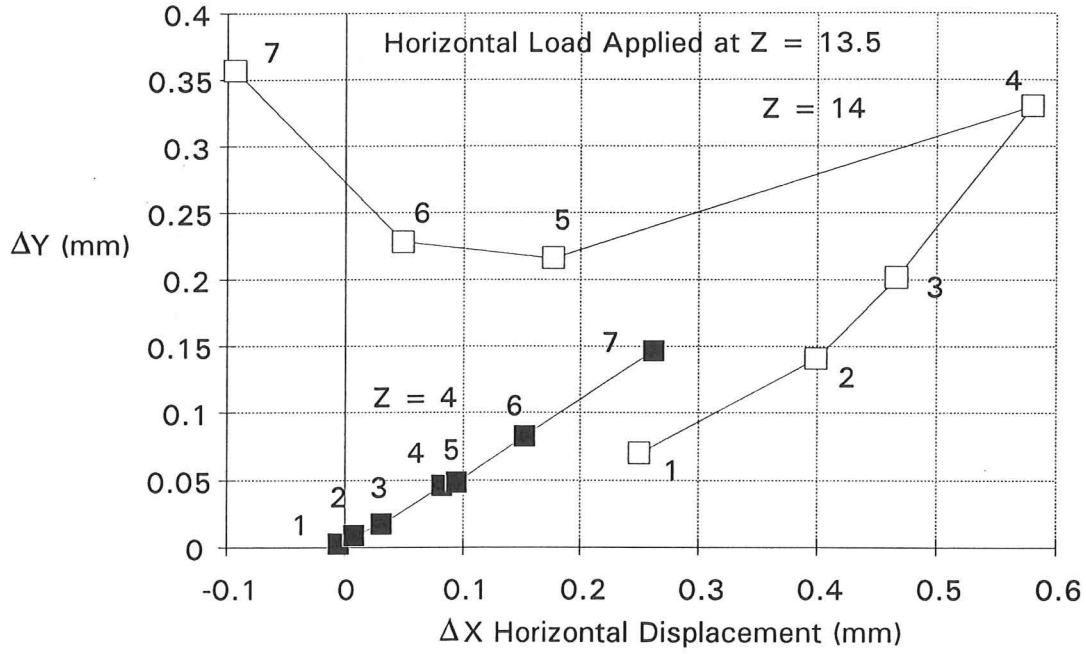


Figure 5.23. A polar plot of the displacement from adding and removing a horizontal load. The displacement of the pipe at positions Z=4 and Z=14 is plotted. The numbered steps correspond to the steps from the previous figure.

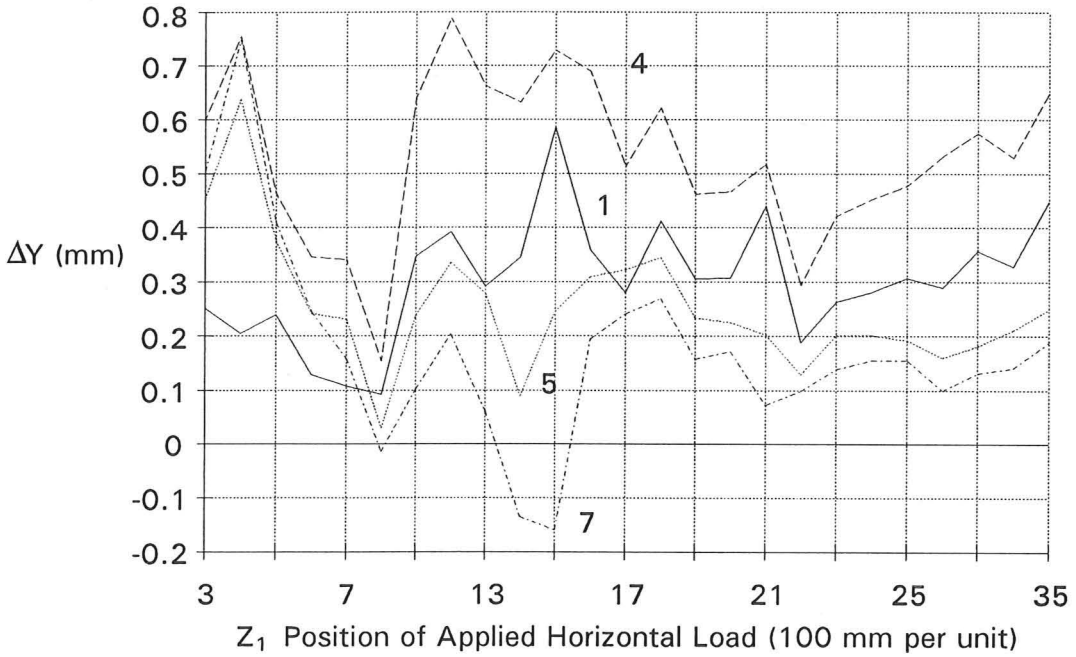


Figure 5.24. The effect of the position of the horizontal load on tests of the preferred wavelength. The position Z_1 is the point of application of the horizontal load. The displacement at Z_1 is plotted versus Z_1, for each of 24 load positions. The step numbers correspond to the steps from the previous 2 figures.

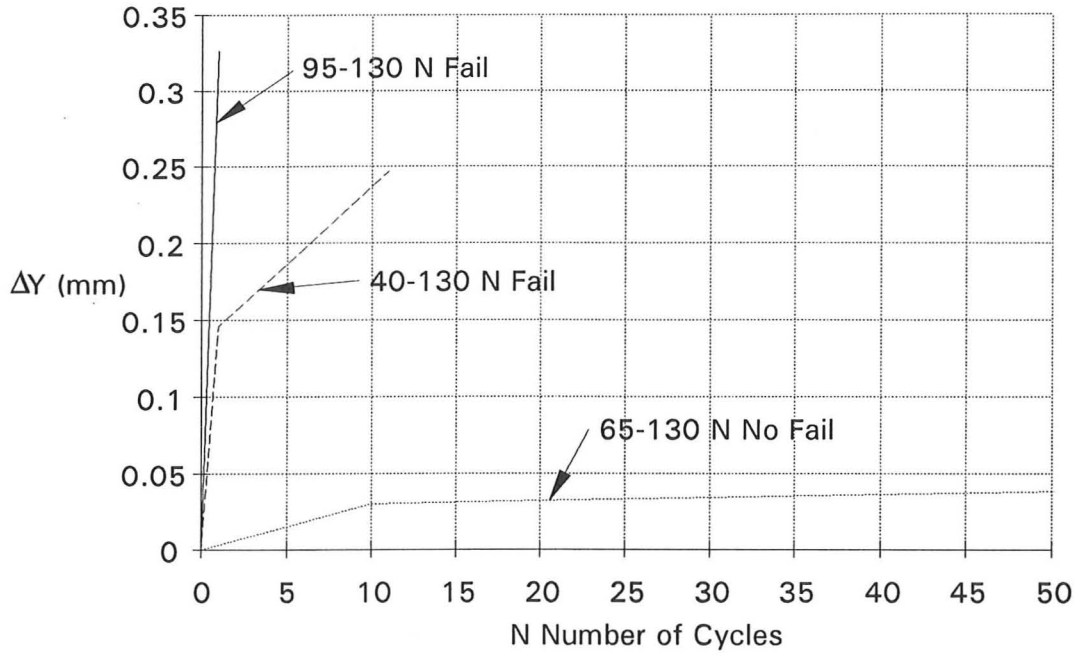


Figure 5.25. The effect of varying the size of the pre-load. The vertical displacement ΔY is plotted versus N the number of cycles for three cyclic loads, 40-130 N, 65-130 N & 95-130 N. Failure occurs if the pipe buckles.

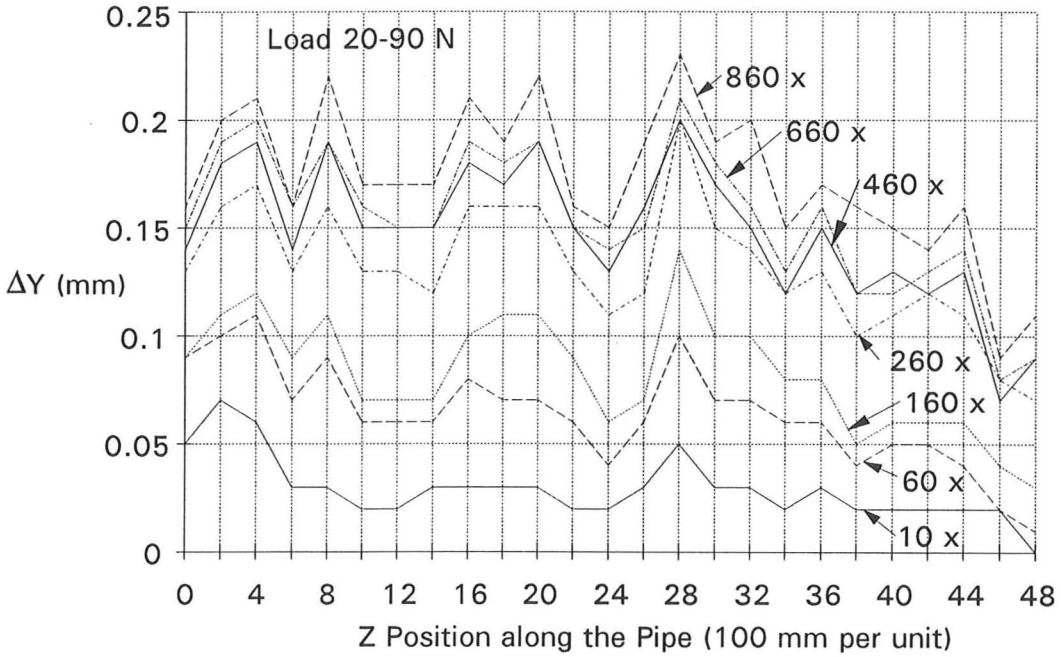


Figure 5.26. The vertical displacement from cycling the axial load. The cumulative number of cycles is marked on the figure.

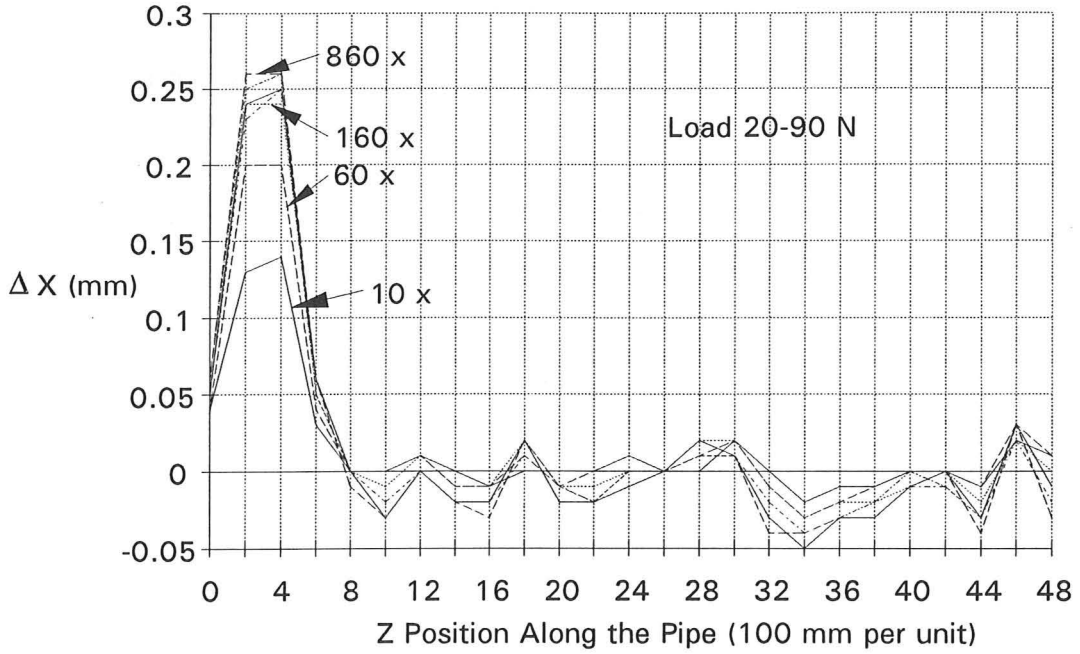


Figure 5.27. The horizontal displacement from cycling the axial load.

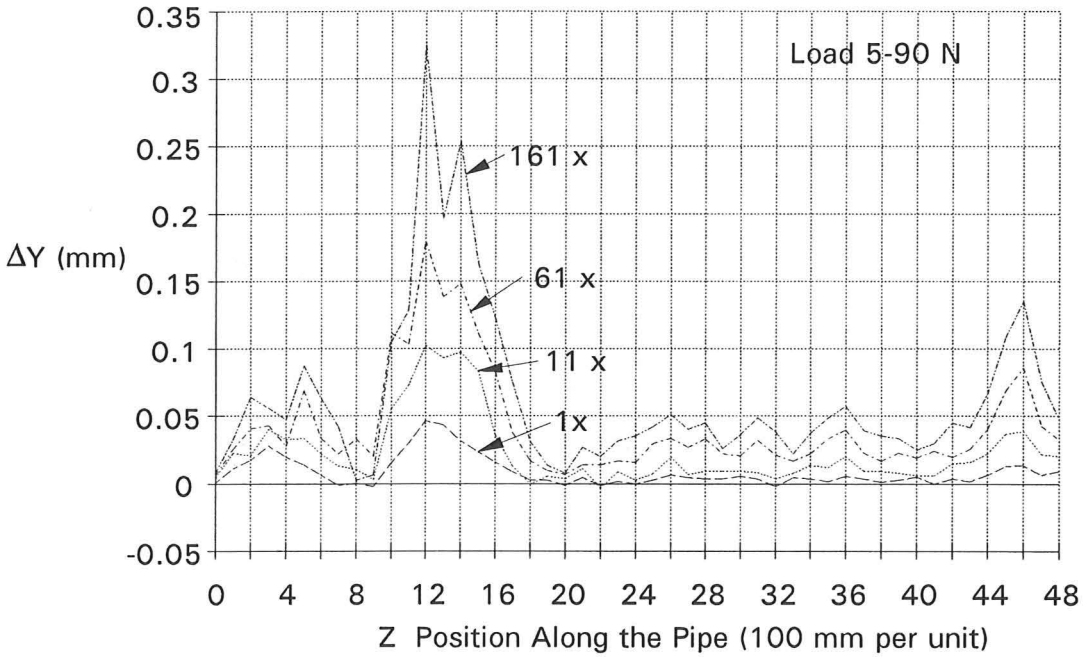


Figure 5.28. The vertical displacement from cycling the axial load. Buckling occurred after 161 cycles.

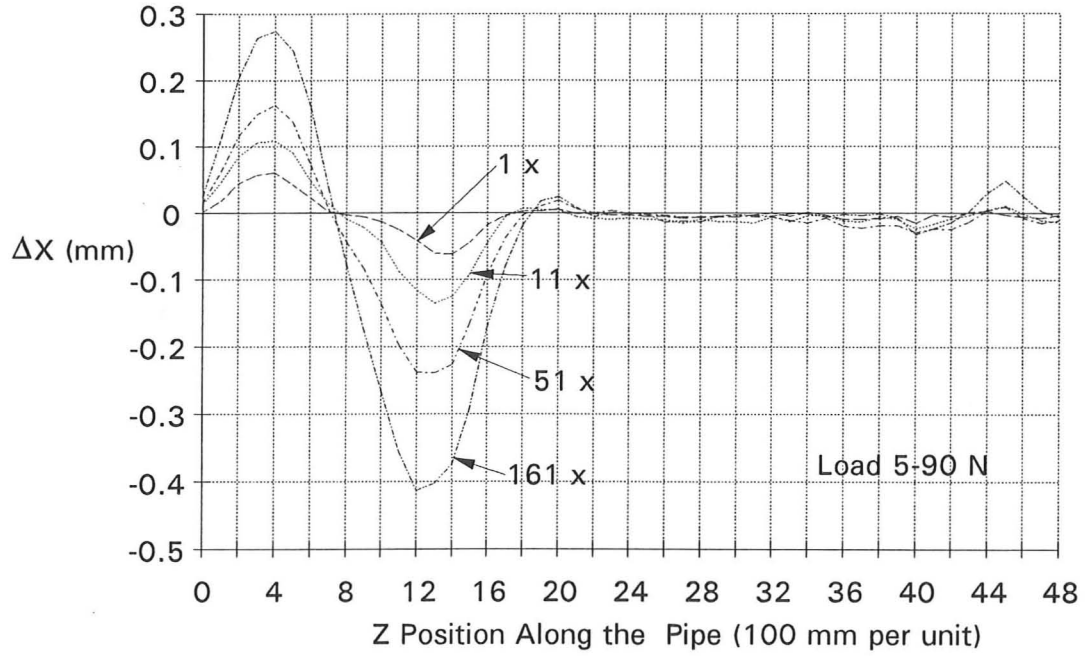


Figure 5.29. The horizontal displacement from cycling the axial load. Buckling occurred after 161 cycles.

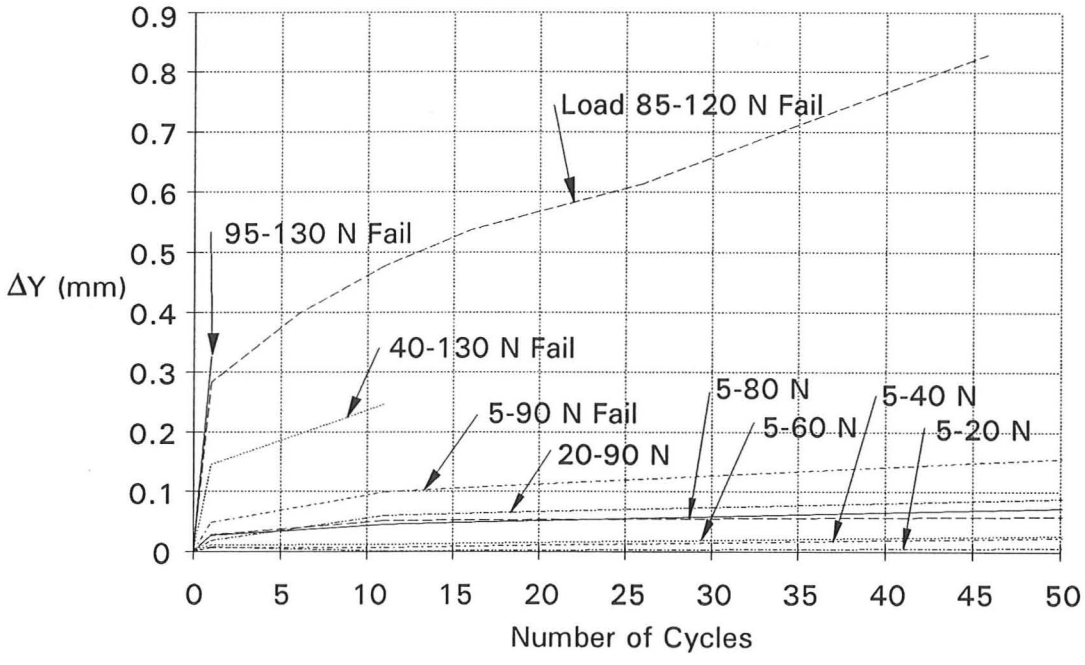


Figure 5.30. The vertical displacement versus the number of cycles. Tests which resulted in buckling failure are marked "Fail".

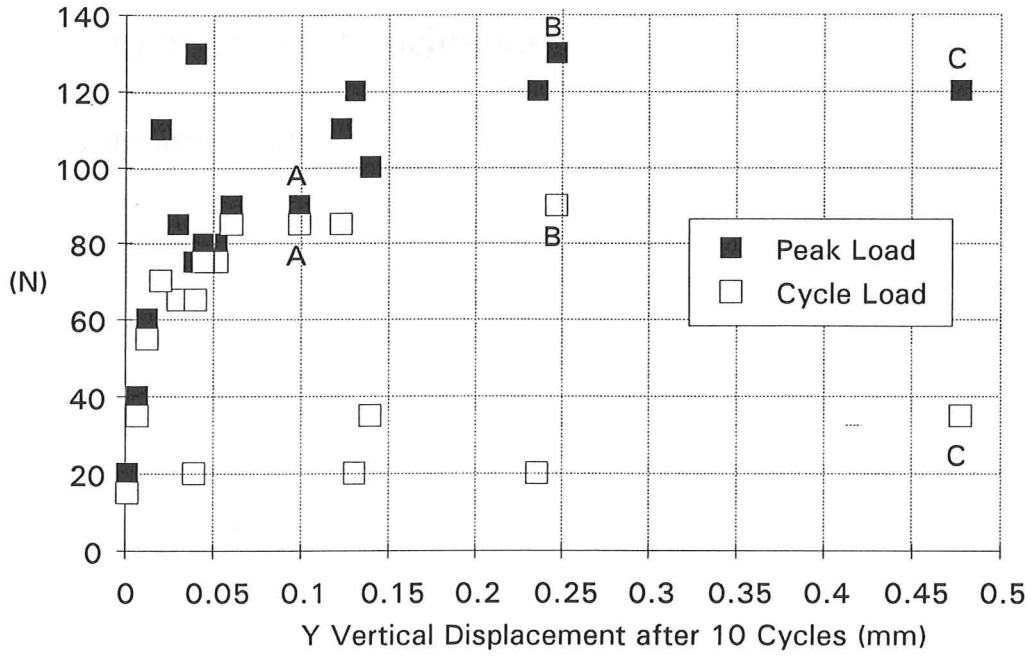


Figure 5.31. The effect of peak load and cycle load. The peak load and the cycle load are plotted versus the displacement after 10 cycles. Tests which buckled are marked; A 5-90 N, B 40-130 N & C 85-120 N.

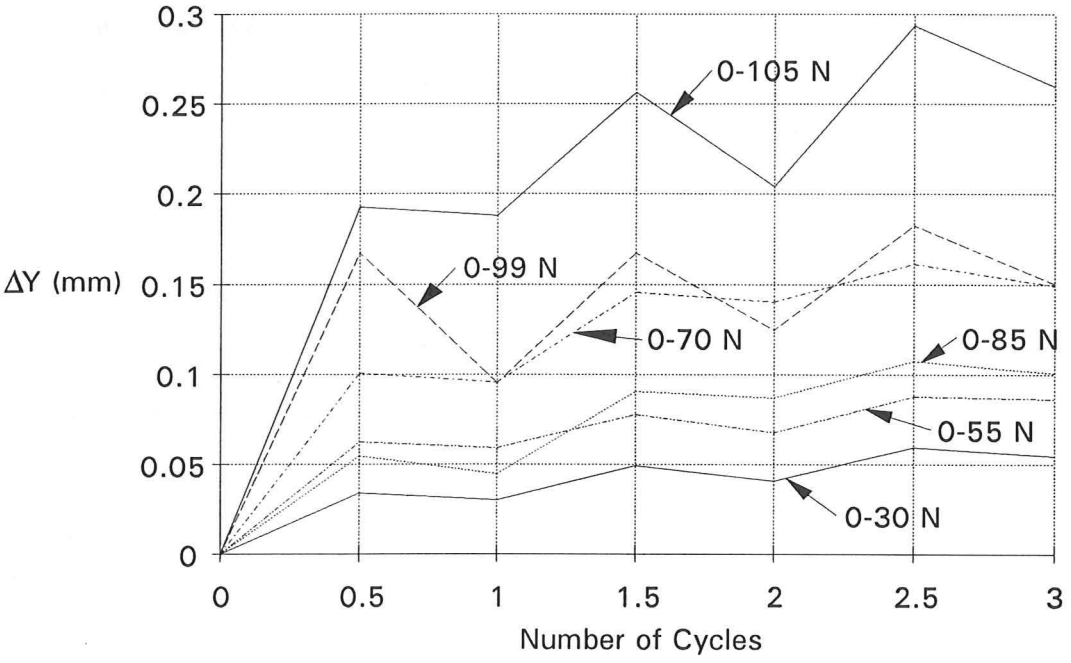


Figure 5.32. The vertical displacement during the load cycle. An end load was applied and removed three times. The depth of soil cover Q=12 mm.

6. Summary and Conclusions

6.1. Literature Survey

Broadly speaking there are two main types of buckling model described in the literature; the rigid-base type of model and the elastic-base type of model. Of these two types the rigid-base model has been the predominant model used to analyse the buckling of both railway tracks and pipelines. The model presupposes that buckling has already occurred and can be used to calculate a safe temperature rise below which, supposedly, buckling cannot occur. The calculated temperature rise turns out to be practically independent of the size of the initial imperfections, but is highly dependent on the value of the axial friction between the pipe and the soil. This type of analysis provides a useful discussion of the post-buckling configuration of the pipeline, but it cannot tell us about the buckling process itself; which we must understand if we are to design pipelines not to buckle.

A more satisfactory model is the modified elastic-base model proposed by Tvergaard and Needleman (1981). This model focuses on the conditions under which buckling occurs, and is used to calculate a safe temperature rise, which is dependent on the size of the initial imperfections and is independent of the axial friction between the pipe and the soil.

Generally, for a single imperfection, thermally induced buckling can only occur if there is a peak in the value of the thermally induced load N_0, with respect to the displacement. However, Tvergaard and Needleman have demonstrated that if multiple imperfections exist on the pipe, a localisation phenomenon can occur; in which case buckling occurs at a peak in the value of the axial load P in the pipe. The difference between the value of P and the value of N_0 is due to the geometric shortening term, and is assumed to be small. Thus, the maximum allowable temperature rise ΔT_{max}, can be calculated by ignoring N_0, and dividing P by $EA\alpha$.

6.2. Theory

A simplified buckling model is presented in Chapter 3. The model is a simplified version of the Tvergaard and Needleman model, and postulates that buckling occurs when the lateral displacement of the pipe reaches the plateau of the soil-response curve. This results in a

simple relationship in which the buckling load and the buckling wavelength are only dependent on the elastic flexural rigidity of the pipe EI N/m^2, the size of the initial imperfection V_0 m and the plateau value of the vertical loading exerted on the pipe by the soil W_0 N/m. The calculated values are not affected by the value of the axial friction between the pipe and the soil, and are virtually independent of the shape of the soil-response curve.

A second model is presented to explain the effect of variations in the wavelength of the initial imperfections. Generally the relationship between the amplitude and the wavelength of imperfections along a pipeline is completely random. However, according to the theory, as summarised above, there is a preferred relationship between the amplitude of an imperfection, and the wavelength at which buckling will occur. This preferred ratio is used to calculate the effective amplitude of an imperfection with an arbitrary wavelength.

A third model is suggested as a method for estimating the amplitude of the initial imperfections on the experimental model pipe. A drawback of the remote-sensing position-measuring system is that it cannot measure the absolute position of the experimental pipe accurately, although it is very sensitive to changes in the position. Consequently, the amplitude of the initial imperfections of the pipeline cannot be measured directly, but must be estimated from the experimental data. This has been done by comparing a Southwell plot of the experimental data with a Southwell plot of data taken from a numerical analysis.

6.3. Experimental Results

6.3.1. The Soil-Response

An important feature of the buckling process is the force exerted on the pipe by the soil, due to movement of the pipe. In these experiments the soil used was a dry, cohesionless, granular material with particles of a single uniform shape and size. The force-displacement characteristics of the pipe and soil, have been measured in two ways:

(i) Directly, by moving a 300 mm length of bar and measuring the forces exerted on the bar.

(ii) Indirectly, by measuring the sideways displacement of the pipe due to a sideways load, without axial loading.

A graph of the force exerted on the 300 mm bar by the soil shows a gently rising curve which reaches a relatively constant plateau value W_0 at large displacements; the value of W_0 for both horizontal and vertical displacement, increases with increasing depth of soil cover. The relationship matches the form expected for a loose-packed granular soil, as described in the literature. However, the measured plateau value of the soil force is somewhat higher than the calculated value from equation (2.15). This is possibly due to an arching effect between the soil grains. The individual grains of the "soil" used in the experimental rig are large in proportion to the pipe diameter. Consequently the behaviour of the test soil may not be representative of actual soils.

The results from the indirect tests showed a calculated value of the horizontal plateau load which was in reasonable agreement with the direct tests.

6.3.2. Axial loading

The test results show that the pipeline forms both vertical and horizontal lobes which grow in magnitude as the axial load is increased, and that at some critical point buckling occurs. This type of behaviour agrees best with the Tvergaard & Needleman type of model; the lobes being assumed to form at the locations of the initial imperfections. By comparison the rigid-base type of model is less satisfactory as it doesn't consider the growth of the initial imperfections; in that in this type of analysis, the buckle is assumed to have somehow already formed.

The amplitude of the initial imperfections on the test pipe has been estimated by means of a Southwell plot, as described in Chapter 3. The measured buckling loads are in reasonable agreement with the simplified buckling model described in Chapter 3. The theoretical buckling loads fit the test data reasonably well, providing a useful lower bound to the data points. This conclusion, is however, dependent on the accuracy of the method used to estimate the amplitude of the initial imperfections. Further experiments are suggested to verify these results.

The expression for the buckling load, equation (3.7) from the simplified buckling model, can be re-arranged, and by substituting for I, A and $P_{b,,}$ gives the following expression for the maximum temperature rise ΔT_{max}:

$$\Delta T_{max} = \frac{0.2}{\alpha}\sqrt{\frac{DW_0}{tEV_0}} \qquad (6.1)$$

Here, α $^oC^{-1}$ is the coefficient of linear, thermal expansion, D m is the diameter of the pipe, W_0 N/m is the plateau value of the downward force exerted by the soil on the pipe, t m is the thickness of the pipe wall, E N/m^2 is Young's Modulus, and V_0 m is the amplitude of the initial imperfection.

In general, the aim of the engineer is to prevent buckling of a pipeline whose design has been arrived at previously. The material parameters α and E are fixed by the selection of the pipe material. (usually steel) Similarly, the pipe diameter and the wall thickness are dictated by the desired flow rate and the operating pressure. In practice therefore, the only parameters which can be varied in terms of the buckling design are the initial crookedness of the pipe V_0, and the plateau value of the soil-response W_0. Thus to increase the value of the maximum temperature rise ΔT_{max}, either V_0 should be reduced or W_0 should be increased.

6.3.3. Combined Horizontal and Axial Loading

The combined horizontal and axial load tests were performed in order to investigate the effect of a "preferred" buckling wavelengths. It can be seen from the series of axial load tests that there is a strong preference displayed by the pipe for a particular displacement configuration; a similar configuration being observed for each test in the series. This observation is also supported by the simplified buckling model, which suggests that there is a simple relationship between the buckling load, the buckling wavelength and the amplitude of the initial imperfection. This observation is further supported by the combined loading tests. The tests show that the pipe has a marked "preference" for a particular configuration; regarding both the wavelength and direction of the lobes.

6.3.4. Cyclic Loading

The experiments show that in general, two distinct types of pipe displacement can occur. One type involves a general lateral displacement of the entire length of the pipe. The

displacement reaches a plateau value as the number of cycles increases, generally without buckling occurring.

In the second type of displacement, a number of individual lobes are formed on the pipeline, and these lobes continue to grow until buckling occurs at some critical value of the load and displacement.

It appears from the limited, available, experimental data, that provided the magnitude of the displacement due to the first cycling of the axial load is less than approximately half the proportional limit of the soil, then buckling would not occur. Thus the maximum allowable displacement ΔV_{max} can be specified as a fraction of the proportional limit. The soil response can be regarded as being linear for small displacements, and the maximum allowable axial load P_{max} can then be calculated from equation (5.10). The maximum temperature rise ΔT_{max} is calculated by dividing P_{max} by $EA\alpha$.

A further series of tests were performed to measure the movement of the pipe during the axial cycles. These tests demonstrated that the response of the test soil was markedly non-elastic, even for small displacements. When the load is cycled, even after only small displacements, the pipe does not return to its original position when the load is released. We had initially assumed that the soil response was elastic over the linear portion of the response curve and that the displacement would have a significant elastic component. However, this is not the case and although the response can be approximated as being linear for small displacements it must be regarded as being essentially linear-inelastic.

We would expect that the imperfection lobes would continue to grow at an increasing rate, as the axial load is cycled. However, this is not the case. The displacement tends to level off, and provided that buckling does not occur first, it reaches a static plateau value. Thus it appears that there is some factor which is limiting the growth of the lobes. This could be; residual forces in the soil which are acting on the pipe, an effect caused by the increasing curvature of the pipe. or the increasing geometric shortening effect as the amplitude increases.

6.4. Further Research

Although these experiments have provided a useful insight into the nature of the buckling process, there are a number of areas where the experimental apparatus should be modified or improved.

An obvious shortcoming of the experiments which were performed was the inability of the apparatus to measure the amplitude of the initial imperfections on the pipe. Although the amplitudes were estimated, the accuracy of the method used is unknown. It is therefore difficult to verify the validity of the simplified buckling model or in fact to make proper measurements of the effect of the imperfection size.

Further experiments are therefore suggested with a modified apparatus, so that the size of the initial imperfections can be carefully controlled and measured. An end-load is an unsatisfactory method of applying the axial load, because of the variation of the load along the pipe. It is suggested that either the hydraulic system be improved, or a thermal heating system is used; so that a larger axial load can be applied uniformly along the entire length of the pipe. Strain gauges should also be fitted at points along its length in order to determine the distribution of the axial load.

It would be useful to experiment with different types of test soil; cohesive soils, tightly packed soils, soils with different densities, soils with different sized particles, and soils with a range of particle sizes, etc. A single soil type was used in these experiments because of the limitations imposed by the remote-sensing, position-measuring system. As an alternative to using different test soils, it may be possible to modify the behaviour of the existing test soil by some artificial means, such as the application of a vacuum. Weights could also be added to the pipeline to increase the value of W_0.

7. Bibliography

Allan, T. 1968 One-way buckling of a compressed strip under lateral loading. *Journal of Mechanical Engineering Science.* **10**, 175-181.

Baldry, J.A.S. 1973 *The buckling of axially loaded buried pipelines*, M.S. thesis, Cambridge University, p 30-.

Ballet, J.P. & Hobbs, R.E. 1992 Assymetric effects of prop imperfections on the upheaval buckling of pipelines. Draft copy

Bastiaanse, T. & Liles, J.R. 1983 Overview of the central Cormorant underwater manifold centre project (1974-1983). *Proceedings, 1983 Offshore Technology Conference,* Paper No. **OTC** 4607.

Boer, S., Hulsbergen, C.H., Richards, D.M., Klock, A. & Biaggi, J.P. 1986 Buckling considerations in the design of the gravel cover for a high-temperature oil line. *Proceedings, 1986 Offshore Technology Conference,* Paper No. **OTC** 5294.

Costello, G.J., Brink, F.I.A. & Henery, D. 1983 Insulated pipelines between the underwater manifold centre and Cormorant 'A' platform in the Northern North Sea. *Proceedings, 1983 Offshore Technology Conference,* Paper No. **OTC** 4611.

Craig, I.G., Nash, N.W. & Oldfield, G.A. 1990 Upheaval buckling: A practical solution using hot water flushing technique. *Proceedings, 1990 Offshore Technology Conference,* Paper No. **OTC** 6334.

Di Tella, V., Minach, G. & Vielmo, P. 1981 TM 402 - A new operating cable and pipe burying system. *Proceedings, 1981 Offshore Technology Conference,* Paper No. **OTC** 3983.

El-Aini, Y.M. 1976 Effect of foundation stiffness on track buckling. **ASCE** *Journal of Engineering Mechanics,* **102**, No. EM3, 531-545.

Ellinas, C.P., Supple, W.J. & Vastenholt, H. 1990 Prevention of upheaval buckling of hot submarine pipelines by means of intermittent rock-dumping. *Proceedings, 1990 Offshore Technology Conference,* Paper No. **OTC** 6332.

Guijt, J. 1990 Upheaval buckling of offshore pipelines: Overview and introduction. *Proceedings, 1990 Offshore Technology Conference,* Paper No. **OTC** 6487.

Heténi, M. 1946 *Beams on elastic foundation,* 1st ed., p. 127. Ann Arbor: The University of Michigan Press.

Hobbs, R.E. 1979 The lifting of pipelines for repair or modification. *Proceedings, Institution of Civil Engineers,* Part 2, **67**, 1003-1013.

Hobbs, R.E. 1980 The effect of soil modulus on pipeline stresses. **ASCE** *Journal of Transportation Engineering,* **106,** No TE6, 775-786.

Hobbs, R.E. 1981 Pipeline buckling caused by axial loads. *Journal of Constructional Steel Research,* **1**, No. 2, 2-10.

Hobbs, R.E. 1984 In-service buckling of heated pipelines. **ASCE** *Journal of Transportation Engineering,* **110**, No. TE2, 175-89.

Hobbs, R.E. 1989 Two-dimensional upheaval buckling of a heavy sheet. *Thin-walled structures,* **8**, 235-252.

Hobbs, R.E., Liang, F. 1989 Thermal buckling of pipelines close to restraints. *Proceedings, Eighth International Offshore Mechanics and Arctic Engineering Conference,* Paper No. **OMAE** -89-812.

James, M.L., Smith, G.M. & Wolford, J.C. 1985 *Applied numerical methods for digital computation,* 3rd ed, p. 397. New York: Harper and Row.

Ju, G.T., Kyriakides, S. 1988 Thermal Buckling of Offshore Pipelines. *Journal Offshore Mechanics and Artic Engineering,* **110**, 355-364.

Kerr, A.D. 1974 On the stability of the railroad track in the vertical plane. *Rail International,* **5**, 131-142.

Kerr, A.D. 1979 On thermal buckling of straight railroad tracks and the effect of track length on the track response. *Rail International,* **9**, 759-768.

Kerr, A.D. & El-Aini, Y.M. 1978 Determination of admissible temperature increases to prevent vertical track buckling, **ASME** *Journal of Applied Mechanics.* **45**, 565-573.

Kimura, T., Idogaki, S., Takada, K. & Fujita, Y. 1980 Experimental and analytical studies of the elastoplastic behaviour of offshore pipelines during laying. *Proceedings, 1980 Offshore Technology Conference,* Paper No. **OTC** 3737.

Klever, F.J., van Helvoirt, L.C., Sluyterman, A.C. 1990 A dedicated finite-element model for analysing upheaval buckling response of submarine pipelines. *Proceedings Offshore Technology Conference,* Paper No. **OTC** 6333.

Luscher, U., Thomas, H.P. & Maple, J.A. 1979 Pipe-soil interaction, Trans-Alaska pipeline. *Proceedings ASCE Pipeline Division Specialty Conference,* p 486-502.

Martinet, M.A. 1936 Flambement des voies sans joints sur ballast et rails de grand longueur. *Revue Générale des Chemins de Fer,* **55**, No. 2, 212-230.

Mousselli, A.H. 1977 Pipe stresses at the seabed during installation and trenching operations, *Proceedings, 1977 Offshore Technology Conference,* Paper No. **OTC** 2965.

Nielsen, N.J.R.,Lyngberg, B.S., & Pedersen, P. T. 1990 Upheaval buckling failures of insulated buried pipelines - case stories. *Proceedings, 1990 Offshore Technology Conference,* Paper No. **OTC** 6488.

Nielsen, N.J.R., Pedersen, P. T., Grundy, A.K., & Lyngberg, B.S. 1988 New design criteria for upheaval creep of buried sub-sea pipelines. *Proceedings, 1988 Offshore Mechanics and Artic Engineering Conference,* Paper No. **OMAE** 88-861, vol V, 243-249.

Ochtman, J.A. & den Boer, A.S. 1980 Post plowing for rigid lines - controlled trench depth and high progress rate. *Proceedings, 1980 Offshore Technology Conference,* Paper No. **OTC** 3738.

Palmer, A.C. 1976 *Structural Mechanics,*1st ed., p. 111. Oxford: Clarendon Press.

Palmer, A.C. & Baldry, J.A.S. 1974 Lateral buckling of axially-compressed pipelines. *Journal of Petroleum Technology,* **26**, 1283-1284.

Palmer, A.C., Ellinas, C.P., Richards, D.M., & Guijt, J. 1990 Design of submarine pipelines against upheaval buckling. *Proceedings, 1990 Offshore Technology Conference,* Paper No. **OTC** 6335.

Pedersen, P. T., Jensen, J.J. 1988 Upheaval creep of buried heated pipelines with initial imperfections. *Marine Structures,* **1**, 11-22.

Pedersen, P. T., Michelsen, J. 1988 Large deflection upheaval buckling of marine pipelines. **DCAMM** Rep. No. 370, The Technical University of Denmark, Mar. 1988.

Putot, C.J.M. 1989 Localised buckling of buried flexible pipelines. *Proceedings, 1989 Offshore Technology Conference,* Paper No. **OTC** 6155.

Richards, D.M. 1990. The effect of imperfection shape on upheaval buckling behaviour. Lloyds Register, London.

Richards, D.M. & Andronicou, A. 1986 Seabed irregularity effects on the buckling of heated submarine pipelines, *Holland Offshore 86, Amsterdam, Advances in Offshore Technology, 1986,* Paper No

Schaminée, P.E.L., Zorn, N.F. & Schotman G.J.M. 1990 Soil response for pipeline upheaval buckling analyses: Full-scale laboratory tests and modelling. *Proceedings, 1990 Offshore Technology Conference,* Paper No. **OTC** 6486.

Taylor, N. & Gan, A.B. 1986 Submarine pipeline buckling - imperfection studies. *Thin-walled Structures,* **4**, 295-323.

Taylor, N., Richardson, D. & Ben Gan, A. 1985 On submarine pipeline frictional characteristics in the presence of buckling. *Proceedings, Fourth International Offshore Mechanics and Artic Engineering Conference,* **1,** 508-515.

Trautmann, C.H., O'Rourke, T.D. & Kulhawy, F.H. 1985_a Uplift force - displacement response of buried pipe. **ASCE** *Journal of Geotechnical Engineering,* **111**, No. 9, 1061-1076.

Trautmann, C.H., O'Rourke, T.D. & Kulhawy, F.H. 1985_b Lateral force - displacement response of buried pipe. **ASCE** *Journal of Geotechnical Engineering,* **111**, No. 9, 1077-1092.

Tvergaard, V. & Needleman, A. 1981 On localised thermal track buckling. *International Journal of Mechanical Sciences,* **23,** 577-587

Yen, B.C., Tsao, C.H. & Hinkle, R.D. 1981 Soil-pipe interaction of heated oil pipelines. **ASCE** *Journal of Transportation Engineering,* **107,** No. TE1, 1-14.

Yun, H. & Kyriakydes, S. 1985 Model for beam-mode buckling of buried pipelines. **ASCE** Journal of Engineering Mechanics, **111**, No. 2,235-253.

A.1 The Experimental Apparatus

A.1.1 Details of The Apparatus

Item	Detail	Value
Pipe	OD	6.37 mm
	wall thickness	0.16 mm
	length	5 m (approximately)
	material	316 Stainless Steel
	E	207 GPa
	υ	0.3
Channel	width	149 mm
	height	79 mm
	web thickness	9.5 mm
	material	aluminium
	length	6 m (= 2x3 m)
Soil	material	polycarbonate granules
	diameter of granules	3.5 mm
	electrical permittivity	3 (measured relative to a vacuum)
	solid density	1.2×10^3 kg/m
	overall density	0.77×10^3 kg/m
Trolley	material	3 mm aluminium plate
	length	300 mm
	width	260 mm
	mast height	655 mm (above trolley deck)
	deck height	80 mm (above channel section base)
	total height	800 mm
Stepper Motor	Voltage	50 V
	Steps / cycle	200
Electrical Signal	frequency	1 kHz
	voltage	16 V RMS.
Sensor	output	0-200 mV RMS.
Amplifier	amplification	10 x
	output	0-2 V DC

A.1.2 Control System

Item	Brand	Model
Signal Generator	Feedback	Function Generator TWG 501
Power Amplifier	Amcron	M600 1500 Watts
Stepper Motor Drive	Digiplan	Microstepper Drive
Data Logger	Solartron	IMP/PC
Computer	IBM	AT 286 with maths co-processor

A.1.3 The Position Measuring Algorithm

(i) Take four data sensor readings S1, S2, S3 & S4. The algorithm interpolates the position from the sensor reference data. S_{ref} and SS_{ref}.

(ii) Rank the data sensor readings in order.

(iii) S_{data} = largest sensor reading.

(iv) SS_{data} = ratio of the largest sensor reading / second largest reading.

(v) Using grid co-ordinates, for y=0 to 5 find the x position where $SS_{ref}=SS_{data}$.

(vi) Calculate the value of S_{ref} at each of these points.

(vii) Fit a polynomial P_1 (y) between the S_{ref} points with respect to y.

(viii) Use the polynomial P_1 (y) to find the y position where $S_{ref}=S_{data}$.

(ix) Fit a polynomial P_2 (y) between the x positions from step (v) with respect to y.

(x) Substitute value of y from step (viii) into polynomial P_2 (y) to calculate x.

(xi) Convert grid co-ordinates to mm co-ordinates.

A.2 List of the Experimental Tests

A.2.1 The Soil Response Tests

Schedule: U up, D down, H horizontal, R return to start, Nx repeat x times. Q Depth of soil cover mm. * The soil surface is covered by a metal plate.

Test	Schedule	Q (mm)	Comments
Jul25L01	D	6	
Jul25L02	U	6	
Jul25L03	H	6	
Jul25L04	U	6	
Jul25L05	D	6	
Jul25L06	U	6	
Jul25L07	U	6	
Jul30L01	DURHHR	6	
Jul30L02	DURHHR	6	
Jul30L03	DHUHDHR	6	
Jul30L04	DRHR	6	
Jul30L05	DRHR	6	
Jul30L06	DRHR	6	
Jul30L07	DHUHDHR	6	
Jul30L08	DRHR	6	Cover Plate*
Jul30L09	DRHR	6	" "
Jul30L10	DRHR	6	" "
Jul30L11	HHR	6	" "
Jul30L12	DUR	6	
Jul30L13	HHR	6	
Jul30L14	DUR	6	Cover Plate
Aug05L01	UDR N3	12	
Aug05L02	UDR N3	12	Re-level Soil
Aug05L03	UDR N3	12	Cover Plate
Aug05L04	HHR N3	12	" " + weights
Aug05L05	HHR N3	12	Re-level soil
Aug05L06	HHR N3	12	
Aug06L01	UDR N3	12	
Aug06L02	HHR N2	12	
Aug06L03	UDR N2	12	
Aug06L04	HHR N3	12	
Aug13L01	D	6	
Aug13L02	UDR N4	6	
Aug13L03	HHR N2	6	
Aug13L04	UDR N3	6	
Aug13L05	HHR N3	6	Cover Plate + weights
Nov21L01	H	6	
Nov21L02	H	8	
Nov21L05	U	6	

Test	Schedule	Q (mm)	Comments
Nov21L06	H	12	
Nov21L07	H	10	
Nov25L01	H	12	
Nov25L02	H	10	
Nov25L03	H	7	
Nov25L04	H	6	
Nov25L05	H	6	
Jan30L01	U	6	
Jan30L02	U	6	
Jan30L03	H	6	
Jan30L04	U	12	
Jan30L05	H	12	
Jan30L06	U	18	
Jan30L07	H	18	
Jan30L08	D	18	
Jan30L09	U	18	
May20L01	U	6	
May20L02	H	6	
May20L03	U	6	
May20L04	H	6	
May20L05	U	12	
May20L06	H	12	
May20L07	U	18	
May20L08	H	18	

A.2.2 The Axial Load Tests

Q Depth of Soil Cover mm.

Test	Q (mm)	Axial Load Schedule (N)
Jun27D01	6	46-73-96-110-132-160
Jun28D01	6	43-90-114-138-149-159
Jun28D02	6	23-35-48-58-77-92-112-132-146-154-156-169-178
Jul02D01	6	51-58-81-101-121-143
Jul03D01	6	34-42-52-60-71-84-104-112
Jul03D02	6	23-35-44-61-71-81-91-99
Jul08D01	6	35-50-70 (Hydraulic)
Jul09D01	6	20-60-70-80-95-101 (Hydraulic)
Jul09D02	6	26-51-75-99
Jul17D01	6	22-42-61-81-100-122-141
Jul17D02	6	43-61-79-103-121-141
Jul17D03	6	21-40-66-84-99-117
Aug19D01	6	53-79-107-129-155
Aug19D02	6	56-80-99-117-156
Aug22D01	6	55-79-104-130
Aug28D01	6	57-78-101-127

Test	Q (mm)	Axial Load Schedule (N)
Nov27D01	12	31-53-80-111-134-160-173
Jul20D01	12	50-84-117-149
Jul20D02	12	52-78-101-121
Jul20D03	12	51-74-94-119
Jul22D01	12	52-83-101-121-131-140
Jul22D03	12	51-81-107-127-154
Jul24D01	12	60-89-112-132-150-170
Jul24D02	12	59-87-105-132-163

A.2.3 The Horizontal Load Tests

Q Depth of Soil Cover mm. Schedule: H+ add horizontal load.

Test	Q (mm)	Load Schedule	Comments
Jul29D01	6	H+++++++	
Aug20D01	6	H+++++++	
Nov28D01	6	H++++++++	

A.2.4 The Combined Horizontal and Axial Load Tests

Schedule: H+ add horizontal load, H- remove horizontal load, A+ add axial load.

Test	Q (mm)	Load Schedule	Comments
Aug20D02	6	H+ A+++++	
Jul29D02	6	H+ A+++++	

A.2.5 Add and Remove The Horizontal Load

Schedule: H+ add horizontal load, H- remove horizontal load, A+ add axial load.

Test	Q (mm)	Load Schedule	Comments
Sep19D01	6	H+ H- A++++++	Fail
Sep19D02	6	H+ H- A++++++	
Sep19D03	6	H+ H- A++++++	
Sep20D01	6	H+ H- A++++++	
Sep20D02	6	H+ H- A++++++	
Sep23D01	6	H+ H- A++++++	
Sep23D02	6	H+ A++++++ H-	
Sep23D03	6	H+ A+ H- A+++++	
Sep23D04	6	H+ A++ H- A+++	
Sep23D05	6	H+ A+++++ H- A+	
Sep23D06	6	H+ A+ H- A+++++	
Sep24D02	6	H+ A+++++ H- A+	
Sep24D03	6	H+ A+++++ H- A+	

Appendix A.2

Test	Q (mm)	Load Schedule	Comments
Sep25D01	6	A++ H+ A+ H-	Fail
Sep25D02	6	A+++ H+ A+ H- A+	
Sep27D01	6	H+ A+++ H- A++	
Sep27D02	6	A++ H+ A+ H- A++	
Sep27D03	6	H+ A+++ H- A++	
Sep27D04	6	H+ A+++ H- A++	
Sep30D01	6	H+ A+++ H- A++	
Sep30D02	6	H+ A+ H- A++++	
Sep30D03	6	A++ H+ A+ H- A+	Fail
Sep30D04	6	H+ A++ H- A+++	
Sep30D05	6	H+ A++ H- A+++	
Sep30D06	6	H+ A++ H- A+++	
Sep30D07	6	H+ A++++ H- A+	Fail
Oct01D01	6	H+ A+++ H- A++	
Oct01D02	6	H+ A++++ H- A	Fail
Oct01D03	6	H+ A+++ H- A++	
Oct01D04	6	H+ A+++ H- A++	
Oct02D01	6	H+ A++++	Fail
Oct02D02	6	H+ A+++ H- A++	
Oct02D03	6	H+ A+++ +	Fail
Oct02D04	6	H+ A++++ H- A+	
Oct02D05	6	H+ A+++ H- A+++	
Oct03D01	6	H+ A+++ H- A+++	
Oct03D02	6	H+ A+++ H- A+++	
Oct03D03	6	H+ A+++ H- A+	Fail
Oct03D04	6	H+ A+++ H- A+++	
Oct04D01	6	H+ A+++ H- A+++	
Oct04D02	6	H+ A+++ H- A+	Fail
Oct04D03	6	H+ A+++ H- A+++	
Oct07D01	6	H+ A+++ H- A+++	
Oct07D02	6	H+ A+++ H- A+++	
Oct07D03	6	H+ A+++ H- A+++	
Oct07D04	6	H+ A+++ H- A+++	
Oct07D05	6	H+ A+++ H- A+	Fail
Oct08D01	6	H+ A+++ H- A+++	
Oct08D02	6	H+ A+++ H- A+++	
Oct09D01	6	H+ A+++ H- A+++	
Oct09D02	6	H+ A+++ H- A+	Fail
Oct09D03	6	H+ A+++ H- A+++	
Oct09D04	6	H+ A+++ H- A+++	
Oct10D01	6	H+ A+++ H- A+++	
Oct10D02	6	H+ A+++ H- A+++	
Oct11D01	6	H+ A+++ H- A+++	
Oct11D02	6	H+ A+++ H- A+++	
Oct11D03	6	H+ A+++ H- A+++	
Oct14D01	6	H+ A+++ H- A+++	
Oct14D02	6	H+ A+++ H- A+++	
Oct14D03	6	H+ A+++ H- A+++	
Oct14D04	6	H+ A+++ H- A+++	
Oct14D05	6	H+ A+++ H- A+++	

A.2.6 The Cyclic Axial Load Tests

Q Depth of Soil Cover mm. Schedule: H+ add horizontal load, H- remove horizontal load, A+ add axial load.

Test	Q (mm)	Load (N)	No of Cycles	Comments
Jun03D03	6	20-85	860 x	
Jun03D03	6	65-130	360 x	
Jun03D06	6	40-105	560 x	
Jun13D01	6	0-70	350 x	
Jul18D01	6	0-70	141 x	
Aug29D01	6	5-90	161 x	Fail
Aug29D02	6	5-90	560 x	
Aug29D04	6	25-110	381 x	
Sep02D01	6	40-130	11 x	Fail
Sep02D02	6	5-80	761 x	
Sep03D01	6	5-60	761 x	
Sep04D01	6	5-40	561 x	
Sep04D02	6	65-100	761 x	
Sep05D01	6	85-120	46 x	Fail
Sep05D02	6	95-130	1 x	Fail
Sep05D03	6	5-20	561 x	
Sep06D01	6	55-75	561 x	
Sep06D02	6	100-120	761 x	
Sep11D01	6	100-120	761 x	
Jul27D01	12	0-105	3 x	End Load Applied
Jul27D02	12	0-55	3 x	" " "
Jul27D03	12	0-70	3 x	" " "
Jul27D04	12	0-30	3 x	" " "
Jul27D05	12	0-90	3 x	" " "
Jul27D06	12	0-100	3 x	" " "

A.3 The Finite-Difference Model

A.3.1 Theory

The finite-difference model is a numerical version of the Tvergaard and Needleman model (1981), which is described in Chapters 2 & 3. A schematic diagram of the finite-difference model, is shown in figure 8.1. The model considers a quarter-wavelength of an imperfection, and is divided into 10 sections of length Δ, which are separated by 11 nodes. The diagram shows node (i), which is a distance $x=i\Delta$ from node (0), and its two neighbouring nodes, (i-1) & (i+1). The vertical displacements at the three nodes are designated by y_{i-1}, y_i & y_{i+1}, respectively, and are joined by straight-line segments to approximate the curved profile of the pipeline.

From small deflection beam theory, the curvature of the pipe at node (i) can be expressed as:

$$EI\left(y'' - y_0''\right)_i = -\sum_i M \tag{8.1}$$

Here, y_0'' is the curvature of the initial imperfection profile, and Σ_i M is the sum of the bending moments acting at node (i). The curvature at node (i) can be expressed in terms of the discrete data points as:

$$y_i'' = \frac{y_{i-1} - 2y + y_{i+1}}{\Delta^2} \tag{8.2}$$

Similarly, the bending moments acting at node (i) can be taken about node (0); which is a point of inflection, the bending moment at that point being zero. Thus at node (i), the sum of the bending moments can be expressed as:

$$\sum_i M = Py_i + S_i x - m_i \tag{8.3}$$

Here, S_i is the shear force acting at node (i), and m_i is the bending moment at node (i) due to the vertical load along the pipe. The shear force S_i can be calculated as:

$$S_i = \left(\frac{W_i + W_{10}}{2} + \sum_{n=i+1}^{n=9} W_n\right)\Delta \tag{8.4}$$

Here, W_i is the vertical load N/m at node (i). The shear force at node (10), $S_{10}=0$. Similarly, the bending moment due to the vertical load m_i, can be calculated as:

$$m_i = \left(\frac{W_i}{2} i + \sum_{n=1}^{n=i+1} W_n n \right) \Delta^2 \qquad (8.5)$$

The bending moment due to the vertical load at node (0), $m_{10}=0$. The vertical load at node (i) W_i, is an exponential function of the vertical displacement ΔY_i, and can be expressed as:

$$W_i = W_0 \left(1 - \exp(-\Delta y_i / y_l)\right) \qquad (8.6)$$

Here, y_l is the proportional limit of the soil. Combining equations (8.1), (8.2) and (8.3), the vertical or y position at node (i), y_i can be expressed as:

$$y_i = \left(EIy_0'' + S_i + m_i - EI \frac{y_{i-1} + y_{i+1}}{\Delta^2} \right) / \left(P - \frac{2EI}{\Delta^2} \right) \qquad (8.7)$$

This is solved by iteration.

A.3.2 The Finite-Difference Algorithm

The vertical displacement y is calculated for a given value of the axial load P, by a repeated iteration technique. The steps are as follows:

(i) Set the values of V_0, L, EI, W_0, & Δ.

(ii) Load the initial imperfection profile.

(iii) Calculate y_0'', for each node.

(iv) Set the value of the axial load P.

(v) For i=1 to 10, calculate y_i. Repeat until the value of y_{10} converges to a solution.

(vi) Increase the value of P by an increment ΔP, and repeat step (v) until the value of y_{10} no longer converges to a solution. (This signifies buckling)

(vii) Stop.

A.3.3 Figures

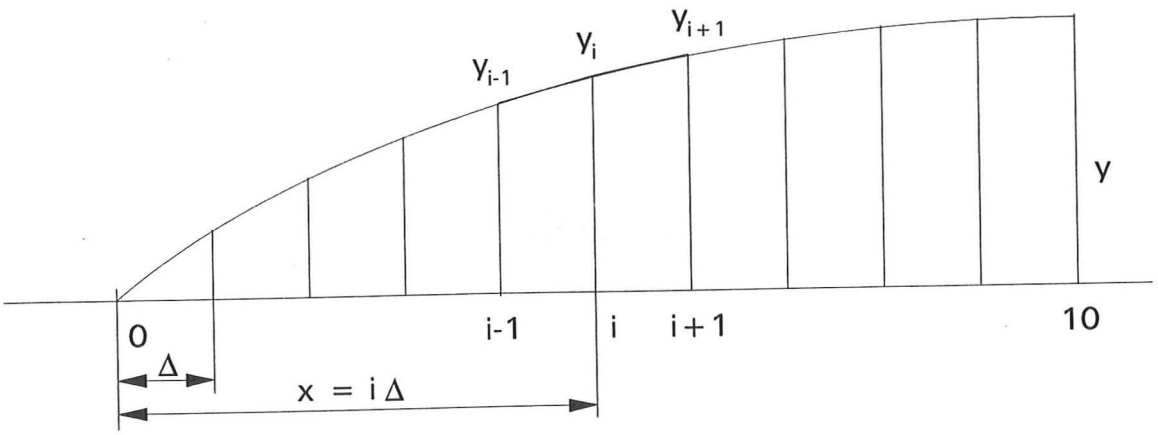


Figure 8.2. A schematic diagram of the finite-difference model. The figure shows a quarter-wavelength of a sinusoidal imperfection, which is divided into 10 sections, separated by 11 nodes.

UNIVERSITY LIBRARY CAMBRIDGE

CAMBRIDGE
UNIVERSITY LIBRARY

Attention is drawn to the fact that the copyright of this dissertation rests with its author.

This copy of the dissertation has been supplied on condition that anyone who consults it is understood to recognise that its copyright rests with its author. In accordance with the Law of Copyright no information derived from the dissertation or quotation from it may be published without full acknowledgement of the source being made nor any substantial extract from the dissertation published without the author's written consent.